FLUORESCENCE CORRELATION SPECTROSCOPY: Simulations and Bio-Chemical Applications based on Solid Immersion Lens Concept

THÈSE N^{O} 3697 (2006)

PRÉSENTÉE LE 1er DÉCEMBRE 2006

À LA FACULTÉ DES SCIENCES ET TECHNIQUES DE L'INGÉNIEUR

Laboratoire d'optique biomédicale

SECTION DE MICROTECHNIQUE

ÉCOLE POLYTECHNIQUE FÉDÉRALE DE LAUSANNE

POUR L'OBTENTION DU GRADE DE DOCTEUR ÈS SCIENCES

PAR

Ramachandra RAO

M.Tech in applied optics, Indian Institute of technology Delhi, Inde
de nationalité indienne

acceptée sur proposition du jury:

Prof. Ph. Renaud, président du jury
Prof. T. Lasser, directeur de thèse
Prof. O. Martin, rapporteur
Prof. R. Rigler, rapporteur
Prof. J. Widengren, rapporteur

ÉCOLE POLYTECHNIQUE
FÉDÉRALE DE LAUSANNE

Lausanne, EPFL
2006

Abstract

Fluorescence Correlation Spectroscopy (FCS) has become an important tool for measuring diffusion, concentration and molecular interactions in biomolecular systems. Two major requirements for FCS are good collection efficiency and a small and well defined excitation volume. This thesis presents an elegant approach in addressing these basic requirements via a single lens element. The Solid Immersion Lens (SIL) is used to obtain a highly confined light field in the excitation volume and also good collection efficiency.

The SIL was utilized with a standard microscope objective and the results compared to that of a conventional high NA water immersion objective. With suitable aberration compensation in solution it was proved that the performance with the SIL was similar to that close to the surface.

The field characterization for the SILs FCS is described by the vectorial Debye diffraction theory with an emphasis on the aberration function for the SIL with generalized Zernike polynomials. The accurate determination of the collection volume geometry for the SIL is also shown by utilizing the vectorial diffraction theory. The most important advance here was to minimize the illuminated sample volume with increased collection efficiency at increasing focusing depths in the sample with aberration compensation.

For many applications in the field of life sciences, biology and medicine a well controlled heating of the sample is necessary. Therefore a thermal, mechanical and/or electrical decoupling is of great interest and utility. This handling modality is easily realized due to the separation of the SIL lens and the microscope objective and/or microscope body. This is demonstrated by the SIL thermal chamber which is used to measure vesicles at varying temperatures.

In extension to the work related to FCS in general,the utilization of a novel global stochastic algorithm is studied for analyzing FCS data. This new application would automate FCS data analysis reducing user induced errors to a black-box level. The theoretical treatment extends to simulations performed on raw photon traces on a software multiple tau correlator and over noise analysis on experimental data.

Keywords: Fluorescence Correlation Spectroscopy, Solid Immersion Lens, Vectorial Diffraction theory, Debye approximations, Aberrations, Vesicles and Stochastic Algorithms.

Résumé

La Spectroscopie de Corrélation de Fluorescence (Fluorescence Correlation Spectroscopy, FCS) est devenue un outil majeur pour l'étude des systèmes biomoléculaires, permettant de mesurer la diffusion, la concentration et les interactions moleculaires. Une grande efficacité de collection ainsi qu'un volume de exitation restreint et bien défini constituent deux conditions nécessaires pour la FCS. La présente thèse expose une approche élégante pour remplir ces conditions de base au moyen d'une unique lentille. Une Lentille à Immersion Solide (Solid Immersion Lens, SIL) est utilisée pour garantir un champ lumineux hautement confiné ainsi qu'une bonne efficacité de collection. Les résultats, obtenus avec la SIL combinée à un objectif de microscope standard, ont été comparés à ceux obtenus avec un objectif de microscope à immersion d'eau conventionnel de grande ouverture numérique. Grâce à une correction appropriée des aberrations, il a été prouvé que les performances de la SIL focalisant dans la solution étaient identiques à celles obtenues proche de la surface.

La théorie vectorielle de la diffraction de Debye permet la description du champ de la SIL-FCS. Les polynômes généralisés de Zernike ont été utilisés pour décrire plus particulièrement la fonction d'aberration de la SIL. La détermination précise de la géométrie du volume de collection pour la SIL est assurée elle aussi grâce à la théorie vectorielle de diffraction. Le plus important progrès consiste à minimiser le volume illuminé de l'échantillon tout en augmentant l'efficacité de collection grâce à la compensation des aberrations pour des profondeurs de focalisation croissantes dans l'échantillon.

De nombreuses applications en science du vivant, biologie et médecine requièrent un echauffment local contrôlé de l'échantillon, et/ou une détection électrique. C'est pourquoi une indépendance des systèmes de chauffage, mécanique, et/ou électrique est d'un intérêt prépondérant. Cette indépendance existe grâce à une séparation complète du corps du microscope lui-même, de l'objectif de microscope et de la SIL. Cet avantage est démontré par la mise en place d'une chambre thermique SIL, utilisée pour mesurer des échantillons de vésicules à diverses températures.

En extension au travail lié à la FCS en général, l'utilisation d'un nouvel algorithme stochastique global pour l'analyse des données de FCS est investiguée. Ceci permettrait d'automatiser complètement le traitement des données de FCS, ramenant le système à un appareil de type boîte noire, réduisant ainsi les erreurs dues à l'utilisateur. Le traitement théorique est étendu à l'analyse du bruit réalisée sur des traces brut de photons grâce à un corrélateur a tau multiples virtuel.

Mots-clés: Spectroscopie de Corrélation de Fluorescence, Lentille à Immersion Solide, théorie Vectorielle de la Diffraction, approximations de Debye, Aberrations, Vésicules, Algorithmes Stochastiques.

To Swami
and my parents.

General Introduction

One of the fields of optical technology where immense developments have been seen in the last decades is fluorescence microscopy and spectroscopy. First appearing as a branch of fundamental spectroscopy physics, the field has evolved toward various applications both in the biological sciences and in applied physics. This has led to the development of ultra-sensitive techniques such as Fluorescence Correlation Spectroscopy (FCS) [1–3] and Fluorescence Intensity Distribution Analysis (FIDA) [4–6] used for the study of single biomolecule dynamics in fluid media.

Fluorescence is a sensitive indicator of molecular kinetics for appropriately chosen reactants, as it also offers a number of other advantages that further distinguish it from light scattering absorbance as well as other optical indicators. They are:

- Simplicity and speed of measurement.
- Low background intensity because the excitation light is highly suppressed away from the measured fluorescence.
- Sensitivity of detection, which readily reaches the nanomolar concentration range and extends to the single molecule regime.
- Spectral selectivity that allows detection of specifically labelled fluorescence molecules in the presence of high concentrations of unlabelled molecules. This makes the measurement of specified molecules in complex systems such as cells possible.
- Applicability of multi-color techniques such as fluorescence resonance energy transfer and cross-correlation.

FCS is one of the many different modes of high-resolution spatial and temporal analysis of extremely low concentrated biomolecules. The parameter of interest is the spontaneous intensity fluctuations caused, *i.e.*,, the minute deviations of the system from thermodynamic equilibrium. In general, all physical parameters that give rise to fluctuations in the fluorescence signal are accessible by FCS. It is, for example, rather straightforward to determine local concentrations, mobility coefficients or characteristic rate constants of inter- or intramolecular reactions of fluorescently labelled biomolecules in nanomolar concentrations. FCS is also an easy to implement alternative for obtaining information on the photodynamical properties of fluorescent dyes not accessible by classical means. It allows the determination of the kinetics of triplet state (dark state) formation [7,8], of photon anti-bunching [9] and of photobleaching processes [10].

The technique was developed in the early seventies as a special case of relaxation analysis. Classical relaxation methods induce certain kinds of external perturbations such as temperature or pressure jumps to a reaction system, and gain information about involved kinetic parameters from the path the system returns back to equilibrium. The novel concept of FCS with respect to these classical techniques is to take advantage of the minute spontaneous fluctuations of physical parameters that are somehow encoded in the fluorescence emission of the molecules. Such fluctuations are incessantly occurring at ambient temperatures and are generally represented as (unwanted) noise patterns of the measured signal, in our case, emission of fluorescence. The fluctuations can be quantified in their strength and duration by temporally autocorrelating the recorded intensity signal. Autocorrelation analysis provides a measure for the self-similarity of a time series signal and therefore describes the persistence of information carried by it. Essential information about processes governing molecular dynamics can thus be derived from the temporal pattern by which fluorescence fluctuations arise and decay. Among the main advantages of this technique is its non-invasive nature with shorter measurement times and with good time resolution.

The essential idea of FCS is based on observing the intensity fluctuation of fluorescence from individual molecules in a small open volume element defined by a laser beam with a Gaussian intensity profile, *i.e.*, looking at the fluctuations of the registered photon events . In the earlier seventies, Elson [1] and Magde [11, 12] as well as Ehrenberg and Rigler [13] derived the principle theory behind FCS. During the 1990s FCS enjoyed an upsurge of interest due mainly to technological advances that made the measurements much faster and easier. These were pioneered in the laboratories of Rigler and Eigen [14]. Perhaps the most important advance was to minimize the illuminated sample volume. Although confocal optics had been used for FCS measurements nearly from the beginning, Rigler and coworkers demonstrated systematically that using a minimal sample volume conferred some important advantages such as reducing the correlation time for diffusion. This reduction substantially accelerated the collection of data and reduced the time required to measure simple diffusion by more than an order of magnitude. In addition, the reduced sample volume diminished the relative contribution of nonspecific background fluorescence, including Raman and Rayleigh scattering. Using highly sensitive photon detectors, such as avalanche photodiodes, made it possible to measure very small numbers of molecules, even to the level of single molecules.

From a technological point of view, one of the critical optical requirements of the FCS technique are high collection efficiency and a small and well defined volume of detection. It is here that the Solid Immersion Lens (SIL) comes in to play the pivotal role by satisfying these requirements. Essentially a high index aplanatic lens (see Chapter 1), it has played a major role in pushing the diffraction limits in microscopy and data-storage applications [15]. With the applications of SILs to photoluminescence microscopy [16], it was seen that one achieved not only high spatial resolution but also greater improvement in collection efficiency [17]. With this as the backdrop, the utilization of the SIL for FCS becomes a natural extension and has also paved the way for new questions regarding the shape and size of the observation volumes as relevant for FCS.

This thesis characterizes the SILs for FCS both experimentally and theoretically. The collection volume geometry for the SIL is accurately determined by utilizing the vectorial diffraction theory. The important advance here was to demonstrate a minimized illuminated sample volume with increased collection efficiency both near the surface and several microns into solution [18]. The theoretical framework presented in the thesis describes the observation volume parameters in the vectorial Debye formalism with the inclusion of spherical aberration and validates experimental data.

For many applications in the field of life sciences a local heating of the sample is necessary. Therefore a thermal, mechanical and/or electrical decoupling is of great interest and utility. It is here that the opto-mechanical mounting of the SIL onto the microscope body comes into play. Due to the air-gap between the SIL and the air-objective it becomes feasible to develop a thermal chamber with the SIL wherein the thermal isolation from the microscope objective and the microscope body becomes a practical reality. This handling modality is demonstrated with measurements on Rhodamine Green solution at 10nM concentration and the subsequent validation of the diffusion times at the molecular level in consonance with the Stokes-Einstein relationship for freely diffusing liquids. This approach is further demonstrated on an application to a sample, which is a model system for putative nano-reactors [19]. The measurements on lipid vesicles highlights the potential for biological applications [20].

In extension to the work related to FCS in general, the utilization of a novel global stochastic algorithm called PGSL, an acronym for Probabilistic Global Search Lausanne, is studied for analyzing FCS data [21]. Currently used algorithms are typically accurate when the user has a good knowledge of the sample system at hand. Also an essential prerequisite for these categories of algorithms is the sound knowledge of the behavior of fit parameters and in most cases good initial guesses for accurate fitting otherwise leading to fitting artifacts. However, for heterogeneous systems or where automated data analysis is a prerequisite, there is generally a need to apply procedures that treat FCS data fitting as a black box and generates reliable fit parameters with accuracy for the chosen model in hand. This new application would automate FCS data analysis reducing user induced errors and automates FCS data analysis to a black-box level. The theoretical analysis extends to noise analysis performed on raw photon traces on a software multiple tau correlator [22]. The experimental noisy data is also studied for a standard 2-component system.

The thesis is organized as follows: In Chapter 1, an overview of various SIL related concepts is presented and also the current state of the art applications in various areas of spectroscopy and imaging. In Chapter 2 the overall vectorial theory for the SIL is developed and presented. Its relevance to the experimental details is highlighted. The influence of high numerical apertures and aberrations on the point spread functions are also discussed. In Chapter 3 the overall description of the SIL-FCS experiments are presented. In Chapter 4 the results obtained with the SIL thermal heating chamber are presented and summarized. The experiments performed with vesicles are presented. Finally, we describe and present the PGSL algorithm which would help in automated FCS data analysis in Chapter 5.

Contents

Chapter 1

The Solid Immersion Lens (SIL)

1.1 Introduction

The push for both improved spatial resolution and the incorporation of new capabilities in microscopic imaging has been a constant presence in the scientific community. The SIL technique was first proposed by Mansfield and Kino [23] to improve the spatial resolution of the optical microscope. Analogous in behavior to the liquid immersion oil, it extends the diffraction limit by filling the object space with a high refractive index material [24]. It has since found application in data storage [25], lithography [26], near-field optics [27] and the study of semiconductor nanostructures [28]. It turned out that with the applications of SILs to photoluminescence microscopy [16] one achieved not only high spatial resolution but also greater improvement in collection efficiency [17]. The simultaneous advantage of high spatial resolution with collection efficiency in fluorescence microscopy has made SILs a useful tool for detection, imaging and spectroscopy of weak fluorescence from single molecules and biological samples tagged with fluorescent molecules. In this thesis, all calculations and experiments were done throughout for the hemispherical SIL (h-SIL).

1.2 Preliminaries

In this chapter we give a brief overview from the viewpoint of simple refraction and the definition of the aberration function using simple geometrical optics. Various basic concepts related to the SIL are explained in the context of geometrical optics. The SIL as an "aplanatic" lens is seen in the next section. It is followed by a discussion on the h-SIL and the W-SIL (Weierstrass-SIL).

1.3 Spherical refracting surface

In Fig. 1.1, the aberration of a ray PAP' from an off-axis point object P passing though a point A on the refracting surface with respect to the off-axis chief ray

PBP' (denoted as CR) passing through the center O of the exit pupil is given by

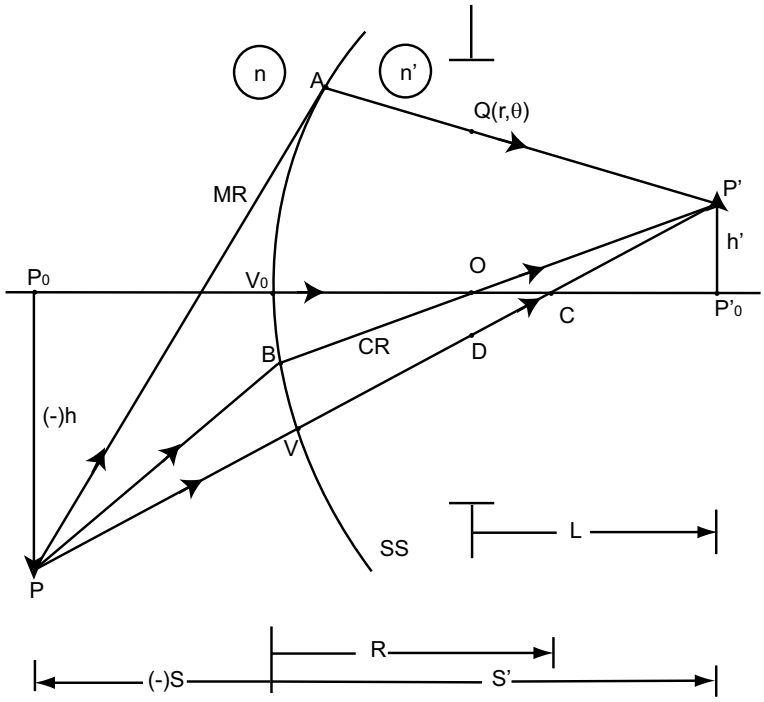

Figure 1.1: Imaging of an off-axis point object P by a spherical refracting surface of radius of curvature R and center of curvature C . The aperture stop and, therefore, the exit pupil are not located at the surface here. The Gaussian image is located at P'.

The point V, where the undeviated ray PVP' intersects the refracting surface, lies in the tangential plane. Hence, its projection in the plane of the exit pupil lies along the x- axis as shown in Fig. 1.2. The primary aberration function of a spherical surface with respect to the Gaussian image point P' may be written as

$$W_s(r,\theta;h') = a_{ss}r^4 + a_{cs}h'r^3 cos\theta + a_{as}h'^2r^2cos^2\theta + a_{ds}h'^2r^2 + a_{ts}h'^3rcos\theta. \quad (1.1)$$

The primary aberration function given in Eq. 1.1 consists of five terms. The first term is independent of the angle θ of a pupil point Q and is denoted as *spherical aberration*. The second term, which depends on the pupil coordinates as $r^3\cos\theta$ and linearly on h' is denoted as *coma*. The third term, which depends on pupil coordinates as $r^2\cos^2\theta$ and quadratically on h' is called *astigmatism*. The fourth term, which varies as h'^2r^2, is called *field curvature* while the fifth term, which varies as $h'^3rcos\theta$ is called *distortion*.

a_s represents the coefficient of the *fourth order spherical wave aberration* and is given by [29]

$$a_s = \frac{n'^2}{8}\left(\frac{1}{R} - \frac{1}{S'}\right)^2\left(\frac{1}{n'S'} - \frac{1}{nS}\right), \quad (1.2)$$

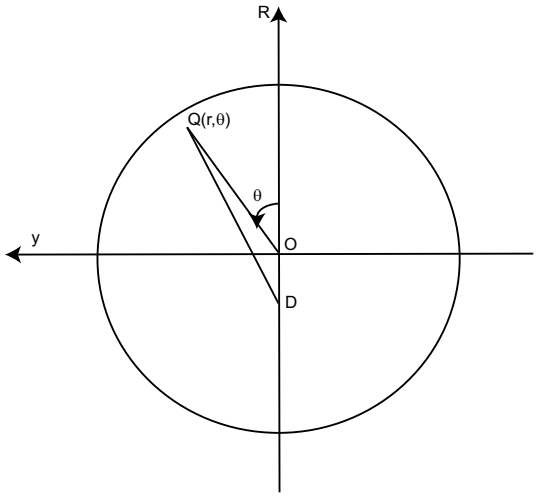

Figure 1.2: Coordinates (r, θ) of a pupil point Q. D is the point of intersection of the undeviated ray with the plane of the exit pupil.

and

$$d = \frac{R - S' + L}{S' - R}. \tag{1.3}$$

Therefore,

$$a_{ss} = (S'/L)^4 a_s, \tag{1.4}$$

$$a_{cs} = 4d a_{ss}, \tag{1.5}$$

$$a_{as} = 4d^2 a_{ss}, \tag{1.6}$$

$$\begin{aligned} a_{ds} =& 2d^2 a_{ss} - \frac{n'(n'-n)}{4nRL^2}, \\ =& \frac{1}{2}\left[a_{as} - \frac{n'(n'-n)}{2nRL^2}\right], \end{aligned} \tag{1.7}$$

$$a_{ts} = 4d^3 a_{ss} - \frac{n'(n'-n)d}{2nRL^2}. \tag{1.8}$$

1.3.1 Aplanatic points of a Spherical Refracting Surface

An optical system that is free of spherical aberration and coma is called an **aplanatic system**. Conjugate points that are free of these aberrations are called **aplanatic points**. From Eqs. 1.5 and 1.6, we now determine the values of the image distance S' for which both a_{ss} and a_{cs} are zero. For these values of S', we then determine the other aberration coefficients according to Eqs. 1.5 and 1.8.

Substituting Eq. 1.2 into Eq. 1.4, we can write

$$a_{ss} = -\frac{n'(n'-n)}{8n^2}\frac{S'(S'-R)^2\left[n'S'-(n+n')R\right]}{R^3L^4} \tag{1.9}$$

$$= 0 \begin{cases} \text{for } \ S'=0, & \text{or} \\ S'=R, & \text{or} \\ S'=\frac{(n+n')R}{n'} \end{cases} \tag{1.10}$$

Substituting Eq. 1.3 and Eq. 1.4 into Eq. 1.5, we can write

$$a_{cs} = -\frac{n'(n'-n)}{2n^2}\frac{S'(R-S'+L)(S'-R)\left(n'S'-(n+n')R\right]}{R^3L^4} \tag{1.11}$$

$$= 0 \begin{cases} \text{for } \ S'=0, & \text{or} \\ S'=R, & \text{or} \\ S'=\frac{(n+n')R}{n'} \end{cases} \tag{1.12}$$

It is therefore clear from Eq. 1.10 and Eq. 1.12 that there are three values of S', namely, 0, R and $(n+n')R/n'$ for which both spherical aberration and coma are zero.

$$a_{as} = -\frac{n'(n'-n)}{2n^2}\frac{S'(R-S'+L)^2\left[n'S'-(n+n')R\right]}{R^3L^4}. \tag{1.13}$$

$$= 0 \begin{cases} \text{for } \ S'=0, & & \text{or} \\ \frac{n'(n'-n)}{2nRL^2} & \text{for } \ S'=R, & \text{or} \\ 0 & \text{for } \ S'=\frac{(n+n')R}{n} & \end{cases} \tag{1.14}$$

The corresponding image magnifications are given as 1, n/n' and $(n/n')^2$ respectively. In each of these three cases, either the object or the image is virtual. The conjugate points in any of the three conjugate planes are aplanatic, and conjugate planes may be called **aplanatic planes**.

The SIL satisfies the above conditions leading to aberration free imaging in the ideal focusing case (corresponds to $d = 0$, Chapter 2). SILs discussed in literature come in one of two designs: the hemisphere, and the Weierstrass (or super-hemisphere) geometry. Other modifications and designs reported include the Diffractive SIL [30], OptiSIL [31], Aspheric SIL [32], Planar Waveguide SIL [33], High-performance SILs (HPSILs) [34] and Microfabricated Silicon SIL [35].

1.4 Hemispherical Solid Immersion lens (h-SIL)

The h-SIL [23] is particularly interesting in microscopy applications, since this lens is more achromatic when compared to the W-SIL (see Section. 1.5. This makes it specially useful for white light microscopy.

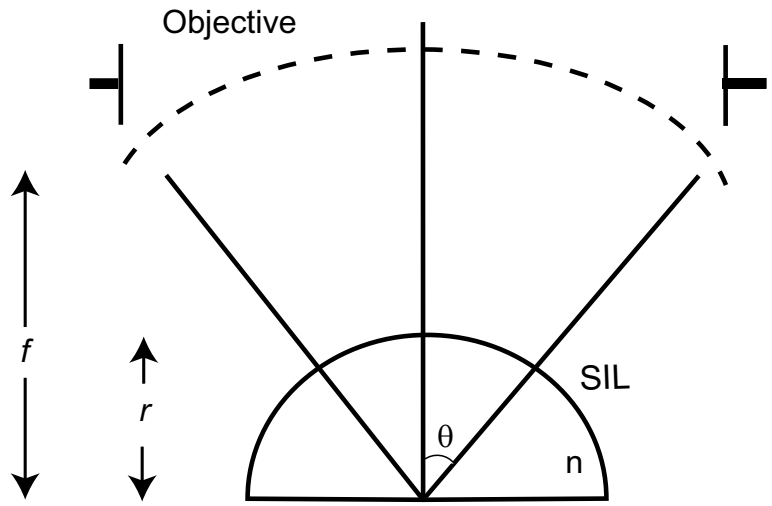

Figure 1.3: Schematic of a hemispherical SIL (thick curve) with the radius r and refractive index n

Using the h-SIL, we have the following spatial resolution,

$$\Delta d = \frac{\lambda/n}{2NA}, \tag{1.15}$$

where, λ is the wavelength used, NA is the numerical aperture of the objective lens and n is the refractive index of the SIL.

Hemispheres do not have longitudinal chromatic aberration because neither the height of hemispheres nor the position of the image plane is wavelength dependent. The remaining chromatic aberration is lateral chromatic aberration, *i.e.*, the variation of magnification for different wavelengths. This aberration is very small since, for most optical materials, the variation of the magnification, or n, is only a few percent over the entire visible spectrum. Therefore, hemispheres can be regarded as nearly achromatic.

1.4.1 Evanescent wave and near field effect

When the light is incident normally to the SIL, it is focussed exactly at the center of the bottom of the SIL, then the evanescent wave which decays exponentially to the depth h, exists just beneath the bottom of the SIL (near the boundary of the SIL and the air gap). At that, if one approaches with some media or a specimen to the SIL planar surface within the distance h, the coupling effect occurs between the SIL and the media by this evanescent wave so that the light energy can be transferred to the media. This is the near-field effect [36, 37]. However in our experiments we ignore the contribution due to this since, a 0.6NA air objective is used with the h-SIL.

1.5 Weierstrass Solid Immersion lens (W-SIL)

In the Weierstrass geometry [38, 39], the height of the SIL is $r + a = (1 + 1/n)r$, where n is the refractive index of the SIL and r its radius of curvature (Fig. 1.4). Hence the Weierstrass SIL effectively compresses the emitted light into a small numerical aperture.

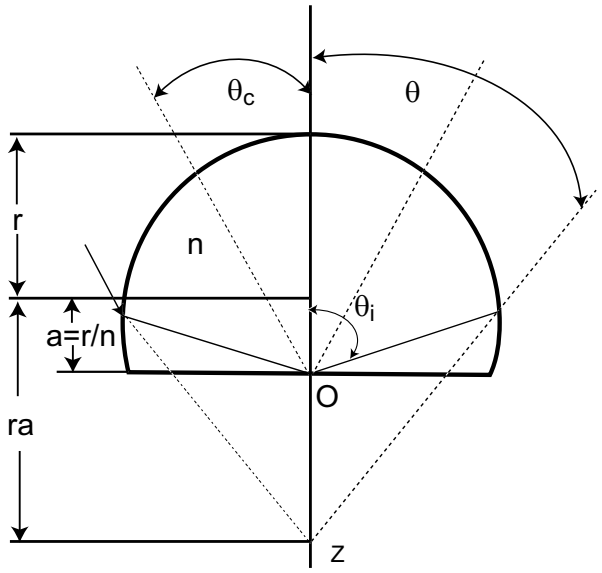

Figure 1.4: Schematic of a Weierstrass-sphere SIL (thick curve) with the thickness of $(1 + 1/n)r$ defined by radius r and refractive index n. Polar angles θ_i and θ in and out of the SIL show the relation $sin\theta_i = nsin\theta$.

The expression for the resolution for the W-SIL is given by:

$$\Delta d = \frac{\lambda/n}{2nNA} \tag{1.16}$$

where we clearly see the n^2 improvement in the spatial resolution.

The W-SIL has the inherent disadvantage as it has serious chromatic aberration. With reference to FCS it implies a mismatch in the overlap of the confocal volumes for the illumination and detection wavelengths. This is because both the thickness and the vertical position of the image plane are dependent on n, which is a function of wavelength. It has been shown that the diffraction-limited bandwidth of the W-SIL is only about 10nm in the visible spectrum [40]. This effective narrow focal depth means that the obtained resolution is valid for only tens of nanometers on top of the W-SIL surface. This nanoscale working distance is a severe barrier for FCS applications where the diffusion studies require a comfortable working distance in solution of the order of several microns.

Chapter 2

SIL Vector Theory

2.1 Introduction

What is the best optical description of a SIL-FCS experiment? This chapter comprises the focus of this study. A conventional FCS set-up typically allows for changes in the type and numerical aperture (NA) of the objective lens which determines the nature of the focal volume. The use of a high aperture scalar theory is also not particularly useful as an approximation to the vectorial case [41]. It becomes necessary to use a vectorial model when precise quantitative measurements are to be done in the case of a high NA optical collection or illumination system. This is required for computing the observation volume geometries incorporating the input state of polarization and modelling the fluorophore as an oscillating dipole averaged over all orientations. Such a high NA description is provided by the vectorial Debye theory [42] which approximates the diffraction pattern to be a superposition of plane waves whose propagation direction is within the geometrical focal cone [43]. In the context of the SIL-FCS experiments we have a physical system which has an overall NA of ~ 1.2 and has a linearly polarized input. We therefore use the integral representation based on the diffraction integrals proposed by [44], which is valid for optical systems of high numerical aperture in the Debye approximation [42]. Previous works made significant approximations in the treatment of the focal volume, particularly at high-NA [45]. It is commonly assumed that the observation volume in FCS is Gaussian in three dimensions. However, it is shown that this is not exactly accurate for the case of the SIL-FCS setup. The focal volume formulation is defined using the description of Wolf [44,46] that treats the polarization of the excitation field and is well-suited to high-NA optics as in the case for the SIL [47].

2.2 Preliminaries

In this chapter we give a brief overview of the Debye approximation generally used in focusing problems and then develop a brief sketch of the formulation of the Debye integral elaborating it further for the SIL lenses. The chapter is organized as follows. We define the fields at the focus for a standard microscope

objective as elucidated in literature and show the natural extension to the case of the SIL. Later on, the effect of spherical aberrations is incorporated and the possibility of compensation (with the correction collar ring) for the SIL system with an air objective is shown.

2.3 Point Spread Function (PSF)

The Intensity Point Spread Function (PSF) is defined as the 3D image of a point source. It is also the intensity distribution in the vicinity of the focal plane resulting from a point source of monochromatic light in the image plane of a lens system. In order to evaluate the 3D PSF for the SIL-microscope objective combination, few models based on the diffraction theory have been proposed. Scalar Debye theory, paraxial approximation, and vectorial Debye theory have been used to evaluate the PSF [48].

2.4 Vector Diffraction Theory - Debye Approximations

2.4.1 Introduction

For high numerical aperture systems where effects due to the vector character of the electric field become important, a vector diffraction theory is necessary. A plane wave incident on a focussing system is transformed into a converging spherical wave. The starting point of the approach is to expand this spherical wave into an angular spectrum of plane waves. For systems with large Fresnel numbers, as in our case, the approximation due to Debye is used to calculate the angular spectrum [49]. According to the Debye approximation, the field in the focal region is a superposition of plane waves whose propagation vectors fall inside the geometrical cone by drawing straight lines from the focal point through the edge of the aperture. Thus, in the Debye approximation there is an abrupt cut-off of the angular spectrum. It corresponds to the use of the geometrical optics approximation of the angular spectrum of the incident field. The field in the focus can be evaluated by superposing those plane waves, keeping track of the phase and the direction of polarization.

2.4.2 Debye Theory

According to the Rayleigh-Sommerfeld and Kirchhoff formulas and assuming that the wavefront over the diffraction aperture is a spherical surface with the origin in the focal point, the light field at an arbitrary point near the focal point O (Fig.2.1) can be expressed as

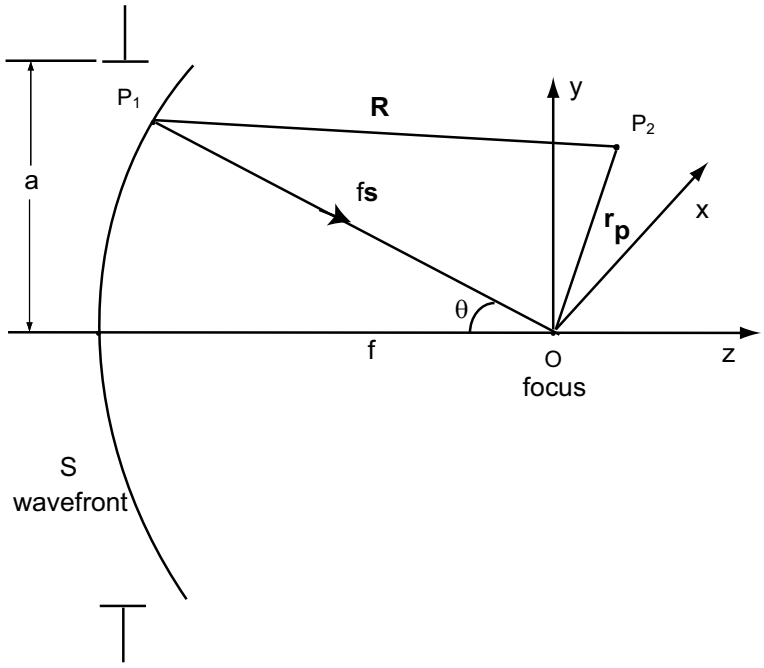

Figure 2.1: Focusing of a spherical wave through a microscope objective.

$$E(P_2) = \frac{i}{\lambda} \int_{\Sigma} E(P_1) \frac{\exp[ik(r-f)]}{fr} \cos(\mathbf{n},\mathbf{R}) dS, \tag{2.1}$$

where $E(P_1)$ denotes the light amplitude at a point within the diffraction aperture Σ, λ is the wavelength of the incident radiation, $k = 2\pi/\lambda$ is the wavenumber and $P(P_1)$ is the aperture function. Eq. 2.1 includes the contribution from the Debye integral plus plane waves outside the geometrical cone. Considering that the observation point is not far away from the origin O we can apply, according to the Debye theory, the following simplifications

a) The approximation that the spherical wavelets originating from the diffraction aperture Σ are replaced by plane wavelets

$$R - f = \mathbf{s} \cdot \overrightarrow{r_p} \tag{2.2}$$

b) The approximation that the area element dS is expressed as

$$dS = f^2 d\Omega \tag{2.3}$$

where $d\Omega$ is the solid angle corresponding to the area dS.
c) The directional cosine can be approximately expressed as

$$\cos(\mathbf{n},\mathbf{R}) \approx 1 \tag{2.4}$$

d) In the denominator of Eq. 2.1 the distance r can be accordingly replaced by f.
Under these approximations, Eq. 2.1 is reduced to the so-called Debye integral

$$E(P_2) = \frac{i}{\lambda} \int_{\Omega} P(P_1) \exp[ik(s.R)] d\Omega \tag{2.5}$$

where the field is expressed as a superposition of plane waves of different propagation directions $\overrightarrow{s}$, which fill the solid angle Ω subtended by the lens at the focus. The approximations (Eqs. 2.2- 2.4) involved in deriving this expression are called the **Debye approximations**.

2.5 Electric field formulation

Therefore, for a focusing problem, one can start with the following equation for the electric field in the Debye approximation for an arbitrary medium i as:

$$\mathbf{E}_i = \frac{i}{\lambda} \int_{\Omega_i} \mathbf{T}(\mathbf{s}_i) \exp[ik_i(s_{ix} + s_{iy} + s_{iz})] ds_{ix} ds_{iy} \tag{2.6}$$

where $\mathbf{s}_i = (s_{ix}, s_{iy}, s_{iz})$ is the unit vector along a typical ray, $\mathbf{T}(s)$ is the vector pupil distribution, which accounts for the polarization, phase and amplitude distribution at the exit pupil within the diffraction aperture Ω. The electric field at the focal plane is obtained by matching the fields in the second and third media at the interface, $z = -d$. The resulting electric field in the third medium is given by:

$$\mathbf{E}_3 = C \int_{\Omega_i} \mathbf{T}(s_i) \exp[id(k_3 s_{3z} - k_2 s_{2z})] \exp(k_3 s_{3z}) \exp[ik_2(s_{2x} + s_{2y})] ds_{2x} ds_{2y}. \tag{2.7}$$

The unit vector $\hat{s}_3$ and position vector $\mathbf{r}$ are given in spherical polar coordinates by:

$$\hat{s}_3 = \sin\theta_3 \cos\phi \hat{i} + \sin\theta_3 \sin\phi \hat{j} + \cos\theta_3 \hat{k} \tag{2.8}$$

$$\hat{\mathbf{r}}_p = r_p(\sin\theta_p \cos\phi_p \hat{i} + \sin\theta_p \sin\phi_p \hat{j} + \cos\theta_p \hat{k}) \tag{2.9}$$

where $\hat{i}, \hat{j}, \hat{k}$ are the unit vectors of the (x, y, z) orthogonal system and the spherical polar coordinates (r, θ, ϕ) are defined so that $r > 0$, $0 \leq \theta < \pi$, and $0 \leq \phi < 2\pi$.

Eq. 2.7 can be written as

$$\mathbf{E}_3 = \int_0^{\alpha} \int_0^{2\pi} \mathbf{T} \exp[ik_0(r_c \kappa + \Phi)] \sin\theta_1 d\theta_1 d\phi \tag{2.10}$$

where,

$$\mathbf{T}(\theta_1, \phi) = P(\theta_1, \phi) A(\theta_1, \phi) \tag{2.11}$$

where $P(\theta_1, \phi)$ is the polarization and $A(\theta_1, \phi)$ represents the amplitude and phase distribution at the exit pupil. Since the objective obeys the sine condition, we have $A(\theta_1) \propto \sqrt{cos\theta_1}$

$$\kappa = n_3 \cos\theta_3 \cos\theta_p + n_2 \sin\theta_2 \sin\theta_p + \cos(\phi - \phi_p) \tag{2.12}$$

and

$$\Phi = d\left[n_3 \cos(\theta_3) - n_2 \cos(\theta_2)\right] \tag{2.13}$$

Φ represents the aberration function due to the refractive mismatch in the media. Rewriting Eq. 2.7 explicitly,

$$\mathbf{E}(\rho_p, \phi_p, z_p) = \int_0^{\alpha}\int_0^{2\pi} P(\theta_1, \phi)\sqrt{cos\theta_1}\exp[ik_3\rho_p sin\theta_2 cos(\phi - \phi_p) \exp(ik_0\psi) sin(\theta_1) d\theta_1 d\phi. \tag{2.14}$$

2.5.1 The polarization vector

To account for polarization effects at high NA, one usually considers the effects of the refraction law on the polarization vector [42]. For a treatment of the refraction that occurs at any interface, it becomes convenient to decompose the polarization (or electric field) vector into $s-$ and $p-$ polarized vector components, *i.e.*, into e_s and e_p respectively. The coordinate system is then rotated that will contain components in the (p, s, ζ) system which is defined in such a way that $e_\zeta = 0$. The incident vector $\mathbf{P}_0 = (1, 0, 0)$ corresponds to x- polarized light.

The polarization vector $\mathbf{P}(\theta_1, \phi)$ of the transmitted field in Eq. 2.14 can be written as [50]

$$\mathbf{P}(\theta_1, \phi) = \mathbf{R}^{-1}(\phi)[\mathbf{L}^3(\theta_3)]^{-1}\mathbf{T}\mathbf{L}^2(\theta_2)\mathbf{C}(\theta_1)\mathbf{R}(\phi)\mathbf{P}_0(\theta_1, \phi) \tag{2.15}$$

where

- $\mathbf{P}(\theta_1, \phi)$ is the polarization vector of incident light in the form of Cartesian basis;
- $\mathbf{R}^{-1}(\phi)$ represents the rotation operation of the coordinate system around the optical axis;
- $\mathbf{C}(\theta_1)$ describes the change of polarization on propagation through the lens;
- $\mathbf{L}^j(\theta_j)$describes a clockwise rotation operation of the coordinate system into s- and p-polarized vectors
- $\mathbf{T}$ represents the transmission matrix (of the equivalent Fresnel coefficients) through the Air-SIL-Water media.

The matrices describing the operations $\mathbf{P}_0$, $\mathbf{R}$, $\mathbf{C}$, $\mathbf{L}$ and $\mathbf{T}$ are expressed by:

$$\mathbf{P}_0(\theta_1,\phi) = \begin{bmatrix} 1 \\ 0 \\ 0 \end{bmatrix}, \text{for } x\text{- polarized light,} \tag{2.16}$$

$$\mathbf{R}(\phi) = \begin{bmatrix} \cos\phi & \sin\phi & 0 \\ -\sin\phi & \cos\phi & 0 \\ 0 & 0 & 1 \end{bmatrix}, \tag{2.17}$$

$$\mathbf{C}(\theta) = \begin{bmatrix} \cos\theta & 0 & \sin\theta \\ 0 & 1 & 0 \\ \sin\theta & 0 & \cos\theta \end{bmatrix}, \tag{2.18}$$

$$\mathbf{L}^j(\theta_j) = \begin{bmatrix} \cos\theta_j & 0 & -\sin\theta_j \\ 0 & 1 & 0 \\ \sin\theta_j & 0 & \cos\theta_j \end{bmatrix}, \tag{2.19}$$

$$\mathbf{T} = \begin{bmatrix} T^p_{SIL} & 0 & 0 \\ 0 & T^s_{SIL} & 0 \\ 0 & 0 & T^p_{SIL} \end{bmatrix}, \tag{2.20}$$

where T^s_{SIL} and T^p_{SIL} are the equivalent reflection and transmission coefficient for a SIL. Substituting Eqs. 2.16-2.20 into Eq. 2.7 and after some algebraic transformations, we have the following expression for the polarization vector of the transmitted field

$$\mathbf{P}_0(\theta_1,\phi) = \begin{bmatrix} \frac{1}{2}(T^p_{SIL}\cos\theta_3 + T^s_{SIL}) + \frac{1}{2}(T^p_{SIL}\cos\theta_3 - T^s_{SIL})\cos 2\phi \\ \frac{1}{2}(T^p_{SIL}\cos\theta_3 - T^s_{SIL})\sin 2\phi \\ -T^p_{SIL}\sin\theta_3\cos\phi \end{bmatrix}. \tag{2.21}$$

When inserted in Eq. 2.14 and solved over ϕ, this gives the transmitted field, as follows:

$$\mathbf{E}(\rho_c,\phi_c,z_c) = \begin{pmatrix} -i(I_0 + I_2\cos 2\phi) \\ -iI_2\sin 2\phi \\ -2I_1\sin 2\phi \end{pmatrix} \tag{2.22}$$

Now we write the three Intensity equations

$$I_0 = \int_0^{\alpha} (\cos\theta_1)^{1/2}\sin\theta_1\exp[ik_0\Phi(\theta_1,\theta_2,-d)](T^s_{SIL} + T^p_{SIL}\cos\theta_3) \\ J_0(k_2 r\sin\theta_2)\exp(ik_3 z\cos\theta_3)d\theta_1 \tag{2.23}$$

$$I_1 = \int_0^{\alpha} (\cos\theta_1)^{1/2} \sin\theta_1 \exp[ik_0\Phi(\theta_1,\theta_2,-d)](T_{SIL}^{p} sin\theta_3) \\ J_1(k_2 r \sin\theta_2)\exp(ik_3 z\cos\theta_3)d\theta_1 \tag{2.24}$$

$$I_2 = \int_0^{\alpha} (\cos\theta_1)^{1/2} \sin\theta_1 \exp[ik_0\Phi(\theta_1,\theta_2,-d)](T_{SIL}^{s} - T_{SIL}^{p} cos\theta_3) \\ J_2(k_2 r \sin\theta_2)\exp(ik_3 z\cos\theta_3)d\theta_1 \tag{2.25}$$

In the above expression α follows from $n\sin\alpha = NA$ which is the convergence semi-angle of the illumination and $J_0(x)$ the Bessel functions of order n, first kind. In Eqs. 2.23 - 2.25 spherical polar coordinates are used with the usual notation $0 < \theta < \pi$ and $0 < \phi < 2\pi$.The transmission coefficients T^s and T^p are computed according to [43]. Note that $\theta_1 = \theta_2$ corresponds to the normal incidence condition for the SIL.

$$T_{SIL}^{s,p} = \frac{t_{12}^{s,p} t_{23}^{s,p} exp(i\beta)}{1 + r_{12}^{s,p} r_{23}^{s,p} exp(2i\beta)} \tag{2.26}$$

with $\beta = k_2 \times r_{\mathrm{SIL}} \times \cos\theta_2$ where $t_{12}^{s,p}$,$t_{23}^{s,p}$,$r_{12}^{s,p}$,$r_{23}^{s,p}$ are the Fresnel transmission and reflection coefficients.

2.6 SIL Aberration function

The incoming spherical wavefront from the microscope objective, which illustrates the surface of constant phase, is a sphere with a radius corresponding to the distance with respect to the origin O. The curved spherical wavefront represents the ideal wavefront when focused on the SIL planar surface, corresponding to the aplanatic condition. The wavefront due to the variation by the correction collar is represented by the aspherical dotted line in Fig. 2.2. The overall wavefront aberration of the SIL system is now given by

$$\Phi = \Phi_{\mathrm{sph}} + \Phi_{\mathrm{planar}} \tag{2.27}$$

wherein, Φ_{sph} denotes the contribution from the spherical interface of the SIL and Φ_{planar} is the contribution from the planar interface (See Appendix 2.10). Since, $\mathrm{d} \ll r_{\mathrm{SIL}}$ (See Fig. 2.2), the difference in the curvatures of the incident wavefront and the SIL spherical surface is small. The contribution from the spherical interface Φ_{sph} is essentially a longitudinal defocus term which can be neglected in the overall analysis when compared to the dominant contribution due to the planar interface term [29]. Therefore the geometric aberration function for the SIL with good approximation is given as [51],

$$\Phi(\theta_1) \approx d\Big[n_3\cos(\theta_3) - n_2\cos(\theta_2)\Big] \tag{2.28}$$

The aberration function is independent of the azimuthal angle of the system and therefore, for a simple evaluation of the angles that go into the SIL aberration function we consider the $Z-X$ plane corresponding to the plane of the paper. The following analysis takes into account the system geometry and provides the angles required for every micron of axial displacement in solution. These angles are further incorporated in the overall computation of the Fresnel coefficients.

In order to visualize the interdependence of the angles with respect to the SIL co-ordinate system, we consider the propagation of an arbitrary ray traversing across the entire air-SIL-water optical system. The spherical SIL surface can be represented as

$$(z_1+\mathrm{d})^2+x_1^2=r_{\mathrm{SIL}}^2, \tag{2.29}$$

whereas the equation of the incident wavefront from the objective is given by:

$$z_1^2+x_1^2=(r_{\mathrm{SIL}}+\mathrm{d})^2. \tag{2.30}$$

From Eqs. 2.29 and 2.30, we see that the wavefront intersects the SIL spherical surface at

$$(z,x)=(-(r_{\mathrm{SIL}}+\mathrm{d}),0) \tag{2.31}$$

where the axial defocus parameter d has also been included. Now consider an arbitrary ray from this incident wavefront from the objective to the origin of the coordinate system that is given by,

$$x_1=-m_1z_1, \tag{2.32}$$

where $m_1=\tan\theta_1$ is the slope the ray makes with respect to the horizontal. Solving for Eqs. (2.29)and (2.32) gives the intersection point on the spherical surface of the SIL for the incoming ray given by,

$$A(z_1,x_1)=\left(\frac{-2d-\sqrt{4d^2-4(1+m_1^2)(d^2-r_{\mathrm{SIL}}^2)}}{2(1+m_1^2)},-m_1z_1\right). \tag{2.33}$$

The angle ϕ can be computed from the slopes of the two points $A(z_1,x_1)$ and $C(-\mathrm{d},0)$ as,

$$\phi=\frac{\tan\theta_1(r_{\mathrm{SIL}}+d)}{r_{\mathrm{SIL}}} \tag{2.34}$$

The angle ϕ which corresponds to the normal for the SIL spherical surface can be computed from the slope of the two points $A(z_1,x_1)$ and $C(-\mathrm{d},0)$ as,

$$\phi=\arctan\left(\frac{x_1}{\mathrm{d}+z_1}\right) \tag{2.35}$$

On the SIL's spherical interface, we have

$$n_1\sin(\phi-\theta_1)=n_2\sin(\phi-\theta_2) \tag{2.36}$$

from which the refracted angle into the SIL is then given by,

$$\theta_2 = \phi - \arcsin\left[\frac{n_1}{n_2}\sin(\phi - \theta_1)\right] \tag{2.37}$$

The refracted angle in water due to the the refractive index mismatch at the interface is then given by,

$$\theta_3 = \arcsin\left(\frac{n_2 \sin\theta_2}{n_3}\right). \tag{2.38}$$

The above coordinate transformations through the SIL also hold for an aberrated wavefront propagating through the SIL system. The considerations in Eqs. 2.29-2.38 constitute the overall aberration function for the SIL. Following [52], we now use a general aberration function that can be expanded in terms of Zernike polynomials to eliminate the explicit dependence on θ.

A general aberration function Φ can be expanded in terms of Zernike polynomials as,

$$\Phi(\rho,\theta) = \sum_{n,m} A_{nm}\varepsilon_{nm}R_n^m(\rho)\cos(m\theta), \tag{2.39}$$

where

$$\varepsilon_{nm} = \begin{cases} \frac{1}{\sqrt{2}} & m = 0, n \neq 0 \\ 1 & \text{otherwise} \end{cases}$$

The Zernike coefficients are given from Eq. 2.39 by

$$A_{nm} = \frac{n+1}{\pi}\int_0^1\int_0^{2\pi}\Phi(\rho,\theta)\varepsilon_{nm}R_n^{(m)}(\rho)\cos(m\theta)\rho d\rho d\theta \tag{2.40}$$

Since there is no azimuthal variation we can consider only Zernike circle polynomials of order n and zero kind, Z_n^0. We therefore have:

$$f(\rho) = A_{00} + \sum_{n=2}^{\infty} A_{n0}Z_n^0(\rho) \tag{2.41}$$

Ignoring the coefficient A_{00} as a constant piston term and which has no effect on the aberrated point spread function, we can therefore write the SIL aberration function in Eq. 2.28 as:

$$\Phi(d,\rho) = \left[\sum_{n=2}^{2N+2} A_{n0}Z_n^0(\rho)\right] dn_1 \sin\alpha \tag{2.42}$$

2.6.1 Optimization of the SIL Aberration function

Many objective lenses incorporate optics that allow for correction of the aberrations introduced by coverglasses of differing thickness. The degree of correction,

corresponding to the thickness of coverglass, is usually controlled by means of a collar on the objective. Using such an objective with the SIL, one can compensate for the aberrations introduced by defocus in solution. We seek to find the limit of the degree of compensation possible for a SIL with a 0.6NA objective with correction collar and benchmark the performance within a 25% variation of the parameters as obtained in the aplanatic "0" position of the SIL system. Finally the performances are compared with the reference 1.15NA Olympus system.

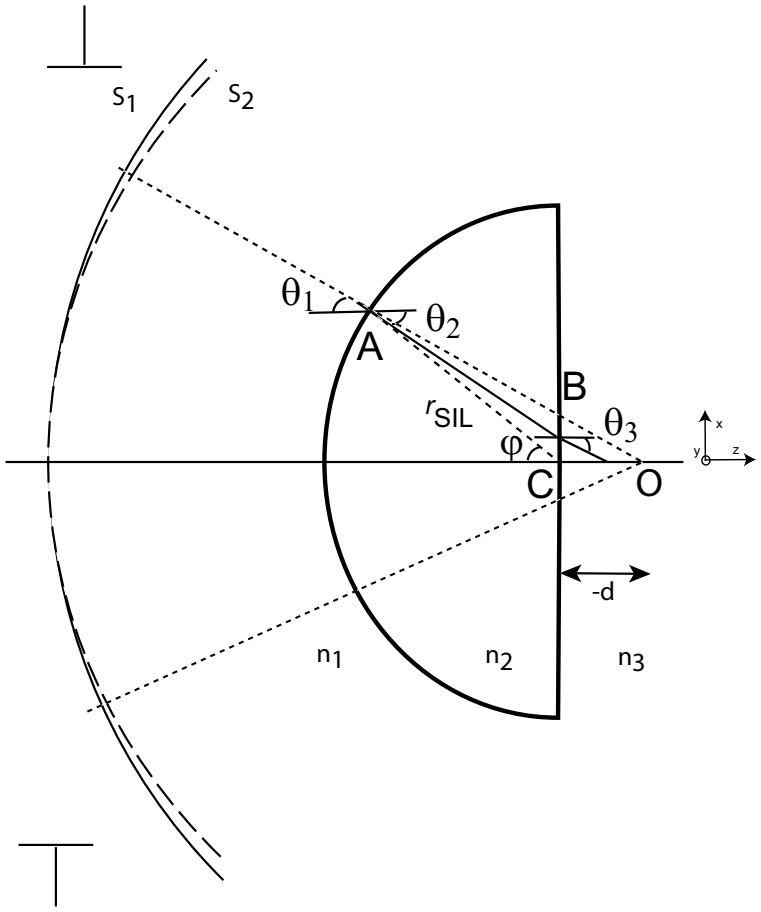

Figure 2.2: Schematic of the SIL illumination geometry. The SIL is defocused axially at a distance $z = -d$ from the Gaussian focus. The dark spherical curved line (S_1) represents the unaberrated wavefront emerging from the objective which is perfectly symmetrical with respect to the curved SIL surface while the dotted aspherical line (S_2) represents the compensated wavefront from the objective which balances the axial defocus into solution.

Zernike polynomials have the useful property that they balance aberrations. For example, an expression for third-order spherical aberration contains an appropriate term for defocus, *i.e.*, what the amount of defocus should be to yield maximum intensity with the given aberration. We now seek to correct the defocus term by introducing a pre-aberration that is opposite to the amount of each Zernike aberration contained within. To do that we represent the SIL aberration function as an infinite sum of Zernike aberration terms with being the strength of the Zernike mode [53]. We now seek the various strengths of the Zernike modes

for increasing aberration orders for correction at increasing focusing depths. This is specified by the compensated aberration function.

$$\Phi^{'}(d,\rho) = \Phi(d,\rho) - \left[\sum_{n=2}^{2N+2} B_{n0} Z_n^0(\rho)\right] dn_1 \sin\alpha \tag{2.43}$$

Thus, for N = 0, we apply refocusing, whereas N = 1 corresponds to correcting for first order spherical aberration, N = 2 corresponds to second order spherical aberration and so on. To obtain the improved performance in solution we now optimize the SIL compensated aberration function in conjunction with the Strehl ratio definition till N = 2.

Based on the definition of the Strehl ratio for a system with the above input aberration function the variance of the aberration across the pupil is given by [53]:

$$\sigma^2_{\Phi'} = \langle \Phi'^2 \rangle - \langle \Phi' \rangle^2 \tag{2.44}$$

where,

$$\Phi'^n = \frac{1}{\pi} \int_0^1 \int_0^{2\pi} \Phi'^n(\rho,\psi)\rho d\rho d\psi \tag{2.45}$$

where the angular brackets indicate an average across the pupil given by the integral in Eq. 2.45.

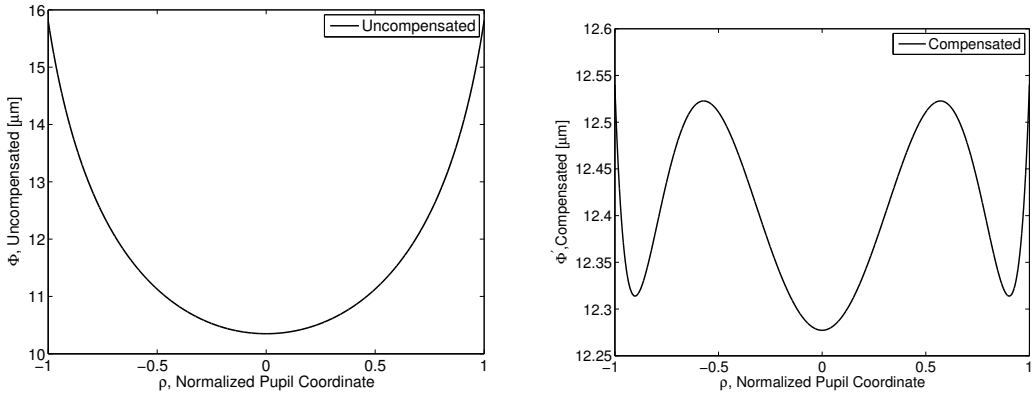

(a) (b)

Figure 2.3: The form of the SIL aberration functions $\Phi(d,\rho)$ and $\Phi^{'}(d,\rho)$ under the uncompensated and compensated conditions for d = 15μm.

The pupil function optimization is done by minimizing the variance of the phase function in Eq. 2.44 over the exit plane of the microscope objective for the SIL system. The phase function defined by Eq. 2.43 is given as an input to the 'fmins' function which is defined for multivariate functions in MATLAB. This acts as a "cost function" and generates unique solutions of (B_{n0}) in its multi-dimensional parameter space. The optimal values were obtained for various axial

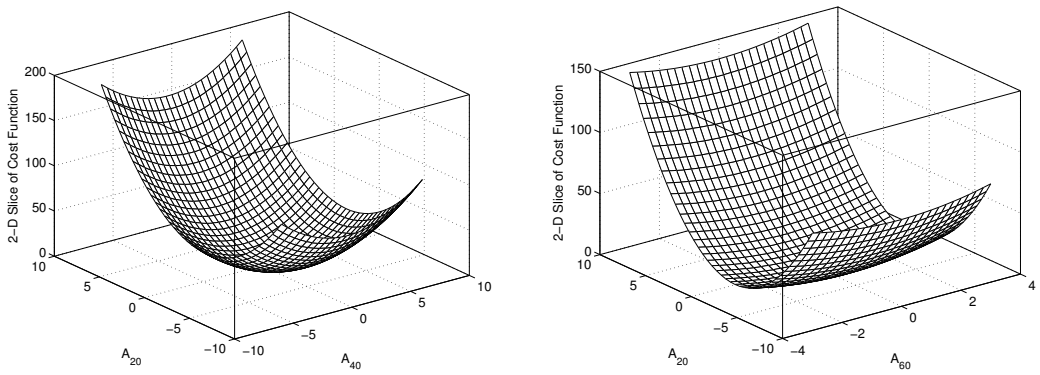

(a) (b)

Figure 2.4: The 2D convex cross sections of the multidimensional minimization routine for every micron of axial variation in solution plotted as a variation of the three variables and corresponds to a unique solution point.

displacements as seen in Table. 2.1. We see that for every micron of axial displacement there is a unique set of (A_{20}, A_{40}, A_{60}) values. The normalized aberration functions for $\Phi(d,\rho)$ and $\Phi^{'}(d,\rho)$ for Eq. 2.42 and Eq. 2.43, as a function of ρ are given in Fig. 2.3. A 2-D cross section of this multidimensional surface is presented in Fig. 2.4. This treatment can be scaled up for enumeration of other spherical aberration terms.

Table 2.1: Look-up table for the aberration coefficients obtained for Eq. 2.43 after the minimization routine.

$d[\mu\mathbf{m}]$	A_{20}	A_{40}	A_{60}
1	-0.1	0	0
2.5	-0.3	0	0
5	-0.5	-0.1	0
7.5	-0.8	-0.1	-0.05
10	-1	-0.2	-0.05
12.5	-1.3	-0.2	-0.05
15	-1.6	-0.3	-0.05
17.5	-1.9	-0.4	-0.1
20	-2.1	-0.4	-0.1

From Table (2.1) we see that there the impact of higher order terms ($N = 2$) starts only around 7.5μm of nominal focusing depth. Generally, aberration compensation with increasing focusing depth should do the following:

- Increase the peak intensity for increasing d.

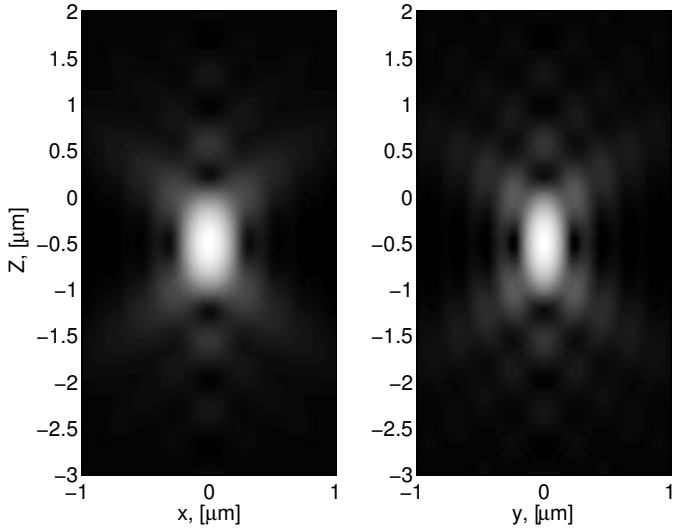

Figure 2.5: The *x* and *y* component of the PSFs of the 1.15NA Olympus objective.

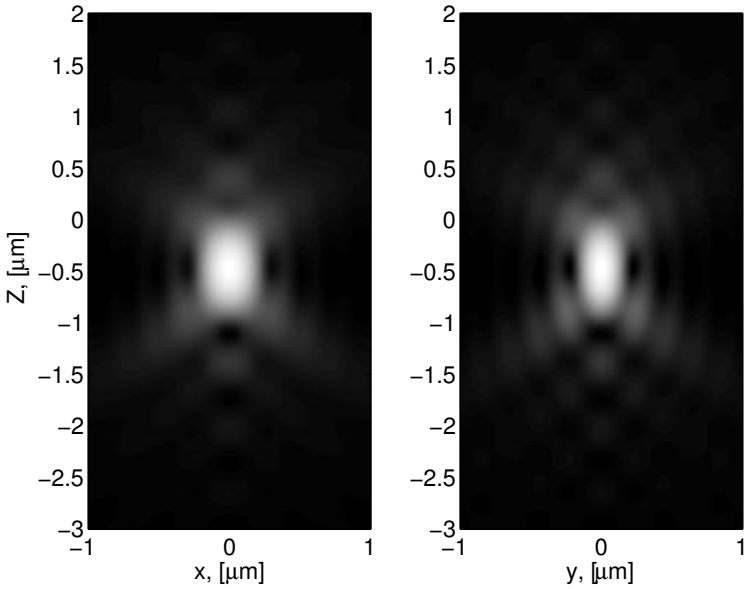

Figure 2.6: The *x* and *y* component of the PSFs of SIL + 0.6NA objective at d = 1 μm.

- Change the focus position *i.e.*, the position of the diffraction-optics focus relative to the Gaussian focus of the unaberrated position.
- Decrease the axial and lateral full width at half maximum (FWHM) of the compensated PSF *vs* the aberrated PSF.

2.7 Point Spread Functions(PSFs) distribution

The system parameters for modelling are based on the experimental set-ups in [18]. For the low NA microscope objective with a correction collar we chose a Zeiss objective 0.6NA LD Achroplan 40x/0.60 Korr, with a working distance of 1.8 mm, which is sufficient to position the SIL lens (0.7mm radius, LASF35, R.I = 2.02). The resultant NA for the above system is 1.2. This is compared with a water immersion objective of NA 1.15 (40x/1.15 Olympus, Uapo/340, (cover slip corrected)). This is considered as our standard reference system in all the calculations. Due to their similar NAs the EM field distributions for both of them are compared. All computations were performed using MATLAB. The intensity distributions in the *x*-*z* and the *y*-*z* meridional planes are presented and it gives us the vectorial asymmetric behaviors which are narrower in the direction perpendicular to that of the incident polarization. Results in Fig. 2.7 and Fig. 2.8 show the axial responses for a *d* variation for the two different cases here.

Fig. 2.6a and Fig. 2.6b shows the PSFs in meridional planes containing the *x* and *y* axes for the SIL based system. We denote it as the limiting experimental diffraction limited PSF, obtained with a nominal focusing depth (d = 1 μm). This axial displacement is considered as we focussed in solution to prevent surface effects on the overall experimental FCS curve. The axial FWHM obtained for the SIL is 0.57 μm.

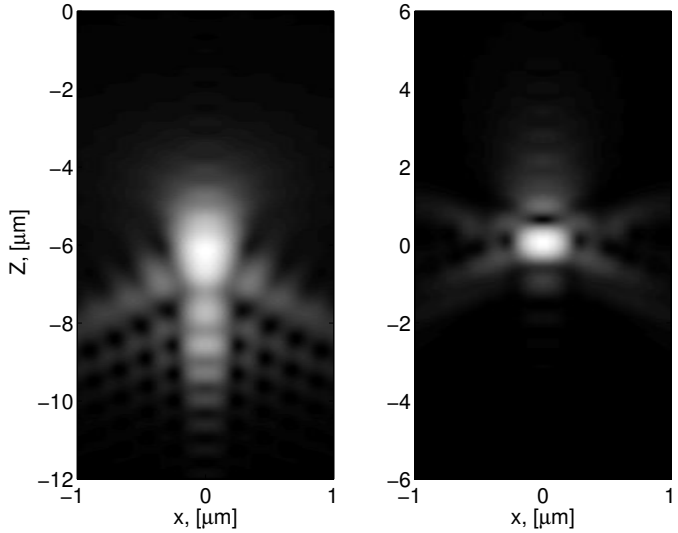

(a) (b)

Figure 2.7: The *x* component of the IPSFs of (a) SIL + 0.6NA objective at d = 15μm, (b) SIL + 0.6NA objective (aberration compensation setting) at d = 15μm.

Fig. 2.5a and Fig. 2.5b shows the electric energy density in the *x* and *y* axes for a 1.15 NA objective. We consider a simple coverglass ($n_{cg} = 1.518$) and water ($n_{water} = 1.33$) interface here and calculate the best possible diffraction performance here. This is the reference PSF with no effects of immersion liquids or coverslip correction factors (NA 1.15 (40x/1.15 Olympus, Uapo/340). The PSFs

have been estimated for the best possible performance (cover glass corrected) for the case of the reference system here. The axial FWHM obtained for the glass-water interface at 1.15NA is 0.66 μm.

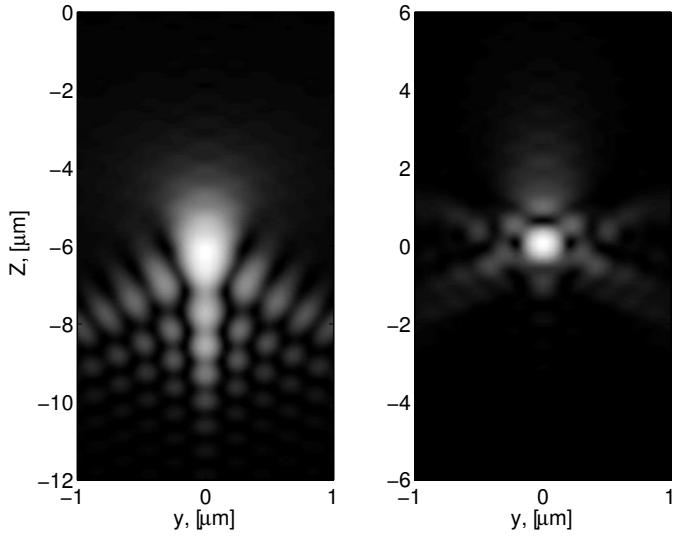

(a) (b)

Figure 2.8: The y component of the IPSFs of (a) SIL + 0.6NA objective at d = 15μm, (b) SIL + 0.6NA objective (aberration compensation setting) at d = 15μm.

In Fig. 2.7a and Fig. 2.8a it is clearly seen that for the nominal focusing depth of 15μm the focal spot is severely aberrated. The strong oscillations on one side of the maximum agree qualitatively with other results for axial responses in literature. Eq. (2.42) as the SIL aberration function is utilized in obtaining this PSF here. We note that the value $z/\mathrm{d} = -0.4$ is close to the value predicted by the low angle theory, $z/\mathrm{d} = (1 - n_1/n_2) = -0.51$. The distribution consists of a central aberrated spot that is displaced from the origin of coordinates and a fringe pattern situated on the interface side of the diffraction focus. The PSF is focussed 8.8 μm away from the SIL planar surface. The axial FWHM obtained here is 1.38 μm.

Fig. 2.7b and Fig. 2.8b shows the extent to which the aberration compensation has taken place with a resultant increase in the peak intensity of the primary lobe and also the FWHM optimized to 0.56 μm. We see that the focus position is close to the nominal value here. This is obtained for the case of aberration compensation which mainly takes into account the first orders $(N = 1$ and $2)$ here. We note that our simulations require the best possible wavefront to obtain the least aberrated PSF at the desired $z = d$ value. No additional assumptions regarding the axial defocus terms have been made here. We clearly see that aberration compensation has resulted in a decrease in the axial FWHM from 1.38μm to 0.56μm comparable to the case when the focusing is close to the SIL surface Fig. 2.9.

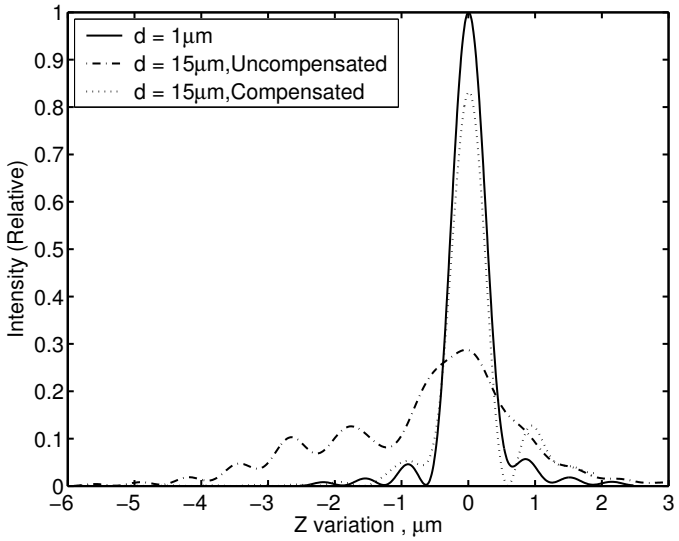

Figure 2.9: The variation in the axial dimensions and the relative peak intensities of the PSF when focusing at a nominal depth d $= 15\mu$m. The uncompensated (dash-dot) PSF and the compensated PSF (dot) with spherical aberration correction. The d $= 1\mu$m (dark line) case for the SIL is considered as the reference.

2.8 Aberration function and its relevance

The aberration function arising due to the refractive index mismatch has evoked several discussions in literature. Hell *et al*. [54] initially claimed that the use of an aberration function is not valid, as it varies within the focal region. As a result they use Fermat's principle in their calculation. Whereas Sheppard and Török justify their use as the aberration function is valid for systems of high Fresnel number. The principle here being that for any focal point the angular spectrum incident on any point in the focal region taking into account the path difference to the point of observation is constant. Therefore, the use of Fermat's principle is equivalent to the use of an aberration function. Finally the convergence in opinions between the two sides is seen in [55]. To conclude, the use of an aberration function is supported by the Zernike expansion from a rigorous diffraction integral [52]. This showed that the first-order spherical aberration was able to characterize the phase front distortion almost entirely. This is also seen in our analysis for the SIL system. The conversion of the analysis to a more generalized framework wherein higher order terms automatically get incorporated validates the usage of the aberration function. The other advantage of using an aberration function is the reduction in computational time since a double integral gets reduced to a single integral. Hence the expressions developed by Török have resulted in more usage for analyzing the fields at the focus [34, 56].

2.9 Discussion

The detailed vectorial theory presented here along with a generalized aberration compensation formalism characterizes the PSFs in a SIL set-up. In particular, the analysis proposed with the SIL-aberration phase function and its optimization scheme via the Strehl ratio can be applied to any general SIL based application. From the dimensions obtained from the primary maxima of the point spread functions we see that the PSF is optimally focussed for the SIL after suitable spherical aberration compensation by the collar variation of the microscope objective. The FWHMs in both the cases are comparable to the diffraction limited PSF of a conventional high NA water immersion objective case. The effect of tighter field confinement is also clearly seen for the SIL systems. One is therefore able to justify the comparable performances for the SIL based system in solution aided by appropriate aberration compensation. Simple aberration correction up-to second order restores near diffraction limited performance in solution for an axial focusing of $15-20\mu$m. These results also agree well with the obtained parameters of the confocal volumes in SIL-FCS experiments. The present model can be used for characterizing any SIL based system with improved resolution and contrast for conventional and confocal microscopy.

2.10 Appendix: Analysis 1

Principle: For an incoming wavefront denoted by the surface $S(\mathbf{r})$, which has the same phase retardation across the entire space, the wavefront aberration is defined by the deviation from a reference plane of the optical element. The deviation dS is expressed in polar coordinates using $z = S(r,\varphi)$ [57]. The differential between the reference and the aberrated wavefront takes into account not only the deviation but also the direction as well.

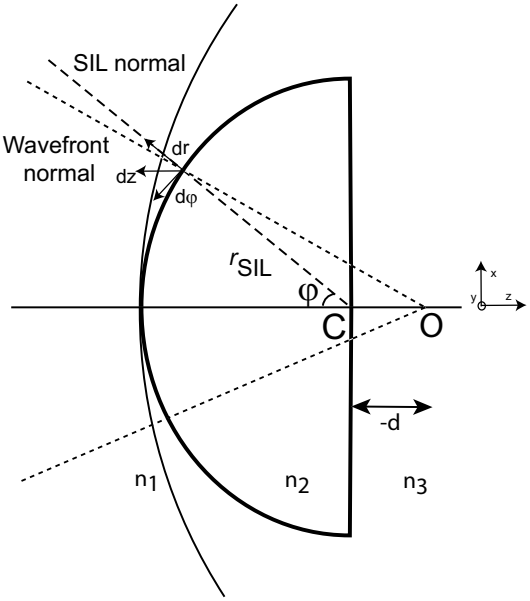

Figure 2.10: Beam propagation and the corresponding difference due to the projection vectors between the normals.

The equation for the surface of the reference wavefront corresponding to the ideal wavefront over the SIL surface is given by (see Fig.2.10)

$$\begin{aligned} z =& S(r,\varphi) \\ =& -r_{\mathrm{SIL}}\cos\varphi + \mathrm{d} \end{aligned} \tag{2.46}$$

The differential over the reference wavefront is then given by

$$dz_{ref} = dS_{ref} = -\cos\varphi dr + r_{\mathrm{SIL}}\sin\varphi d\varphi \tag{2.47}$$

The equation for the surface of the aberrated wavefront is given by

$$\begin{aligned} z =& S_{abrrt} \\ =& -(r_{\mathrm{SIL}} + \mathrm{d})\cos\varphi \end{aligned} \tag{2.48}$$

The differential over the aberrated wavefront is now given by

$$dz_{abrrt} = dS_{abrrt} = -\cos\varphi dr + (r_{\mathrm{SIL}} + d)\sin\varphi d\varphi \tag{2.49}$$

The difference between Eqs.2.47 and 2.49 gives the mismatch between the incident spherical wavefront and the SIL spherical surface.

$$dS_{abrrt} - dS_{ref} = d\sin\varphi d\varphi \tag{2.50}$$

We therefore see that the mismatch in the wave fronts is essentially a function of the incident angle and its differential. For the SIL case, the refraction at the SIL spherical interface gives

$$\begin{aligned} n_1 \sin\varphi &= n_2 \sin(\varphi + d\varphi) \\ &= n_2 \sin(\varphi) \quad \text{for} \quad \mathrm{d} \ll r_{\mathrm{SIL}} \end{aligned} \tag{2.51}$$

Therefore the mismatch between a converging spherical wavefront on the SIL spherical interface can be ignored for small values of d.

2.11 Appendix: Analysis 2

Defocus aberration due to the SIL spherical interface

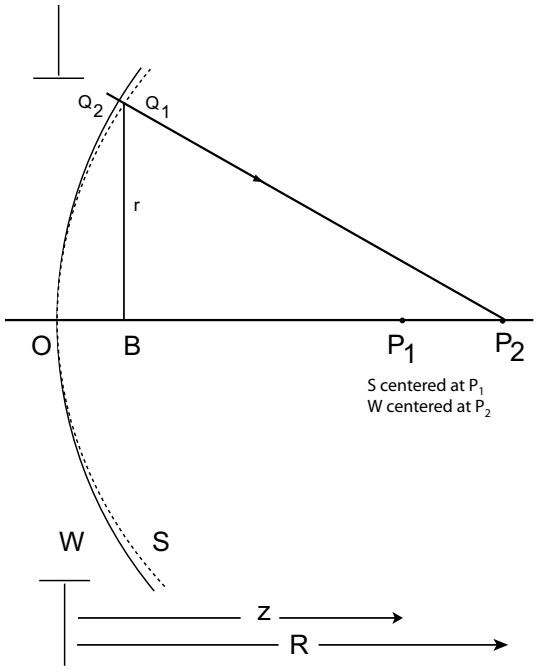

Figure 2.11: Defocused wavefront W is spherical with a radius of curvature R centered at P_2. The reference sphere S with a radius of curvature z is centered at P_1. Both W and S pass through the center O of the exit pupil. The ray Q_2P_2 is normal to the wavefront at Q_2.

A defocus aberration is introduced when the image is observed at a plane other that the Gaussian image plane. For the Gaussian image located at the point P_2, if

the image is observed at the point P_1, then for the observed image to be aberration free, the wavefront at the exit pupil must be spherical with its centre of curvature at P1. Such a wavefront forms the reference sphere with respect to which the aberration of the actual wavefront must be defined (see Fig. 2.11). Therefore the aberration at a point Q_1 on the reference sphere is given by

$$\begin{aligned} W(r) =& \frac{n}{2}\left(\frac{1}{z}-\frac{1}{R}\right)a^2\rho^2 \\ =& L_d\rho^2 \end{aligned} \tag{2.52}$$

where,$\rho = r/a$ Therefore, the overall wavefront aberration of the SIL system is given by

$$\Phi(\theta_1) = L_d\rho^2 + \Big[n_3\cos(\theta_3) - n_2\cos(\theta_2)\Big] \tag{2.53}$$

Wherein, the contribution from the spherical interface is essentially a longitudinal defocus term which remains constant in the entire analysis and is also negligible when compared to the planar interface term. We therefore finally have Eq. 2.28 as

$$\Phi(\theta_1) \approx d\Big[n_3\cos(\theta_3) - n_2\cos(\theta_2)\Big] \tag{2.54}$$

Chapter 3

SIL- Fluorescence Correlation Spectroscopy (SIL-FCS)

3.1 Introduction

In this chapter we give an overview of various concepts of FCS as relevant to situations encountered during the experiments. It is commonly assumed that the observation volume in FCS is Gaussian in three dimensions. However we show in the case of the SIL-FCS measurement conditions that this approximation is inaccurate.

3.2 FCS Theory

The technique is based on the observation of the fluorescence $\mathbf{F}(t)$ produced by dilute fluorescent species (nM concentrations) that diffuse in liquid solution. The resultant fluctuations $\delta\mathbf{F}(t) = \mathbf{F}(t) - \langle \mathbf{F}(t) \rangle$ of time average $\langle \mathbf{F}(t) \rangle$ carry information on the interactions that generate the observed variations in the induced optical response [47].

This information is revealed in the shape of the following intensity correlation. For the general case the auto-correlation function can be expressed as:

$$G_{total}(\tau) = \frac{\langle I(t+\tau)I(\tau) \rangle}{\langle I(\tau) \rangle^2} \tag{3.1}$$

The brackets $\langle\rangle$ denote the time average; I is the fluorescence signal as a function of time and τ is the delay time. Analysis of the correlation function reveals information about the dynamic processes (transversal and rotational diffusion) and kinetic processes (e.g. singlet-triplet transition) of the fluorescent molecules. The analytical expression for one species of freely diffusing molecules can be written as:

$$G(\tau) = 1 + \frac{1}{N}\left(1 + \frac{\tau}{\tau_D}\right)^{-1}\left(1 + \frac{\tau}{\omega^2\tau_D}\right)^{-1/2}\left[1 + \frac{p}{1-p}\exp\left(\frac{-\tau}{\tau_t}\right)\right] \tag{3.2}$$

Here, N is the average number of molecules present in the detection volume element, τ_D denotes the average diffusion time of molecules across the sampling region, ω is the ratio of the axial to radial dimensions ($\omega = \omega_z/\omega_{xy}$) of the detection volume element, p is the fraction of dye molecules residing in the longer living triplet state, and τ_T is the related relaxation time. Autocorrelation and volume are related in the limit $\tau \to 0$, where

$$G_D(\tau \to 0) = 1/N = 1/C_0V \tag{3.3}$$

and C_0 is a spatially constant concentration of molecules in the observation volume of size V.

Using the fact that $G_D(0)^{-1} = N$ and $C_0 = N/V$, the physical volume of the observation volume V can be determined from an FCS measurement at known concentration C_0, or for a known observation volume an absolute concentration can be obtained. In order to achieve a high signal-to-noise ratio (SNR), the confinement of the excitation field plays an important role. Raman scattered light is minimized and the fluorescent signal of the molecules can better be discriminated against the background. An experimental measure of the signal-to-noise ratio is typically given by the count rate per molecule (CPM). For higher concentrations of dye-labelled molecules in FCS, the higher confinement can be of advantage, since the amplitude of the autocorrelation, which is inversely proportional to the number of molecules, N (Eq. 3.2), increases as well.

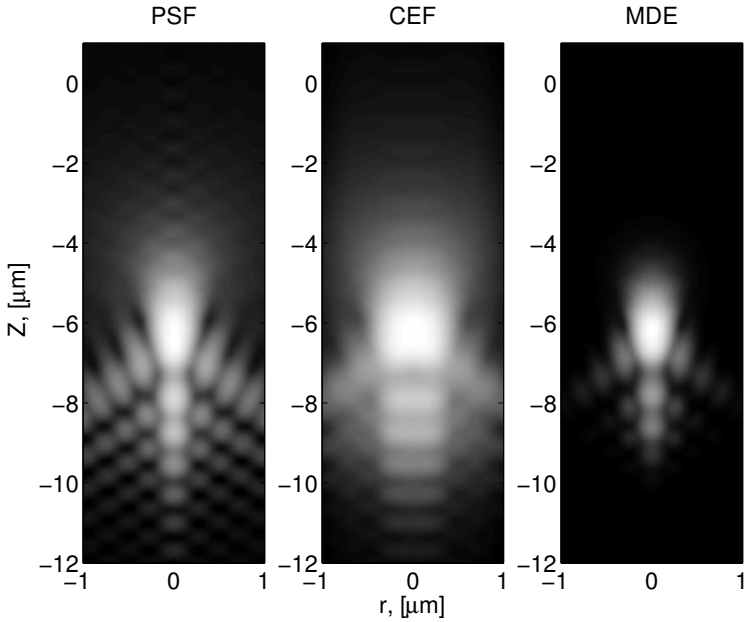

Figure 3.1: The normalized PSF, CEF and the MDE for the linearly polarized SIL-FCS with an axial focusing at d = 15μm. A 0.6NA, 40$\times$ air objective was used to focus 0.5μm into solution from the SIL planar surface. A pinhole diameter of 50μm was assumed in both cases. The excitation wavelength was 488 nm and the fluorescence emission wavelength was 542 nm.

The autocorrelation function (ACF) is shaped by different properties of the fluorescing molecules; on a nanosecond timescale, the ACF shows a steep rise

from zero to some maximum within the fluorescence lifetime. This photon antibunching reflects the fact that, after the emission of a photon, a molecule needs to become re-excited and to spend some time in the excited state before it can emit the next photon [58]. On the nano- to microsecond timescale, the ACF may be influenced by the rotational diffusion of the molecule [59]. On a microsecond timescale, the ACF is dominated by fast processes such as triplet-state dynamics or photo-isomerization [60]. On a millisecond to second timescale, the ACF decays because molecules leave the detection region by diffusion.

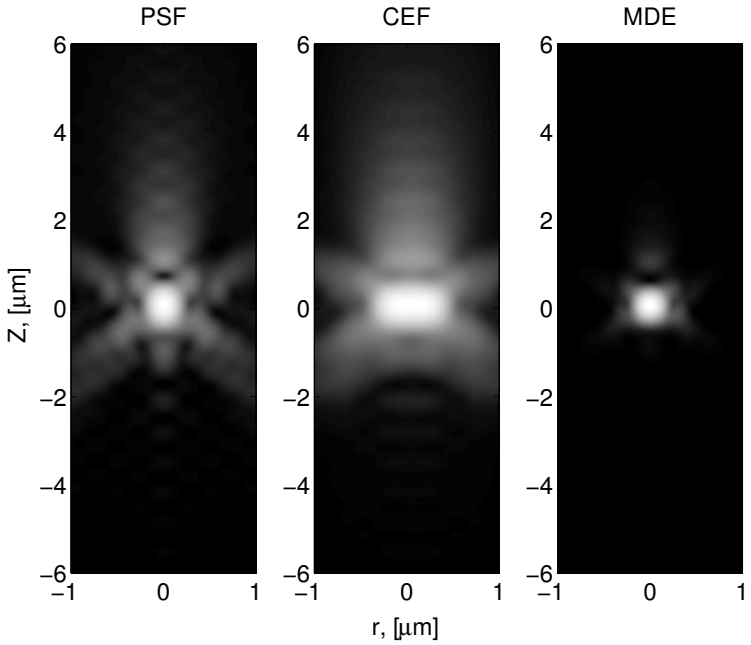

Figure 3.2: The normalized PSF,CEF and the MDE for the linearly polarized SIL-FCS with an axial focusing at d = 15μm with suitable aberration compensation. A 0.6NA, 40$\times$ air objective was used to focus 0.5μm into solution from the SIL planar surface. A pinhole diameter of 50μm was assumed in both cases. The excitation wavelength was 488 nm and the fluorescence emission wavelength was 542 nm.

The shape of the ACF due to diffusion is determined by the molecule detection efficiency function (MDE) and by the diffusion coefficient of the molecules. The amplitude of the ACF is determined by the concentration of molecules. The MDE quantifies the efficiency with which a photon is detected from a fluorescing molecule. The MDE depends on the intensity distribution of the focused laser light and on the efficiency of detecting a photon from its point of origin, but also on the photophysics of the fluorescing molecules and on their rotational diffusion. These factors enter the MDE in a complicated way that does not generally allow the factoring the MDE into a pure excitation and a pure emission part.

The MDE therefore describes the spatial changes in the induced fluorescence and combines the so called collection efficiency function $CEF(\mathbf{r})$ and the intensity excitation profile $I(\mathbf{r})$:

$$MDE(\mathbf{r}) = CEF(\mathbf{r})I(\mathbf{r}) \tag{3.4}$$

More interesting for FCS is the enhancement of the count rate per molecule. To give some quantitative estimate of this rate we compare the effective observation volume element given by the following integral that is evaluated over all three spatial dimensions [61].

$$V_{eff} = \frac{\left[\int MDE(\mathbf{r})\mathrm{d}\mathbf{r} \right]^2}{\int MDE^2(\mathbf{r})\mathrm{d}\mathbf{r}} \tag{3.5}$$

The size of this focal volume therefore has a direct effect on the number of molecules in the sampling volume and is a key parameter for enabling effective SNRs in an FCS experiment [22].

Fig.3.1 and Fig.3.2 gives us the computed CEF and MDE for the SIL-FCS cases as described in Chapter 2.

3.2.1 Imaging of an electric dipole

For calculating the MDE, it also becomes important to consider theoretically the image of a fluorescent point object. This can then be regarded as the intensity point spread function for the overall imaging process. The strength of excitation is given by the component of the electric field in the direction of the dipole axis. The image for arbitrary orientation of the dipole can then be calculated. In practice, the dipole can rotate between excitation and emission. Here one can consider two limiting cases: the first where the dipole orientations at excitation and emission are unrelated (case A), and the second where they are assumed equal (case B). The first could be applicable for dye molecules in solution (as in the case for the SIL-FCS), whereas the second describes the behaviour of a dye molecule fixed in space (for surface FCS measurements). Finally, one can average over all possible orientations to obtain an averaged intensity point spread function.

For the case when the fluorescent molecule can rotate freely between excitation and emission (case A), the orientation of the dipole is not related to the illumination field. Thus for many dye molecules, which can be arbitrarily oriented, we can average over a complete sphere. Eqs.(2.23-2.25) can then be transformed to give the intensity expression as:

$$I_{av} = \int_0^{\pi} \int_0^{2\pi} |E|^2 \, sin\theta_1 d\phi d\theta_1 \tag{3.6}$$

This is illustrated in the Fig .3.1 and Fig .3.2 for the case of the SIL, when the wavelength of emission is 542 nm. This is equivalent to the treatment for obtaining the PSF in the focal region of a lens illuminated by an unpolarized wave [62].

3.2.2 Non-Gaussian SIL Observation Volumes

In most publications on FCS, the MDE is assumed to have a three-dimensional (3D) Gaussian shape (Fig. 3.3) [45]. This assumption significantly simplifies the

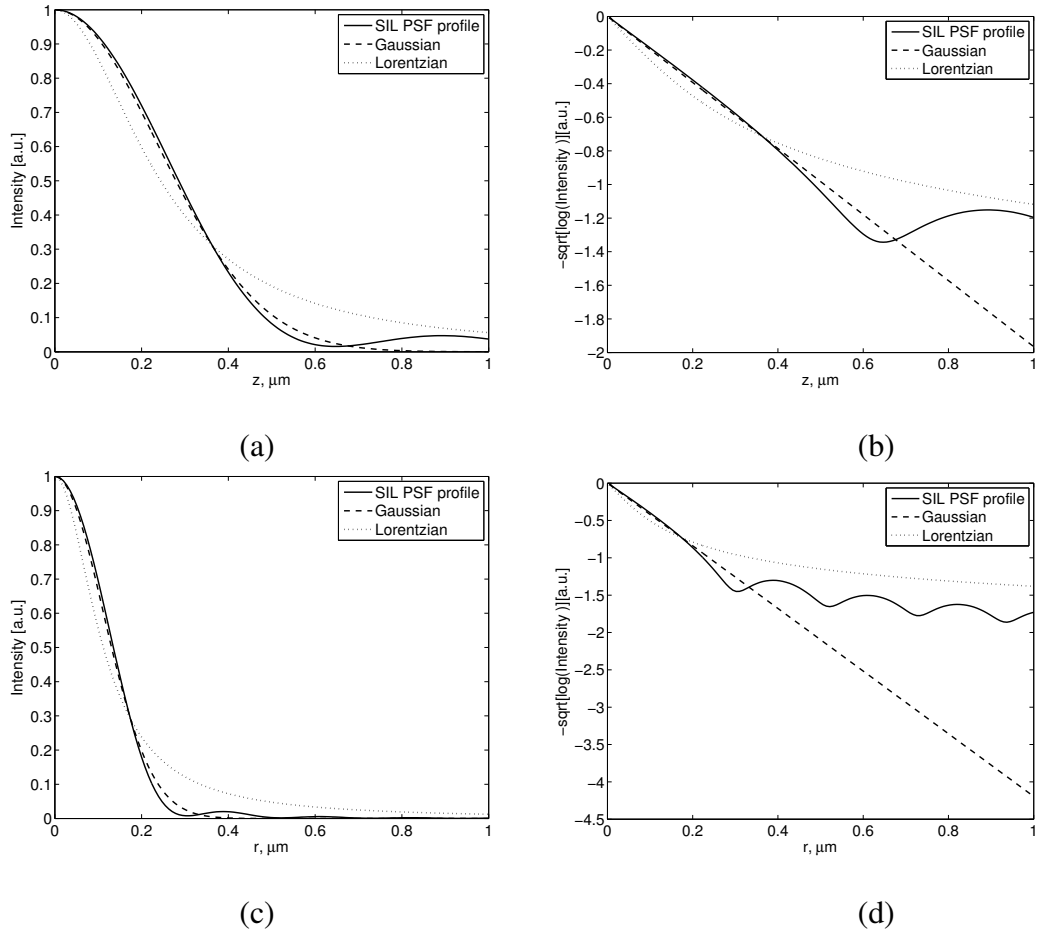

Figure 3.3: The calculated PSF profile for linearly polarized light (solid line) is fit with a Lorentzian (dotted line) and Gaussian (dashed line) on a linear (left) and logarithmic (right) intensity scale, [-log(intensity)]$^{0.5}$, which should yield a straight line for all positions if the profile is Gaussian.

calculation of the autocorrelation function, but represents the experimental situation rather imprecisely. Fig. 3.3 shows the axial plot of the MDE profile which indicates that the functional form is neither Gaussian nor Lorentzian in the axial or lateral direction. In general, the Gaussian fits well at short distances from the focus, but decays too quickly at large distances. Furthermore, because the fringes are at such large distances from the focus, they occupy a significant volume due to the approximate axial symmetry of the system, and can have a strong influence on the measured volume and autocorrelation in FCS.

3.3 SIL-FCS: Experimental Implementation

The experimental set-up for FCS measurements with the SIL is based on a standard confocal microscope ConfoCor from Carl Zeiss (see Fig. 3.4). The SIL with radius of 0.7 mm was made of LaSF35 glass ($n = 2.02$ at 633 nm). Rhodamine Green at 10nM concentration were dispersed in a droplet on a cover glass, for the water immersion objective, or directly on the plane surface of the SIL. The mole-

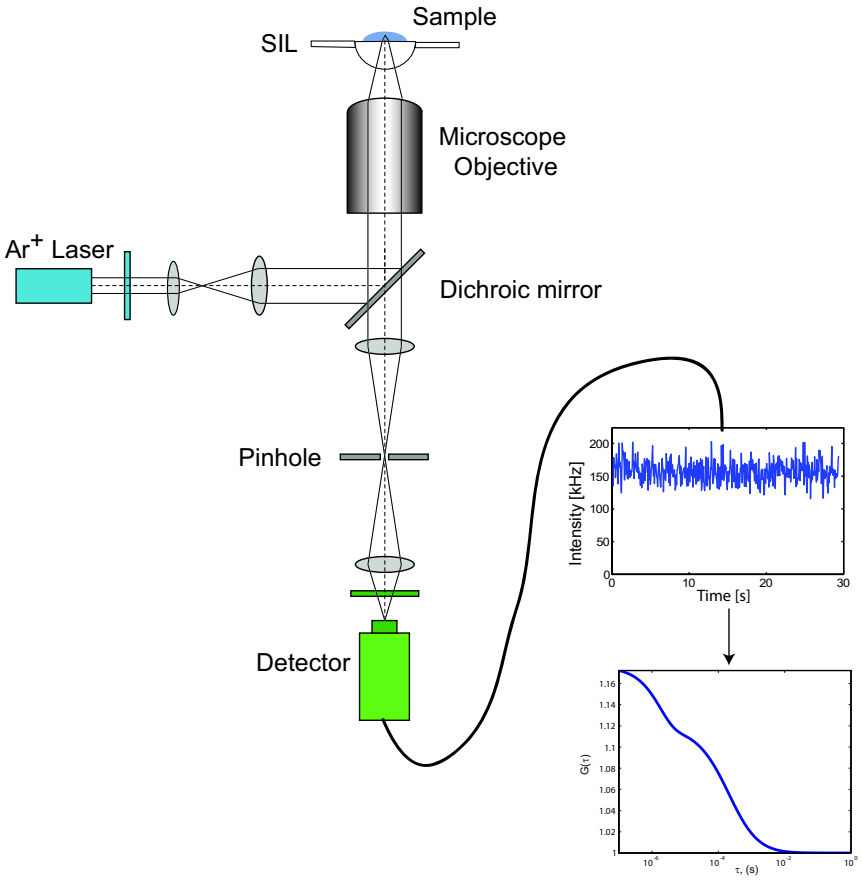

Figure 3.4: Schematic of the SIL-FCS setup is shown. A laser is focused by a air objective (NA=0.6 or 0.8 typically) into the SIL and excites the dye sample or the model system under investigation on the SIL planar surface. Essentially an epi-illumination setup, the emitted fluorescence is separated from the excitation light by the dichroic mirror and is then spatially filtered by a pinhole. The light is focused onto a detector which counts the incoming photons in fixed time intervals. This intensity signal is then autocorrelated as shown in the lower part of the figure. From the autocorrelation function one can deduce different parameters depending on the underlying physical process that causes fluctuations in the fluorescence intensity.

cules were excited with a linearly polarized Ar^+ laser at 488 nm. The fluorescent response was detected with an avalanche photo diode (Single Photon Counting Module from Perkin Elmer) and processed with a hardware correlator having 288 channels.

The obtained data (see Fig. 3.5) was then analyzed with a fit based on the non-linear Marquardt-Levenberg algorithm (Chapter 5) that allows extracting the number of molecules, N, the diffusion time,τ_D, of the molecules, the fraction of molecules in the triplet state, T, and the relaxation time,τ_T; see (Eq. 3.2). Two different microscope objectives were used for experiments. For the conventional FCS reference measurements, a 40x/1.15 Olympus, Uapo/340 (cover slide corrected), water immersion objective was used. The optimum CPM value for this

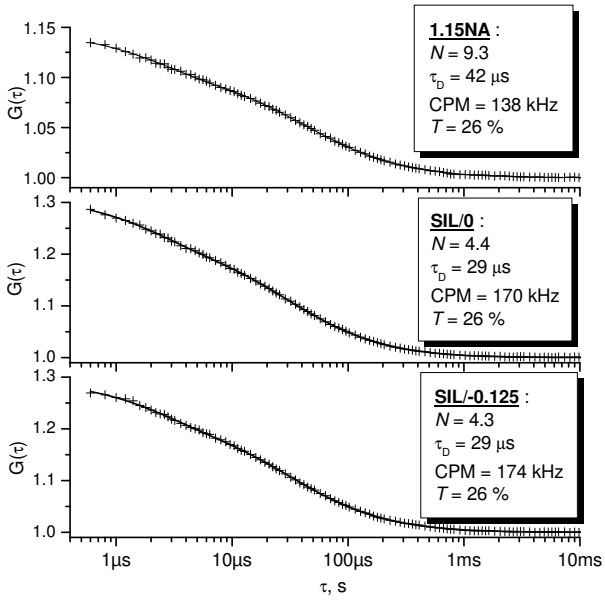

Figure 3.5: Typical FCS correlation curves of Rhodamine Green at 10nM concentrations obtained with 1.15NA objective; SIL and 0.6NA objective with "-0.125 mm" setting; SIL and 0.6NA objective with "0 mm" setting. The "crosses" are the measured data; the solid line represents the fit. For more details, refer [18].

high NA system was found to be typically at 140kHz. For the SIL-FCS set-up a LD Achroplan 40x/0.60 Korr, Zeiss air objective was used with a working distance of 1.8 mm, which enabled the positioning of the SIL lens.

3.4 Discussion

We clearly see that the SIL-FCS setup represents a marked improvement over existing conventional set-ups. Apart from providing the optical advantage of a tighter focal volume it paves the way for temperature controlled not only in FCS but in general for other Single Molecule Detection experiments as well.

Chapter 4

SIL Thermal Chamber

4.1 Introduction

Many FCS applications require temperature variation studies [63, 64] and utilize various commercial or home-made systems. In hybridisation studies [65, 66], the ability of denatured DNA to reanneal with complementary strands in an environment is just below their melting point (T_m) [67]. Several thermal chambers have been designed in the past for various applications and are now a standard accessory for imaging and spectroscopy studies [68–71]. The basic principle in many of these sample compartments is that it is placed in a temperature controlled holder. The temperature is then applied from the top or by the side using a Peltier element (also called TEC-thermo electric cooler). To ensure temperature stability, the high NA water immersion objective is also heated up by winding a plastic tube around it and by pumping tempered water through the tube. This approach does not thermally insulate the heated sample from the microscope body which acts as a temperature sink. This approach is also fraught with the risks of loss in focus position requiring subsequent realignment and also potential damage to the optics of the microscope objective [19]. To circumvent these basic disadvantages in temperature based FCS experiments, we present a new sample holder which combines the dual advantage of giving high collection efficiency due to the high system NA (> 1.2) as needed for FCS experiments as well as achieving the thermal decoupling by using a SIL in an air gap with a low NA objective. The SIL temperature module has been designed to meet the following considerations:

- maximum aperture of the excitation and emission window,
- well-defined sample volume and
- convenience of operation.

4.2 Preliminaries

In this chapter the detailed characteristics of the SIL thermal chamber is presented. Details of the mechanical design, thermal characterization tests on Rhodamine Green dye samples and finally measurements on the model bio-chemical systems

chosen, *i.e.*, vesicles made from phospholipids encapsulating Alexa Fluor 488 hydrazide (AEV) (henceforth called as vesicles) are presented.The validity of the diffusion data is fitted and explained with the Stokes-Einstein (SE) relationship at the molecular level. The phase transition of vesicles and its dependence on temperature is gainfully exploited for highlighting the specific advantage of the SIL technique.

4.3 Mechanical Design

The temperature controlled module consists of the h-SIL lens glued into a thin Alumina (Al_2O_3) plate of 170μm thickness with glue. This plate is inserted on another alumina stage which acts like the common base for the whole module (see Fig. 4.1).

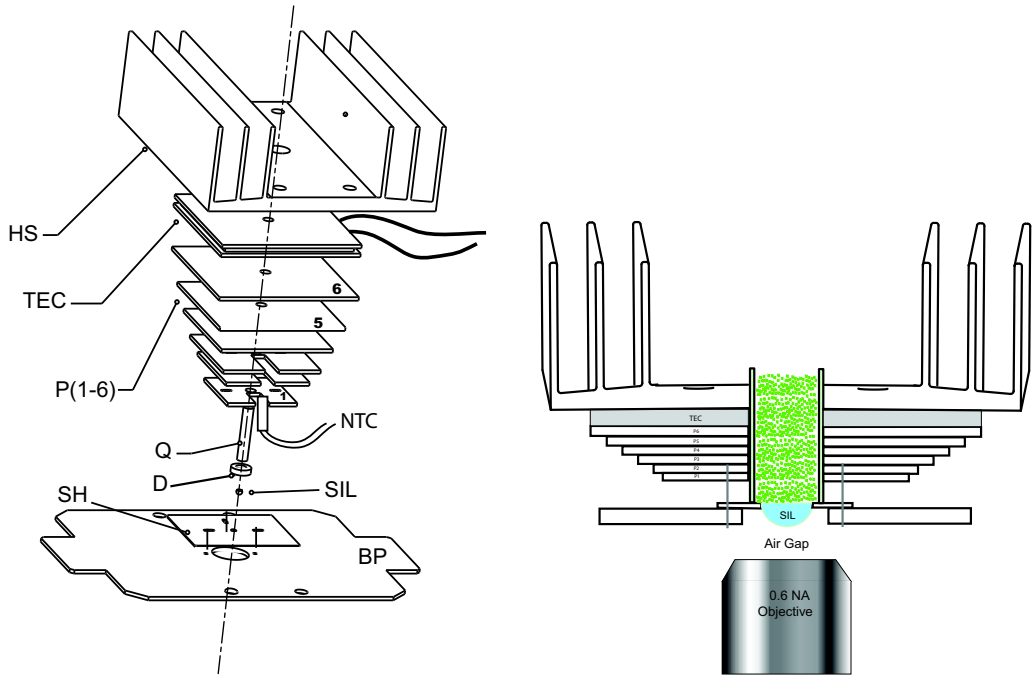

(a) (b)

Figure 4.1: Schematic of the SIL temperature module. a) Exploded view of SIL Temperature Module and b) Complete Assembly. BP, Base plate; SH, Alumina Foil SIL holder (170 μm);SIL, Solid Immersion Lens; D, Circular Disc; Q, Quartz tube; NTC, Thermistor; P(1-6), Alumina Pyramid glued together from individual alumina plates of varying dimensions for effective heat transfer; TEC, Thermo Electric Cooler or Annular Peltier element; HS, Heat sink. b) Vertical cross-section of the module with respect to microscope body (dimensions not to scale).

It has a central opening for the objective aperture and has three pins in a symmetric triangular way to guide the SIL Alumina foil onto it for every measurement session. This ensures mechanical stability of the whole system. The SIL Alumina foil is therefore guided by the pins (1mm long). To ensure heating of only the

sample volume and not the whole SIL plate, a heat pyramid with a central opening was also designed to ensure overall thermal conduction without being in contact with the SIL plate or the microscope body. This pyramid was positioned on the three pins and ensured repeatability in terms of mechanical precision of positioning for every measurement session. A tube made of synthetic quartz (inner diameter = 2.425mm, outer diameter = 3.00mm and mean expansion coefficient $= 5.1 \times 10^{-7}$, Polymicro Technologies, U.S.A.) of length 16.5mm was used for confining the sample volume to around 50μl. This tube was inserted into a circular disc made of polyoxymethylene (POM) to hold the tube tightly preventing leakage. Evaporation loss tests carried out on solutions indicated a loss of around 10μl over a span of one hour of heating upto 85°C. This pyramid was glued using a thermally conducting glue to a annular Thermoelectric cooler (TEC) (SH1.0-95-06L, Melcor Corporation, U.S.A.) The TEC was operated by a temperature controller (MPT-2500, Wavelength Electronics, U.S.A.) with a control loop from a NTC (negative temperature coefficient) thermistor ensuring stabilization and operated within 22 to 85°C with an estimated error of 1°C.

This module is stable at higher temperatures enabling long measurement times, ease of handling and cleaning of the SIL surface. The maximum evaporation loss in sample for a typical experimental run for one hour involving the time for temperature stabilization for around 100 consecutive measurements of measuring time of 20 sec each was 30%.

The sampling volume on top of the SIL was therefore heated adequately and was thermally insulated effectively from the ambient laboratory environment. The calibration of the current on the TECs was done to ensure heating accuracy taking into account the heat gradient from the TEC hot side down to region around the SIL planar surface. A precise determination of temperature dependence variation on the length and good contact with the silica micro tube and the alumina pyramid was done before proceeding to temperature measurements. The temperature on surface of the SIL was measured with a digital thermometer during the calibration taking into account the overall temperature drift and the convection gradient along the tube down to the SIL surface.

4.4 Diffusion and Stokes-Einstein relation

4.4.1 Measurements on Rhodamine Green (10nM)

The translational diffusion coefficient (D) of a particle in a viscous medium is given by the Stokes-Einstein equation:

$$D = \frac{k_B T}{6\pi\eta R_h}, \tag{4.1}$$

where k_B is the Boltzmann constant, R_h is the hydrodynamic radius, T the temperature and $\eta(T)$ the viscosity. The diffusion time, $\tau_D(T)$ in FCS is related to the diffusion coefficient as:

$$\tau_D = \frac{\omega^2}{4D}, \tag{4.2}$$

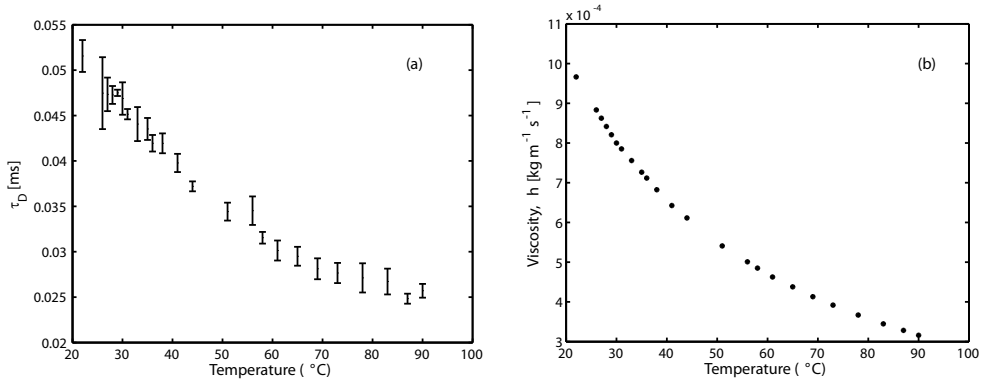

Figure 4.2: (a) The variation of diffusion time (τ_d) with increasing temperature for Rhodamine Green at 10nM concentrations obtained with SIL + 0.6NA objective. The error bars indicate the range of fit values obtained from the measurements at a particular temperature setting. (b) The variation of viscosity with temperature [72].

where ω is the structure parameter of the sampling volume. Therefore, in the first order,

$$\tau_D \propto \frac{1}{T}, \tag{4.3}$$

neglecting the temperature dependence of $\tau_D = f(\eta(T))$. The data in Fig. 4.2a and Fig. 4.2b (obtained from literature) show that the variation of τ_D and η are proportional in behavior. We therefore can extract the relation between τ_D and T from the autocorrelation curves as measured in an FCS experiment.

From Fig. 4.3 we see that the number of molecules (N) increase and the CPMs decrease from around 60° onwards, indicating the effect of evaporation as well as the presence of thermal gradient in the quartz tube. The corresponding behavior for the triplet fractions is that it also increases slightly at higher temperatures. Figs. 4.2 and 4.3 represent a global view of the experimental data wherein temperature is the only varying parameter. The laser excitation intensity was constant throughout the measurements.

Assuming that the RhG molecules are photochemically intact, the thermal dependence of the fluorescence quantum yield ϕ and lifetime τ is modified due to the higher rate of collisions *i.e.*, dynamic quenching due to temperature effects on the fluorophore lifetime and on molecular mobilities. In a solution containing only one solute (RhG in this case), the fluorescence quantum yield and lifetime are given by

$$\phi_0 = k_f \tau_0, \qquad \text{and} \tag{4.4}$$

$$\tau_0 = (k_f + k_{nr})^{-1}, \tag{4.5}$$

where k_f and k_{nr} are the rate constants of emission and/or non-radiative deactivation respectively. Extensive studies in literature have shown that temperature has

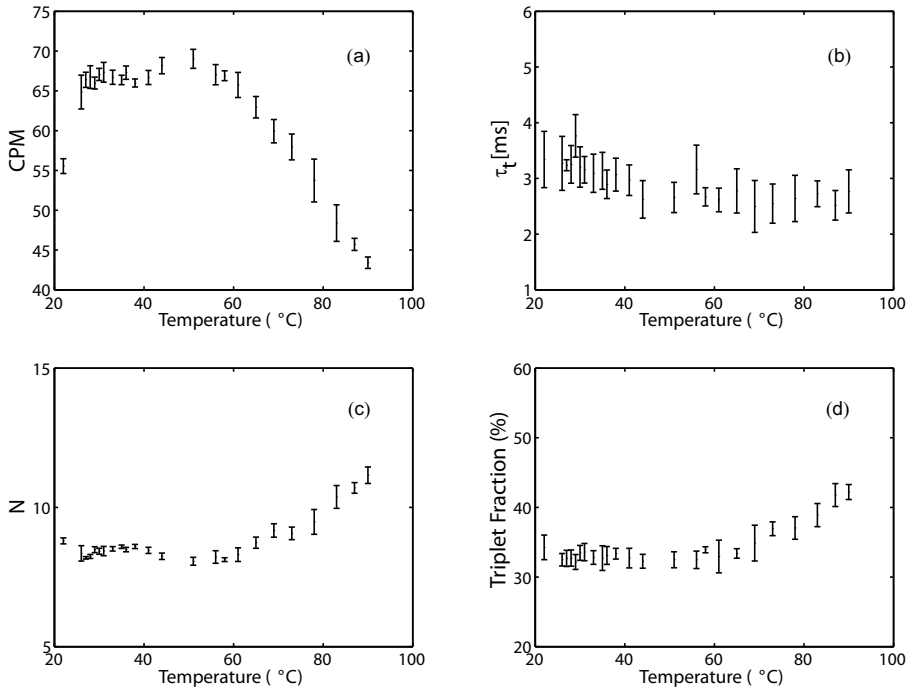

Figure 4.3: The variation of (a) Counts per Molecule (CPM) (b) Triplet time (c) Number of molecules (N) and (d) Triplet Fraction with increasing temperature for Rhodamine Green at 10nM concentrations obtained with SIL + 0.6NA objective. The error bars indicate the range of fit values obtained from the measurements at a particular temperature setting.

practically no influence on the emission rate but affects the efficiencies of intersystem crossing to the triplet state and/or internal conversion to the ground state. Morever, collisional quenching of the triplet state by oxygen molecules in an air-saturated solution is for most dyes the main deactivation pathway of their triplet states and also enhances the rate of intersystem crossing [73].

The data in 4.3a therefore indicates two competing processes. *i.e.*, on lifetime and quenching efficiency [74]. The first part of the curve till around 60° corresponds to an increase in the relaxation rates due to an increase in temperature thereby increasing the fluorescence emission till a certain build up of the activation energy. This decrease in fluorophore lifetime thereby reduces the probability of further encounters with any quenching mechanism in the system.

However, molecular mobility simultaneously increases the quenching efficiency in the system. Generally an increase in temperature increases the non-radiative processes such as collisions with solvent molecules, intramolecular vibrations and rotations. This process is seen to dominate in the second part of the curve after 60°. Temperature is therefore a useful parameter for quantification of this phenomenon and shows insights into the activation energy for diffusion.

4.5 Fluorescence and Quenching of Dyes

The transitions involved in the absorption of visible light by fluorescent dyes are those from the electronic ground state S_0 to the first excited singlet state S_1. Relaxation of the system back to the ground state may occur by emission of a fluorescence photon or by non-radiative decay processes in which the excess energy is dissipated in the form of heat via vibrational, rotational and translational modes of the system. Another possible relaxation mechanism involves chemical reactions occurring in the excited state, which will not be discussed here. Electronic transitions of a molecular system upon absorption or emission of photons occur on timescales which are much faster (about 10^{-15} s) than the response of the nuclei (Franck- Condon principle). For this reason, the absorption and emission spectra of most molecules exhibit broad band structures, indeed the rotationally and vibrationally excited states, which depend only on the nuclear degrees of freedom have longer decay times than the electronically excited states, therefore electronic transitions may occur between many different vibrational and rotational states. This fact is illustrated in the absorption and emission spectra of the fluorescent probe RhG [75]. At room temperature, molecules generally occupy the electronic and vibrational ground-state. Upon light absorption the molecule finds itself in a vibrationally excited state of one of the electronically excited levels. This electronic state is generally the first excited singlet state S_1. Excitations into S_2 and higher singlet states also occur, but these generally decay rapidly ($10^{-11} - 10^{-13}$)s in a non-radiative fashion into the S_0 state. After excitation into a vibrationally excited state of S_1, the molecule relaxes to the vibrational ground-state by collisions with surrounding molecules in a time scale of the order of 10^{-12} s. Subsequently, different radiative and non-radiative relaxation processes are possible, these are illustrated in the schematic Jablonski diagram of Fig. 4.4.

From the vibrational ground state of the S_1 state, radiative relaxation to vibrationally excited S_0 levels can occur by spontaneous emission of a fluorescence photon. As vibrational relaxation of the electronically excited state takes place prior to photon emission, and as the accompanied electronic relaxation goes to vibrationally excited states, the fluorescence photon has a lower energy compared to the absorbed photon, *i.e.*, the emission spectrum exhibits a bathochromic shift - the so-called Stokes shift respect to the emission spectrum. The remaining energy in the vibrationally excited S_0 state is again dissipated in the form of heat by collisions with the surrounding medium. The Stokes shift is crucial for the high sensitivity of fluorescence spectroscopy because the fluorescence light can be separated efficiently from Rayleigh and Raman scattering using optical filtering systems.

The non-radiative decay from the lowest vibrational state of electronically excited states to vibrationally and rotationally excited electronic ground-states is called internal conversion (IC) and is mostly responsible for the loss of fluorescence efficiency of organic dyes. Depending on the molecular structure of the dye and the properties of the solvent, the rate of relaxation by IC can vary by many orders of magnitude. Besides the non-radiative decay directly to the ground-state, a molecule in the S_1 state may enter the system of triplet states and relax to the lowest triplet level T_1 , this process is called intersystem crossing (ISC). Transitions involving ISC are spin-forbidden, but have a non-zero probability due to spinorbit

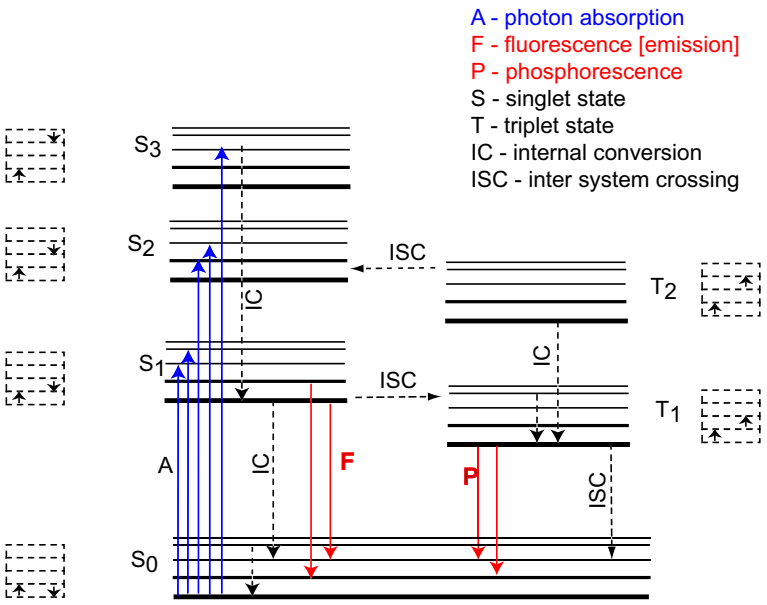

Figure 4.4: Schematic Jablonski-diagram illustrating different radiative and non-radiative processes. Full lines show processes of light emission (red) or absorption (blue), dotted lines show non-radiative processes. Internal conversion processes (IC) occur between energy levels with the same spin multiplicity, Intersystem crossing (ISC) requires spin flip.

coupling. $S_1 \longrightarrow T_1$ transitions are energetically always possible because the first excited triplet state always has lower energy compared to the first excited singlet state. From the vibronic ground state of the first excited triplet state T_1 the molecule can relax in a nonradiative fashion by ISC or by the emission of a phosphorescence photon. As this is again a spin forbidden process with low probability, the rate constant for phosphorescence is several orders of magnitude smaller than that of S_1 states and T_1 states have characteristic lifetimes of $10^{-6} - 10^{-3}$s. The preceding considerations concerned absorption and emission characteristics of a single molecule.

Dynamic and Static Fluorescence Quenching

Interactions of the dye in the fluorescent state with surrounding molecules may cause fluorescence quenching.In general, fluorescence quenching processes can be divided into two classes: dynamic and static quenching. In the dynamic quenching model, a quencher molecule collides by diffusion with the fluorophore during the excited-state lifetime. An encounter complex is formed. Upon formation of the encounter complex, the fluorophore relaxes non-radiatively to the electronic ground-state. This type of dynamic quenching process is characterized by a reduction of both the measured fluorescence lifetime and the fluorescence intensity.

Static quenching is marked by the formation of a ground-state complexes between dye and quencher in equilibrium. The equilibrium between free compounds and complex is also assumed for the fluorophore in the excited state. The ground-state complexes are non- or only weakly fluorescent. Ground state complexes do not influence the measured fluorescence lifetime but only the fluorescence intensity (*i.e.*, the relative fluorescence quantum yield), this is due to the fact that the formation of ground-state complexes reduces the concentration of free fluorescent dye.

Besides measurement of fluorescence lifetimes, static and dynamic quenching can also be distinguished by specific temperature behavior. Dynamic quenching depends upon diffusion. Since higher temperatures results in larger diffusion coefficients, the bimolar quenching constants are expected to increase with increasing temperature. More specifically, the collision frequency is expected to be proportional to T/η since diffusion coefficients are proportional to this ratio (see Eq. 4.1). In contrast, increased temperature is likely to result in decreased stability of complexes, and thus lower values of the static quenching constants [76]. However, precise information about the actual fluorescence quenching mechanism cannot be extracted without appropriate control measurements. For the interpretation of fluorescence spectroscopic data, especially in bioanalytic applications, it is crucial to understand how changes in the microenvironment and interactions with surrounding molecular compounds influence the dye in the electronically excited state and thus its fluorescence properties.

4.6 Measurements on Lipid Vesicles

Lipid vesicles constitute nanocontainer systems (Fig. 4.5) ideally suited for the isolation, preservation, transport, and localization of few molecules [20], [77, 78]. FCS is the only technique that is able to distinguish encapsulated dyes from the released one, in particular under diluted conditions [19]. The specific advantage arising from the SIL-FCS technique is the possibility to analyze the *in situ* behavior of such systems at a given particular temperature.

4.6.1 Materials and methods

Negatively charged DPPG (1,2 Dipalmitoyl-sn-Glycerol-3-(Phospho-rac-(1- glycerol)) (Sodium Salt) purchased from Avanti Polar Lipids is used for the preparation of extruded unilamellar vesicles. 5 mg of the lipid powder is hydrated with 1mL of 3.17 μM of Alexa Fluor 488 hydrazide in buffer (Tris-HCl 10nM at pH 7.0 in order to control the pH and thus the charge of the lipids). The lipid solution is heated to $60°C$ and spontaneously form multilamellar vesicles (MLV). The dye entrapment efficiency is increase with 3 cycles of freeze-thaw in liquid nitrogen in 60°C water bath. The MLVs are then extruded by nitrogen pressure through polycarbonate membrane with 100nm pores size to produce small unilamellar vesicles with a homogenous size distribution of 100nm (which was also measured by dynamic light scattering (DLS)). Finally, the non-incorporated dyes

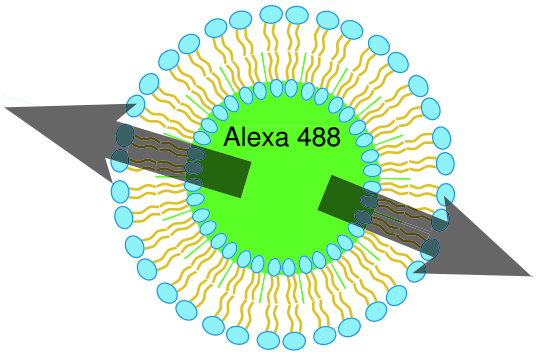

Figure 4.5: (a) Schematic presentation of the cross section of vesicles made from phospholipids together with added Alexa 488 which is entrapped inside. The arrows indicate the high permeability increase of the vesicle bilayer that comes from mismatching between neighbors lipid during the phase transition temperature. There is a high concentration gradient between the bulk solution and the interior of the loaded vesicles.

are removed by size exclusion chromatography (2 passages, with sephadex G75 from Sigma).

Intensity autocorrelation functions $G(\tau)$ of free Alexa and vesicles are shown in Fig. 4.6. Due to the differences in the diffusion times between free Alexa and vesicles it is possible to quantify the fractions between them (Table. (4.1)).

Table (4.1) summarizes the data values for the vesicle experiments.

4.6.2 Analysis

Fig. 4.6, shows FCS measurements performed to analyze the permeability of loaded vesicles as a function of the sample temperature. The reference (Part A) corresponds to the intensity fluctuation of free Alexa488 in solution without any vesicles. Part B shows intensity fluctuation of concentrated (1) and dilute (2) vesicles solution loaded with Alexa488 at room temperature. Part C represents the normalized autocorrelation curves summarizing different conditions: (1) For reference, the freely diffusing Alexa488 in solution without any vesicles. (2) Slow diffusing vesicles encapsulating Alexa488 at room temperature (3) Fast diffusing dyes released from the vesicles at $T > 41^{\circ}$C. Curve 3 is similar to curve 1, demonstrating an efficient dyes release in dilute conditions (dilution of 100 times after purification) due to a high concentration gradient between the bulk solution and the interior of loaded vesicles. The cartoon below summarizes the conditions corresponding to the different autocorrelation curves. Part (1) shows free Alex488. Part (2) represents the vesicles loaded with Alexa488 at temperature below the lipid phase transition, where the non-incorporated dyes are removed as described in the material section. Part (3) shows the same vesicles sample at a temperature higher than the lipid phase transition, where the dyes are released from the vesicles while heating through the lipid phase transition temperature. The high permeability increase of the vesicle bilayer comes from the mismatch between

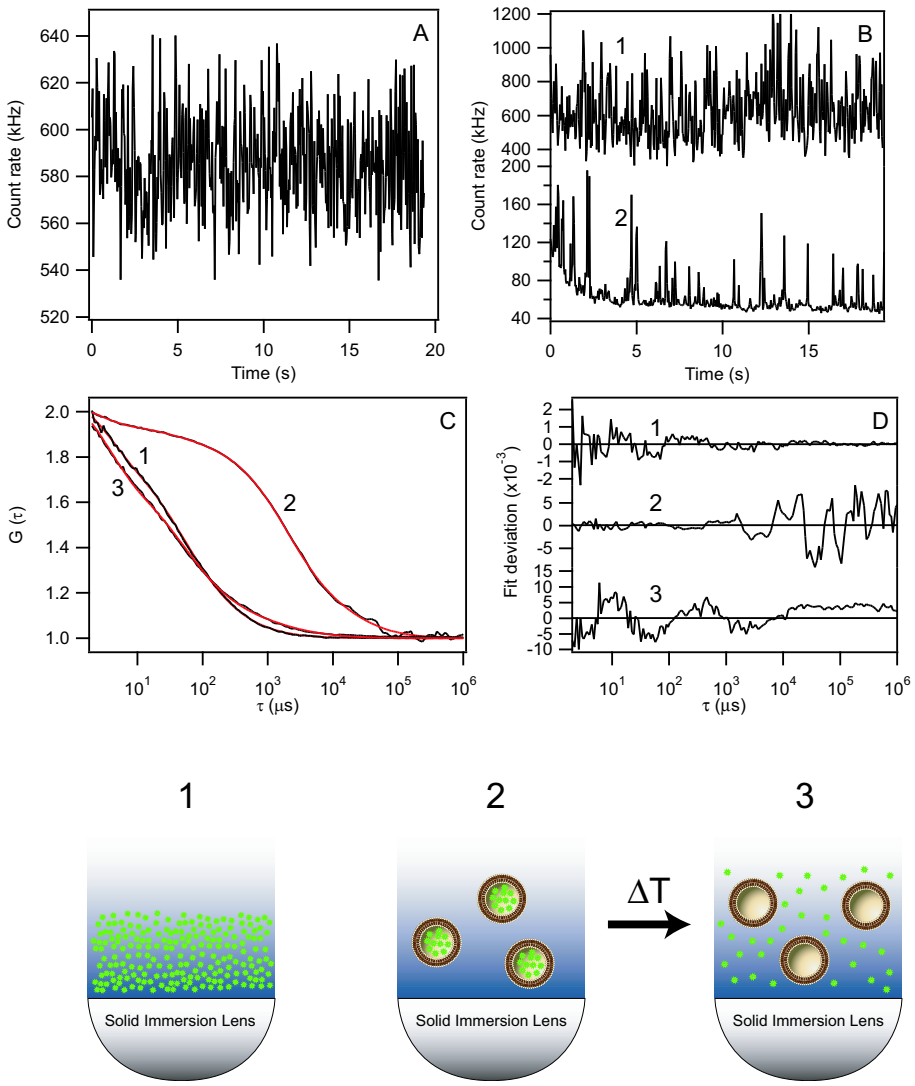

Figure 4.6: Measurement of fluorescent lipid vesicle permeability triggered by temperature increase as measured by SIL-FCS. Intensity fluctuations of (A) freely diffusing Alexa 488 FH, and (B) of lipid vesicles labelled with Alexa 488 FH, where (1) corresponds to a high concentration, and (2) to a low concentration of loaded vesicles. (C) Normalized autocorrelation curves obtained by SIL-FCS of (1) freely diffusing Alexa 488 FH, (2) lipid vesicles encapsulating Alexa 488 FH, and (3) solution acquired after dyes release triggered by a temperature increase (T $>$ 41°C). The red lines show the fit to the experimental data, and (D) the corresponding deviations of the fit. The dye release process is depicted in the cartoon where the numbering corresponds to that of the curves shown in (C) and (D).

neighbor lipids during the phase transition.

Table 4.1: Evaluation of fitting the autocorrelation curves of fluorescent dyes and vesicles.

Sample	Count Rate kHz	CPM kHz	N[a]	F_1[b], τ_{D1} %, μs	F_2 [b], τ_{D2} %, μs	F_3[b], τ_{D3} %, μs
Alexa 488 FH, 10 nM	586	55	12.5	92%, 50	8%, 445	N.A. [c]
Lipid Vesicles, before rupture	621	216	3.0	8%, 50	75%, 2783	17%, 34.2
Lipid Vesicles, after rupture	117	68	2.2	85%, 50	15%, 3905	N.A. [c]

[a]N, number of molecules/particles in detection volume.
[b]F_n, fraction of molecules/particles having a specific diffusion time.
[c]N.A., Not Applicable

4.7 Discussion

The SIL thermal chamber proves the feasibility of performing FCS/SMD experiments without having to heat up the microscope objective/body. It shows effectively the "proof of concept" for the SIL-FCS concept for biological measurements at the single molecule level. It eliminates the handling issues associated with heating a high NA objective by decoupling itself from the microscope body. The presented module incorporated design issues based on multi-functional considerations arising from the mechanical, thermal, optical, bio-chemical and liquid handling aspects as part of the system design. These results indicate that further experiments in studying conformational dynamics associated with protein folding, ligand binding and enzymatic catalysis, where accurate control of the sample-temperature is important becomes feasible with the SIL technique. The future outlook for further engineering research lies with the diffractive SIL [30] technology or designs similar to the Microfabricated SIL [35] or the SIL arrays [79]which can further be modified to the form that can be used like the Greiner 1536-Well CellStar Plates for fluorescence assays. Today's technology easily offers the possibility for realizing this. Its implications on high throughput screening methods are obvious.

Chapter 5

Stochastic Approach to Data Analysis in FCS

5.1 Introduction

What is the effect of fitting algorithms on FCS data? To what extent are they reliable and when do they appear to give artifacts causing wrong interpretation of experimental data? And are there ways to get around it without sacrificing on accuracy. This chapter seeks to present an alternate approach to the ones currently used in conventional FCS fitting. A "good" FCS set-up is typically made when the experimenter has taken into consideration the following criteria. *i.e.*, the type and numerical aperture (NA) of the objective lens, the size of the detector aperture, and the degree of underfilling of the back-aperture of the objective, the SNR and the treatment of the focal volume. This chapter emphasizes that the FCS data fitting procedures are as important as that of any other experimental parameter. These considerations extend further into data processing and analysis with a better approach than what is being used currently.

5.2 Preliminaries

The experimental data is conventionally fit using standard local search techniques e.g. the Marquardt Levenberg (ML) algorithm [80] or other gradient search techniques [81]. They are fast and typically accurate when the user has a good knowledge of the sample system at hand. A typical prerequisite for these categories of algorithms is the sound knowledge of the behavior of fit parameters and in most cases good initial guesses for accurate fitting, otherwise leading to fitting artifacts. Normally, for known fit models and with user experience about the behavior of fit parameters, these local search algorithms work extremely well. However, for heterogeneous systems or where automated data analysis is a prerequisite, there is generally a need to apply procedures that treat FCS data fitting as a black box and generates reliable fit parameters with accuracy for the chosen model in hand.

This novel computational approach to analyze FCS data is done by means of a

stochastic algorithm for global search called PGSL, an acronym for Probabilistic Global Search Lausanne [82]. This algorithm does not require any initial guesses and does the fitting in terms of searching for solutions by global sampling. The performance study of PGSL was carried out for Eq. 3.2. The statistical study and the goodness of fit criterion for PGSL was also presented. The scope of PGSL by a hybrid analysis wherein the output of PGSL is fed as initial guesses to ML. Reliability studies show that PGSL and the hybrid combination of both perform better than ML for various thresholds of the mean squared error (MSE). The following section presents the detailed simulations carried out for the noise analysis. This supplements the work done in [83].

5.3 Noise Analysis: Simulations

We further extend our study and present a detailed statistical analysis with respect to the various noise contributions as present in a typical FCS experiment. We exclude systematic experimental errors like alignment and aberration effects due to refractive index mismatches that also contribute to the measured signal to background [84]. Noise sources in the auto-correlation processes are mainly the following. Shot noise arising from the small lag times which is governed by the Poisson statistics of the number of photons per correlator bin time $\Delta\tau_n$. Averaging noise for the long lag times which is equivalent to the small number of slow events during the finite measurement interval, T; Correlation noise which is equivalent to the rounding off (quantization) errors in the numerical implementation here; Detector saturation that is equal to the maximum count rate due to the detector dead time; Fluorescence saturation that is equal to the maximum emission rate due to the fluorescence life time; afterpulsing, which corresponds to the correlated virtual photon events generated by the detector and finally background, which is the uncorrelated static photon events. We fix the detector saturation here to a constant value as it can be easily avoided in an experiment. Since we are mainly interested in modelling the influence of shot noise, we set the detector dead time and the background to zero to avoid any influence of the average detection rate on the auto-correlation. This implies that the variation of the detector quantum yield does not introduce any bias on the correlation curve. Thereby, we are able to check the robustness of our fitting algorithm against correlation noise and shot noise. The current Monte-Carlo simulation therefore takes into account all noise sources with the exception of afterpulsing here.

We further simulate the behavior of a solution of Rhodamine6G molecules when diffusing through the focus of a $488nm$ laser beam in a epi-illumination setup with a 40x 1.20 water immersion objective. The diameter of the pinhole was set to 50μm. Rhodamine6G is a bright and photo-stable fluorophore with well-known absorption and emission characteristics18. In the laser focus, the number of emitted photons is in the order of $10^8 s^{-1}$ per Rhodamine6G molecule. The number of photons passing through the pinhole is then in the order of $10^6 s^{-1}$. Depending upon the detector quantum yield, the number of detected photons is of the order of 10^5 per molecule per second.

We then simulate the absorption and emission process of fluorophores diffus-

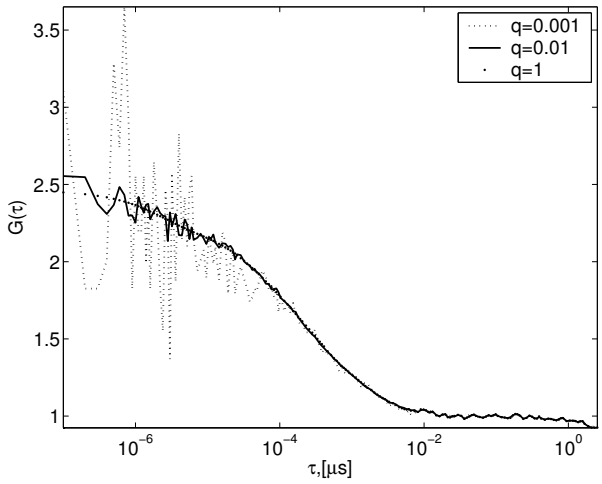

Figure 5.1: The effect of noise for various photon yields depending on the quantum yields (q) of the APD. qs of 0.01, 0.1 and 1 are considered here respectively.

ing through the confocal volume. The approach followed is similar to that of Wohland [22] and is concisely explained there. Firstly, the arrival times of fluorescence photons on the detector are calculated using a Monte-Carlo simulation. Secondly, the detector behavior is modelled by its dead time, quantum yield and dark current (noise) to get the trace of detected photons. Finally, this generated photon trace for every time-bin is evaluated by calculating the auto-correlation.

Here, we calculate the auto-correlation as for a multiple-tau correlator generally used in FCS experiments. Our software correlator calculates the symmetrically normalized auto-correlation [85, 86] for 16 lag times $\Delta\tau_0$ and 8 lag times of $\Delta\tau_n = 2^n\Delta\tau_0$ for each $n = (1,2,26)$. For the following noise analysis, we have therefore the arrival times of photons through the detection pinhole. For varying detector quantum yields (q), the auto-correlation is then calculated for the detected photons. Since, the photon detection part here is a random process leading to shot noise with Poisson statistics, each auto-correlation represents an individual realization of the detection process. The signal to noise ratio here is therefore represented as a function of the photon yield per particle and the quantum efficiency of the detector for a given constant experiment time. The various FCS curves for varying qs of 0.01, 0.1, and 1 for the detector are shown in Fig. 5.1.

5.3.1 Parameter estimation in presence of noise

The scatter plots in Fig. 5.2 shows the variance of these variables with respect to the quantum efficiency. They are generated from 100 realizations of individual correlograms for varying detection efficiencies from 0 to 1. We see good parameter retrieval beyond a q of 0.1 onwards.

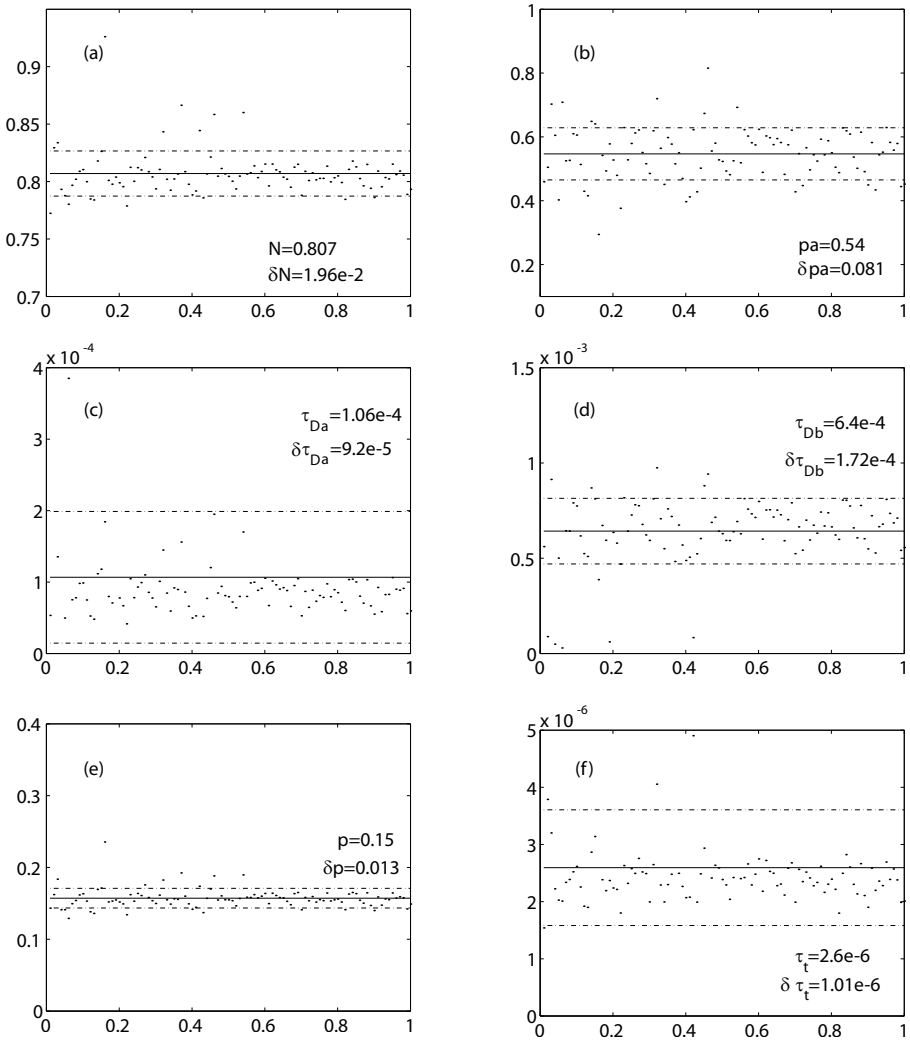

Figure 5.2: The scatter plots for N, pa, τ_{Da}, τ_{Db}, p and τ_t shows the overall variation with respect to the noise around the mean values.

5.4 Discussion

This chapter described a novel stochastic data analysis concept applicable to the determination of fitting parameters in FCS experiments. For the two-component case, the FCS parameters were determined with high precision by the application of this algorithm. The fitting values are given the lower and upper bounds with no initial guesses thereby giving the experimentalist the confidence in data validation when experiments are to be planned requiring the application of various models. It is therefore useful in experimental situations wherein accurate determination of parameters with no fitting artifacts from various physical models is also a prime criterion. The quality of the fit was also demonstrated from the mean error analysis. Statistical studies further demonstrate the capability of the method to estimate the fit parameters with greater confidence along with existing standard gradient-based methods. Therefore, PGSL appears to be a viable tool for unbiased parameter retrieval of FCS data.

Conclusions and Perspectives

The goal of using the SIL has been established as a working tool for FCS experiments. This simple and novel idea has been studied both experimentally and theoretically and integrated into a standard FCS set-up. The results were comparable to that of a conventional high NA FCS set-up. The advantages in terms of a better confined focal field and the resultant benefit of focussing several microns into solution via aberration compensation is also highlighted.

Given the inherent design advantage of an air-gap vis-à-vis the overall microscope and especially the objective when used with a conventional air-objective (typically 0.6NA or 0.8NA) it presents itself as a natural extension in terms of thermal decoupling. The opto-mechanical-thermal module for the SIL was designed and experiments conducted on vesicles which served as model systems for bio-chemical applications with the SIL thermal module. The module worked fine for the intended temperature range of $22 - 85^{\circ}C$.

The presented study on the SIL is but one part of the jigsaw puzzle of developing a total integrated analysis system as part of a high throughput SMD tool. The module developed and studied with the refractive hemispherical SIL would find its fulfillment with a configuration that would be possible with the advanced manufacturing techniques of the lithography industry culminating in a multi-diffractive SIL. This technological development is already in sight and presents itself as a commercially feasible route for the oligonucleotide based industry interested in hybridization analysis. It would then be possible to take a few μl of appropriately conjugated DNA and study it with appropriate temperature variations.

Apart from the above SIL oriented FCS projects, a fitting tool for FCS data analysis was developed based on a novel stochastic approach which eliminates the issue of giving good initial guesses as in local gradient search methods. This computationally faster algorithm was studied in depth for both synthetic and experimental data with noise analysis. It is intended to be used in automated data fitting environments where accurate expert user inputs in terms of good initial guesses is often difficult. With the inclusion of correct methods of calculation of standard deviation, the resolution and precision of parameter estimation in FCS can be improved within certain limits.

Current data processing in the "high throughput" zone is automated and utilizes extremely sophisticated tools all primarily based on a local search technique utilizing a good initial guess. With user experience and improved data processing it has been the current backbone for SMD analysis. The PGSL presents as itself a convenient alternative for the huge amounts of data waiting to be analyzed with increased reliability and better performance.

Abbreviations

2D - two-dimensional

3D - three-dimensional

Ar^+ - Argon-ion laser

CPM - Counts per Molecule

f - friction coefficient

F, F(t), $\delta F(t)$ - fluorescence intensity, fluorescence intensity fluctuations

FCS - fluorescence correlation spectroscopy

FWHM - full width half maximum

γ - correction factor for the ACF for an inhomogeneous excitation profile

$G(\tau)$- autocorrelation function

G_∞ - convergence value of autocorrelation function for long times

HeNe - laser Helium Neon laser

$I(\overrightarrow{r})$ - intensity distribution

IPSF - intensity point spread function

k_B - Boltzmann constant

N - number of particles

NA - numerical aperture

ω - shape parameter of intensity profile

PSF - point spread function

q_f fluorescence quantum yield

q_D - detector quantum yield

r, $\overrightarrow{r}$ - radial coordinate, or coordinate vector

SNR - signal-to-noise ratio

SMD - single molecule detection

τ - correlation time

τ_D - characteristic correlation or diffusion time

τ_{trip} - triplet lifetime

T - temperature

$T(\overrightarrow{r})$ - transmission function of a pinhole

V - volume

$W(\overrightarrow{r})$ - effective intensity profile

Acknowledgements

A thesis is a kind of micro-penance which cannot be completed without the help of many people.

First of all, I would like to thank my thesis advisor Prof. Theo Lasser for having given me the opportunity to work on this research project and for the freedom he gave me to realize my ideas. My deep gratitude and appreciation goes to the thesis defence committee for the time and effort they put in reading and judging the thesis and for their valuable comments. Many thanks to Prof. Rudolf Rigler, Prof. Jerker Widengren, Prof. Olivier Martin, Prof. Philippe Renaud and Prof. Rainer A. Leitgeb.

I was very fortunate to work in the pleasant and motivating scientific atmosphere of the Laboratoire d'Optique Biomédicale. Many thanks to my collaborators and group members with whom I spent many good moments inside and outside the lab.

My gratitude to Per Rigler for his immense patience, leadership, guidance and for following my work with keen interest. Many heartfelt thanks to Antonio Lopez for his positive and cheerful spirit and also aiding me in solving the nitty-gritty mechanical design problems. A special thanks to Rainer A. Leitgeb again for the good counsel. Could not have made it without all of you!

Markus Laubscher and Varvara Valtchanova for the delightful evenings, food, entertainment and trips in Europe. My appreciation for Europe has been a large extent been possible because of both of you.

Jelena Mitić, Kai Haßler, Marcel Leutenegger and Ling Chin Hwang for their cooperation and the intense scientific and non-scientific discussions at all points of time.

Rajesh Langoju and Abhijit Patil for being there always. Your unlimited enthusiasm and affection has been a pillar of support throughout my stay in Lausanne. Chandrasekhar Seelamantula for livening up our desi parties by reminding me that we both are in common cuckoo country!

Sathish Ramani, Nirmala Sathish, Koushik Venkatesan and Venkatesh Sivasubramaniam for their affection and moral support.

My heartfelt gratitude to the Shah family for being around and giving me the support that only a good Indian family can give. I owe them a debt for this lifetime. The Mittals deserve a special award for having successfully endured me for so long!

My special thanks to Anshuman, Ratika, Laxmi and Arthi for the many parties and treats with the IBM gang in Lausanne.

Boris Karamata and Stéphane Bourquin for sharing the office with me and for broadening my perspectives on Switzerland.

Luc Froehly and Sébastian Favre for their inspiring presence in the initial stages of my thesis. Alexandre Serov for the laboratory guidance and reading my drafts every time with such patience.

My heartfelt thanks to Thomas Sidler, Claude Amendola and Ronald Gianotti for their help and advice throughout the electronic and mechanical related challenges faced during the experiments.

The institute secretaries Judith Chaubert, Nathalie Etter, Manuelle Borruat and Yvette Bernhard for their availability and administrative help.

I would also like to thank to all my colleagues from the Institute of Applied Optics with whom I shared many interesting scientific meetings and outdoor activities.

Many thanks to all the people in Lausanne and Europe in general that have made my life so enjoyable during all these years. My acknowledgements goes also to my family and friends who have always encouraged me.

Finally, thanks to Switzerland for coming into my life!

G. Ramachandra Rao
Lausanne, December, 2006

Bibliography

[1] E. L. Elson and D. Magde. Fluorescence correlation spectroscopy .1. conceptual basis and theory. *Biopolymers*, 13(1):1–27, 1974.

[2] W. W. Webb. Applications of Fluorescence Correlation Spectroscopy. *Q. Rev. Biophys.*, 9(1):49–68, 1976.

[3] R. Rigler and E.S. Elson. *Fluorescence correlation spectroscopy :Theory and Applications*. Chemical Physics. Springer Verlag, Berlin, 2001.

[4] Y. Chen, J. D. Muller, P. T. C. So, and E. Gratton. The photon counting histogram in fluorescence fluctuation spectroscopy. *Biophys. J.*, 77(1):553–567, 1999.

[5] P. Kask, K. Palo, D. Ullmann, and K. Gall. Fluorescence-intensity distribution analysis and its application in biomolecular detection technology. *Proc. Natl. Acad. Sci. U. S. A.*, 96(24):13756–13761, 1999.

[6] K. Palo, U. Mets, S. Jager, P. Kask, and K. Gall. Fluorescence intensity multiple distributions analysis: Concurrent determination of diffusion times and molecular brightness. *Biophys. J.*, 79(6):2858–2866, 2000.

[7] J. Widengren, J. Dapprich, and R. Rigler. Fast interactions between Rh6G and dGTP in water studied by fluorescence correlation spectroscopy. *Chem. Phys.*, 216(3):417–426, 1997.

[8] J. Widengren, U. Mets, and R. Rigler. Photodynamic properties of green fluorescent proteins investigated by fluorescence correlation spectroscopy. *Chem. Phys.*, 250(2):171–186, 1999.

[9] U. Mets, J. Widengren, and R. Rigler. Application of the antibunching in dye fluorescence: Measuring the excitation rates in solution. *Chem. Phys.*, 218(1-2):191–198, 1997.

[10] C. Eggeling, J. Widengren, R. Rigler, and C. A. M. Seidel. Photobleaching of fluorescent dyes under conditions used for single-molecule detection: Evidence of two-step photolysis. *Anal. Chem.*, 70(13):2651–2659, 1998.

[11] D. Magde, W. W. Webb, and E. Elson. Thermodynamic fluctuations in a reacting system - measurement by fluorescence correlation spectroscopy. *Phys. Rev. Lett.*, 29(11):705–708, 1972.

[12] D. Magde, E. L. Elson, and W. W. Webb. Fluorescence correlation spectroscopy.2. experimental realization. *Biopolymers*, 13(1):29–61, 1974.

[13] Ehrenberg.M and R. Rigler. Rotational brownian-motion and fluorescence intensity fluctuations. *Chem. Phys.*, 4(3):390–401, 1974.

[14] M. Eigen and R. Rigler. Sorting single molecules - application to diagnostics and evolutionary biotechnology. *Proc. Natl. Acad. Sci. U. S. A.*, 91(13):5740–5747, 1994.

[15] T. D. Milster. Near-field optics: A new tool for data storage. *Proc. IEEE*, 88(9):1480–1490, 2000.

[16] M. Yoshita, T. Sasaki, M. Baba, and H. Akiyama. Application of solid immersion lens to high-spatial resolution photoluminescence imaging of GaAs quantum wells at low temperatures. *Appl. Phys. Lett.*, 73(5):635–637, 1998.

[17] K. Koyama, M. Yoshita, M. Baba, T. Suemoto, and H. Akiyama. High collection efficiency in fluorescence microscopy with a solid immersion lens. *Appl. Phys. Lett.*, 75(12):1667–1669, 1999.

[18] A. Serov, R. Rao, M. Gösch, T. Anhut, D. Martin, R. Brunner, R. Rigler, and T. Lasser. High light field confinement for fluorescent correlation spectroscopy using a solid immersion lens. *Biosens. Bioelectron.*, 20(3):431–435, 2004.

[19] P. Y. Bolinger, D. Stamou, and H. Vogel. Integrated nanoreactor systems: Triggering the release and mixing of compounds inside single vesicles. *J. Am. Chem. Soc.*, 126(28):8594–8595, 2004.

[20] A. Pramanik, P. Thyberg, and R. Rigler. Molecular interactions of peptide with phospholipid vesicle membranes as studied by fluorescence correlation spectroscopy. *Chem. Phys. Lipids*, 104(1):35–47, 2000.

[21] B. Raphael and I. F. C. Smith. A direct stochastic algorithm for global search. *Appl. Math. Comput.*, 146(2-3):729–758, 2003.

[22] T Wohland, R Rigler, and H Vogel. The standard deviation in fluorescence correlation spectroscopy. *Biophys. J.*, 80(6):2987–2999, 2001.

[23] S M Mansfield and G S Kino. Solid immersion microscope. *Appl. Phys. Lett.*, 57(24):2615, 1990.

[24] Q. Wu, G. D. Feke, R. D. Grober, and L. P. Ghislain. Realization of numerical aperture 2.0 using a gallium phosphide solid immersion lens. *Appl. Phys. Lett.*, 75(26):4064–4066, 1999.

[25] I. Ichimura, S. Hayashi, and G. S. Kino. High-density optical recording using a solid immersion lens. *Appl. Optics*, 36(19):4339–4348, 1997.

[26] L. P. Ghislain, V. B. Elings, K. B. Crozier, S. R. Manalis, S. C. Minne, K. Wilder, G. S. Kino, and C. F. Quate. Near-field photolithography with a solid immersion lens. *Appl. Phys. Lett.*, 74(4):501–503, 1999.

[27] K. Sendur, C. Peng, and W. Challener. Near-field radiation from a ridge waveguide transducer in the vicinity of a solid immersion lens. *Phys. Rev. Lett.*, 94(4), 2005.

[28] S. Moehl, H. Zhao, B. D. Don, S. Wachter, and H. Kalt. Solid immersion lens-enhanced nano-photoluminescence: Principle and applications. *J. Appl. Phys.*, 93(10):6265–6272, 2003.

[29] V. N. Mahajan. *Optical Imaging and Aberrations, Ray Geometrical Optics*, volume 1. Society of Photo-Optical Instrumentation Engineers (SPIE), 1998.

[30] R. Brunner, M. Burkhardt, A. Pesch, O. Sandfuchs, M. Ferstl, S. Hohng, and J. O. White. Diffraction-based solid immersion lens. *J. Opt. Soc. Am. A-Opt. Image Sci. Vis.*, 21(7):1186–1191, 2004.

[31] W.L. Barnes, G. Bjork, J M Gerard, P. Jonsson, J.A.E. Wasey, P.T. Worthing, and V. Zwiller. Solid-state single photon sources: light collection strategies. *Eur. Phys. J. D*, 18:197–210, 2002.

[32] M. Y. Liu, B. X. Xu, T. C. Chong, G. Q. Yuan, and C. Y. Bah. Aspherical supersphere solid immersion lens for near-field optical recording. *Jpn. J. Appl. Phys. Part 1 - Regul. Pap. Short Notes Rev. Pap.*, 39(2B):875–876, 2000.

[33] D. H. Chien, C. H. Tsai, S. S. Lo, C. C. Chen, and J. Y. Chang. Solid immersion lenses in planar waveguides. *J. Lightwave Technol.*, 23(9):2746–2748, 2005.

[34] Y. Zhang. Design of high-performance supersphere solid immersion lenses. *Appl. Opt.*, 45:4540–4546, 2006.

[35] D. A. Fletcher, K. B. Crozier, K. W. Guarini, S. C. Minne, G. S. Kino, C. F. Quate, and K. E. Goodson. Microfabricated silicon solid immersion lens. *J. Microelectromech. Syst.*, 10(3):450–459, 2001.

[36] T. D. Milster, J. S. Jo, and K. Hirota. Roles of propagating and evanescent waves in solid immersion lens systems. *Appl. Optics*, 38(23):5046–5057, 1999.

[37] W. H. Yeh and M. Mansuripur. Evanescent coupling in magneto-optical and phase-change disk systems based on the solid immersion lens. *Appl. Optics*, 39(2):302–315, 2000.

[38] B. D. Terris, H. J. Mamin, D Rugar, W.R. Studenmund, and Kino G.S. Near-field optical-data storage using a solid immersion lens. *Appl. Phys. Lett.*, 65(4):388–390, 1994.

[39] M. Yoshita, K. Koyama, Y. Hayamizu, M. Baba, and H. Akiyama. Improved high collection efficiency in fluorescence microscopy with a weierstrass-sphere solid immersion lens. *Jpn. J. Appl. Phys. Part 2 - Lett.*, 41(7B):L858–L860, 2002.

[40] T. D. Milster. Chromatic correction of high-performance solid immersion lens systems. *Jpn. J. Appl. Phys. Part 1 - Regul. Pap. Short Notes Rev. Pap.*, 38(3B):1777–1779, 1999.

[41] C. J. R. Sheppard and P. Török. Approximate forms for diffraction integrals in high numerical aperture focusing. *Optik*, 105(2):77–82, 1997.

[42] J Stamnes. *Waves in Focal Regions*. Adam Hilger, Bristol, 1986.

[43] P. Török and P. Varga. Electromagnetic diffraction of light focused through a stratified medium. *Appl. Optics*, 36(11):2305–2312, 1997.

[44] B. Richards and E. Wolf. Electromagnetic diffraction in optical systems .2. structure of the image field in an aplanatic system. *Proc.Roy.Soc.A*, 253(1274):358–379, 1959.

[45] R. Rigler, U. Mets, J. Widengren, and P. Kask. Fluorescence correlation spectroscopy with high count rate and low-background - analysis of translational diffusion. *Eur. Biophys. J. Biophys. Lett.*, 22(3):169–175, 1993.

[46] E. Wolf. Electromagnetic diffraction in optical systems .1. an integral representation of the image field. *Proc.Roy.Soc.A*, 253(1274):349–357, 1959.

[47] S. T. Hess and W. W. Webb. Focal volume optics and experimental artifacts in confocal fluorescence correlation spectroscopy. *Biophys. J.*, 83(4):2300–2317, 2002.

[48] M Gu. *Advanced Optical Imaging Theory*. Springer Verlag, 2000.

[49] P. Debye. The behaviour of light waves nearing combustion or a caustic line. *Ann. Phys.-Berlin*, 30(14):755–776, 1909.

[50] L. E. Helseth. Roles of polarization, phase, amplitude in solid immersion lens systems. *Opt. Commn*, 191:161–172, 2001.

[51] Y. Zhang. Multiple reflection effect inside a hemispherical solid immersion lens. *Opt. Commun.*, To be published, 2006.

[52] P. Török, P. Varga, and G. Nemeth. Analytical solution of the diffraction integrals and interpretation of wave-front distortion when light is focused through a planar interface between materials of mismatched refractive-indexes. *J. Opt. Soc. Am. A.*, 12(12):2660–2671, 1995.

[53] V. N. Mahajan. *Aberration Theory Made Simple*, volume TT06. Society of Photo-Optical Instrumentation Engineers (SPIE), 1993.

[54] S.W. Hell, G. Reiner, C. Cremer, and E. H. K. Stelzer. Aberrations in confocal fluorescence microscopy induced by mismatches in refractive-index. *J. Microsc.-Oxf.*, 169:391–405, 1993.

[55] A. Egner and S. W. Hell. Equivalence of the Huygens-Fresnel and Debye approach for the calculation of high aperture point-spread functions in the presence of refractive index mismatch. *J. Microsc.-Oxf.*, 193:244–249, 1999.

[56] Y. Zhang. Theoretical study of near-field optical storage with a solid immersion lens. *J. Opt. Soc. Am. A*, 23:2132–2136, 2006.

[57] T. M. Jeong, D. K. Ko, and J. M. Lee. Generalized ray-transfer matrix for an optical element having an arbitrary wavefront aberration. *Opt. Lett.*, 30(22):3009–3011, 2005.

[58] P. Kask, P. Piksarv, and U. Mets. Fluorescence correlation spectroscopy in the nanosecond time range - photon antibunching in dye fluorescence. *Eur. Biophys. J. Biophys. Lett.*, 12(3):163–166, 1985.

[59] P. Kask, P. Piksarv, U. Mets, M. Pooga, and E. Lippmaa. Fluorescence correlation spectroscopy in the nanosecond time range - rotational diffusion of bovine carbonic anhydrase-b. *Eur. Biophys. J. Biophys. Lett.*, 14(4):257–261, 1987.

[60] J. Widengren and P. Schwille. Characterization of photoinduced isomerization and back-isomerization of the cyanine dye Cy5 by fluorescence correlation spectroscopy. *J. Phys. Chem. A*, 104(27):6416–6428, 2000.

[61] N. L. Thompson. *Fluorescence Correlation Spectroscopy*, volume 1 of *Topics in Fluorescence Spectroscopy*. Plenum Press, New York, 1991.

[62] C. J. R. Sheppard and P. Török. An electromagnetic theory of imaging in fluorescence microscopy, and imaging in polarization fluorescence microscopy. *Bioimaging*, 5:205–218, 1997.

[63] P. Schwille, S. Kummer, A. A. Heikal, W. E. Moerner, and W. W. Webb. Fluorescence correlation spectroscopy reveals fast optical excitation-driven intramolecular dynamics of yellow fluorescent proteins. *Proc. Natl. Acad. Sci. U. S. A.*, 97(1):151–156, 2000.

[64] K. Korn, P. Gardellin, B. Liao, M. Amacker, A. Bergström, H. Björkman, A. Camacho, S. Dörhöfer, K. Dörre, J. Enström, T. Ericson, T. Favez, M. Gösch, A. Honegger, S. Jaccoud, M. Lapczyna, E. Litborn, P. Thyberg, H. Winter, and R. Rigler. Gene expression analysis using single molecule detection. *Nucleic Acids Res.*, 31(16), 2003.

[65] C. Schildkr and S. Lifson. Dependence of melting temperature of DNA on salt concentration. *Biopolymers*, 3(2):195, 1965.

[66] Z. J. Tan and S. J. Chen. Nucleic acid helix stability: Effects of salt concentration, cation valence and size, and chain length. *Biophys. J.*, 90(4):1175–1190, 2006.

[67] J. L. Mergny and L. Lacroix. Analysis of thermal melting curves. *Oligonucleotides*, 13(6):515–537, 2003.

[68] R. E. Cech. A high-low temperature microscope stage. *Rev. Sci. Instrum.*, 21(8):747–749, 1950.

[69] D. S. Reid. Programmed controlled temperature microscope stage. *J. Microsc.-Oxf.*, 114:241–248, 1978.

[70] L. Verbit and T. R. Halbert. Versatile variable temperature microscope stage. *J. Chem. Educ.*, 48(11):773, 1971.

[71] R. Rigler, A. Jost, and L. Demaeyer. Chemical kinetics at micro level - a laser micro temperature jump apparatus for relaxation studies in micro samples. *Exp. Cell Res.*, 62(1):197, 1970.

[72] N. Ernest Dorsey. Knovel critical tables., 2003.

[73] W. R. Ware. Oxygen quenching of fluorescence in solution - an experimental study of diffusion process. *J. Phys. Chem.*, 66(3):455–458, 1962.

[74] G. Laustriat and D. Gerard. Influence of dynamic quenching on thermal dependence of fluorescence in solution - study of indole and phenol in water and dioxane. *J. Phys. Chem.*, 82(6):746–749, 1978.

[75] B Valeur. *Molecular Fluorescence: Principles and Applications*. Wiley-VCH, Weinheim, 2001.

[76] J.R. Lakowicz. *Principles of fluorescence spectroscopy*. Plenum Press, New York, 1983.

[77] D. Stamou, C. Duschl, E. Delamarche, and H. Vogel. Self-assembled microarrays of attoliter molecular vessels. *Angew. Chem.-Int. Edit.*, 42(45):5580–5583, 2003.

[78] P. Rigler and W. Meier. Encapsulation of fluorescent molecules by functionalized polymeric nanocontainers: Investigation by confocal fluorescence imaging and fluorescence correlation spectroscopy. *J. Am. Chem. Soc.*, 128(1):367–373, 2006.

[79] M. Lang, T. D. Milster, T. Minamitani, G. Borek, and D. Brown. Fabrication and characterization of sub-100 μm diameter gallium phosphide solid immersion lens arrays. *Jpn. J. Appl. Phys. Part 1 - Regul. Pap. Short Notes Rev. Pap.*, 44(5B):3385–3387, 2005.

[80] D. W. Marquardt. An algorithm for least-squares estimation of nonlinear parameters. *J. Soc. Ind. App.Math.*, 11(2):431–441, 1963.

[81] R. Aster, B. Borchers, and C. Thurber. Parameter estimation and inverse problems. pages 184–204. Academic Press, 2004.

[82] B. Raphael and I. F. C. Smith. A direct stochastic algorithm for global search. *Appl. Math. Comput.*, 146(2-3):729–758, 2003.

[83] R. Rao, R. Langoju, M. Gösch, P. Rigler, A. Serov, and T. Lasser. Stochastic approach to data analysis in fluorescence correlation spectroscopy. *J. Phys. Chem. A*, 110(37):10674–10682, 2006.

[84] J. Enderlein, I. Gregor, D. Patra, and J. Fitter. Art and artefacts of fluorescence correlation spectroscopy. *Curr. Phar. Biotech.*, 5(2):155–161, 2004.

[85] K. Schatzel. Noise in photon-correlation and photon structure functions. *Optica Acta*, 30(2):155–166, 1983.

[86] K. Schatzel, M. Drewel, and S. Stimac. Photon-correlation measurements at large lag times - improving statistical accuracy. *J. Mod. Opt.*, 35(4):711–718, 1988.

Paper 1

Available online at www.sciencedirect.com
SCIENCE DIRECT®
Biosensors and Bioelectronics 20 (2004) 431–435
BIOSENSORS & BIOELECTRONICS
www.elsevier.com/locate/bios

High light field confinement for fluorescent correlation spectroscopy using a solid immersion lens

A. Serov [a,*], R. Rao [a], M. Gösch [a], T. Anhut [a], D. Martin [c], R. Brunner [c], R. Rigler [a,b], T. Lasser [a]

[a] *Institute for Biomedical Imaging, Optics, and Engineering of the Swiss Federal Institute of Technology (EPFL), CH-1015 Lausanne, Switzerland*
[b] *Department of Medical Biochemistry and Biophysics, Karolinska Institute, S-171 77 Stockholm, Sweden*
[c] *Carl Zeiss Jena GmbH, Germany*

Received 24 September 2003; received in revised form 4 February 2004; accepted 5 February 2004
Available online 14 May 2004

Abstract

In this paper we present recent single molecule detection experiment using a solid immersion lens (SIL) for fluorescent correlation spectroscopy measurements. We compared the performance of the SIL in combination with an air objective (40×, numerical aperture (NA) = 0.6) with a water immersion objective (40×, NA = 1.15) in a confocal microscope system (ConfoCorr 1). Important parameters for single molecule experiments such as collection efficiency and excitation field confinement were investigated. Although the two set-ups have similar numerical aperture the measurements demonstrated higher field confinement and better collection efficiency for the SIL system in comparison to the conventional confocal set-up. Adding spherical aberrations shifts the sample volume up to 4 μm away from the plane surface of the SIL and conserves a diffraction limited focal volume. In this case the FCS autocorrelation demonstrates a free 3D diffusion of dye molecules in a highly confined light field.

Keywords: Fluorescent correlation spectroscopy; Solid immersion lens; Single molecule detection; High resolution

1. Introduction

Recent advances in high spatial resolution imaging (Mansfield and Kino, 1990), as well as fluorescence imaging (Koyama et al., 1999), Raman imaging (Poweleit et al., 1998) and near-field optical data storage (Terris et al., 1994) have proved the usefulness of solid immersion lenses (SILs) for variety of applications. Here we demonstrate that the SIL-approach has a potential towards single molecule detection experiment, particularly for fluorescence correlation spectroscopy.

Fluorescence correlation spectroscopy (FCS) is an experimental technique used in studies of chemical and photophysical dynamics at the single molecule level (Rigler and Elson, 2001). Here, an autocorrelation is obtained by measuring the random intensity fluctuations of a fluorescent response generated by light-excited molecules in a confocal volume (Rigler et al., 1993). Analysis of the correlation function reveals information about the dynamic (transversal and rotational diffusion) and kinetic processes (e.g. triplet states) of the fluorescent molecules. Over the last decade, FCS has emerged as a powerful method for analyzing the processes on the molecular level: molecular interactions, conformational changes, chemical reactions, protein binding on cell membranes, photophysical dynamics, etc.

For a high signal-to-noise ratio, both the confinement of the excitation optical field and a high collection efficiency of the optical system are of a major importance in FCS experiments. Both parameters are directly proportional to the numerical aperture (NA) of the microscope objective system. Filling the object space with a liquid of a high refractive index material, e.g. oil, increases the NA. Another way to increase the NA can be achieved by utilizing a SIL. The SIL is an aplanatic lens, which increases the NA of the optical

* Corresponding author.
E-mail address: alexandre.serov@epfl.ch (A. Serov).

0956-5663/$ – see front matter © 2004 Elsevier B.V. All rights reserved.
doi:10.1016/j.bios.2004.02.028

system by a factor of n (for a hemispherical SIL) (Terris et al., 1994); where n is the index of refraction of the SIL material. Koyama et al. (1999) reported an improvement of the collection efficiency by using a hemispherical SIL for fluorescence microscopy. Wu et al. (1999) achieved a spatial resolution as small as 139 nm at a wavelength of 560 nm. Excitation field confinement and the resolution are closely related parameters in single molecule experiments. Moreover, solid immersion microscopy (SIM) can be made even more powerful when combined with confocal microscopy technique. Recently a successful use of SIL for confocal microscopy was reported (Karrai et al., 2000). All this makes the SIL a useful component for single molecule spectroscopy.

For our study we integrated a hemispherical SIL into a commercial confocal microscope system, ConfoCorr 1 from Carl Zeiss, originally built-up for FCS experiments. We investigated the performance of our SIL-FCS set-up and compared it to the performance of a conventional FCS system.

2. Theory

The basics of FCS have been established around 25 years, detailed reviews on FCS can be found elsewhere (Rigler and Elson, 2001; Krichevsky and Bonnet, 2002). In general, an excitation laser is focused into a sample. Every molecule diffusing through the excitation focus gives rise to fluorescence photon bursts. The length of each photon burst corresponds to the time the molecule spends in the detection volume element. In order to reject out of focus contributions and stray light a confocal set-up is used thereby increasing the signal to background (Rigler et al., 1993). Thereafter the fluorescence photons are detected with a single photon detector working in the Geiger-mode. Every detected single fluorescence photon generates a pulse, which is sent to a correlator where the autocorrelation function of the fluorescence intensity fluctuations is calculated.

The autocorrelation curve contains information about the dynamics of intensity fluctuations in the time interval from typically 30 ns (the dead time of the detector) to the duration of the measurement. By fitting the autocorrelation function to an analytical expression important basic parameters can be extracted: diffusion time (average time a molecule is located in the detection volume) average number of molecules, in the detection volume element, molecule fractions (if several types of different diffusing molecules are present in the sample), and the fraction of particles occupying the triplet state (long-living non-fluorescent dark states). The correlation function in FCS can be expressed as

$$G(\tau) = \frac{\langle I(t+\tau)\, I(t)\rangle}{\langle I(t)\rangle^2} = G_{\text{motion}}(\tau)\, X_{\text{kinetics}}(\tau), \tag{1}$$

where $I(t)$ is the instantaneous intensity of the fluorescence present in the detection volume element, $\langle\,\rangle$ denotes the time average. $G_{\text{motion}}(\tau)$ reflects the motion of the molecules, e.g. translational and rotational diffusion, and $X_{\text{kinetics}}(\tau)$ describes kinetic processes of the molecule/s. For the case of free 3D diffusion of a single chemical species in a dilute solution the analytical expression of the autocorrelation function is (Krichevsky and Bonnet, 2002)

$$G(\tau) = 1 + \frac{1}{N}\left(1+\frac{\tau}{\tau_{\text{D}}}\right)^{-1}\left(1+\frac{\tau}{\omega^2\tau_{\text{D}}}\right)^{-1/2} \times \left(1+\frac{T}{1-T}\exp\left(-\frac{\tau}{\tau_{\text{T}}}\right)\right), \tag{2}$$

which is deduced based on 3D Gaussian spatial distribution of the detected fluorescence intensity. Here N is the average number of molecules present in the detection volume element $V = \pi^{3/2}\omega_{xy}^2\omega_z$, $\omega = \omega_z/\omega_{xy}$ is the aspect ratio of the detection volume element, and $\tau_{\text{D}} = \omega_{xy}^2/4D$ denotes the diffusion time across the sampling region, where D is the diffusion coefficient. Thus, the average concentration of the molecules in the volume element is $C = N/V$.

In the kinetic part, the last term in Eq. (2), T is the fraction of dye molecules in the triplet state and τ_{T} is the relaxation time, the time while the molecules are in the triplet state.

3. Experiment

Our experimental set-up was based on the commercial confocal microscope designed for FCS measurements, ConfoCorr 1 from Carl Zeiss. Dye molecules crossing the sampling volume, were excited with an Ar^+ laser at 488 nm. Intensity variations of the fluorescent response were detected with a single photon counting module and processed with a hardware correlator. The obtained data were stored in the computer memory and then analyzed with a software based non-linear Marquardt–Levenberg algorithm that allows extracting the number of molecules, N, the diffusion time, τ_{D}, of the molecules, the fraction of molecules in the triplet state, T, and the relaxation time, τ_{T}; see Eq. (2). Two different microscope objectives were used for the measurements. For conventional FCS measurements, considered as reference measurements, we used a 40× NA = 1.15 water immersion objective (Olympus, Uapo/340, variable cover slip correction). For the SIL-FCS set-up a Zeiss objective (LD Achroplan, 40×, NA = 0.60, variable cover slip correction) with a working distance of 1.8 mm was used. This objective has sufficient working distance to place the SIL (LaSF35 glass, $r = 0.7$ mm, $n = 2.030$ at $\lambda = 527$ nm (expected fluorescence maximum of "molecular probes"); $n = 2.034944$ at $\lambda = 488$ nm) in-between. A variable cover slide correction ring is integrated in the 0.6NA objective; the adjustment gauge allows a correction between a 'negative' "−0.125 mm" correction until a "2 mm" cover slip thickness. The choice of the adjustment gauge position allows to manipulate the wavefront curvature of the incident field and consequently the intensity distribution in the focal plane

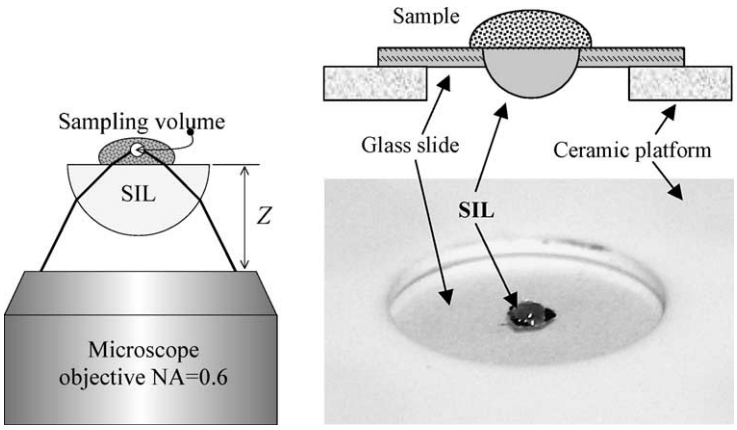

Fig. 1. SIL-objective system (left) and the SIL mounted into the holder (right).

(Helseth, 2001), including the SIL in our case. With the SIL in place and the correction ring set to "0 mm" (SIL/0) the sampling volume is situated on the plane surface of the SIL (Milster et al., 1999). When the correction ring is set to the "−0.125 mm" (SIL/−0.125) position the sampling volume is shifted several microns away from the plane SIL surface conserving the diffraction-limited performance (simulated with ZEMAX (Focus Software, Inc.)).

Rhodamine Green at 10 nM concentration was used as a fluorescent sample. The dye molecules were dispersed in a droplet on a cover glass, for the water immersion objective, or directly on the flat surface of the SIL; see Fig. 1. Optical power on the sample was around 3 mW in all measurements tuned so to achieve the same value of the fraction of molecules in the triplet state, T.

To obtain the best focus, and therefore the higher excitation field confinement, we measured correlation curves for different distances between the SIL flat surface and the objective (Z), see Fig. 1, and for different pinhole sizes (PH) of the detector, see Fig. 2. The obtained correlation curves were fitted to Eq. (2) for an investigation of the dependencies of N, τ_D and CPM (counts per molecule) on Z and PH-diameter for two different adjustments of the correction ring ("0" and "−0.125"). Fig. 2 shows the results for the SIL/−0.125 system (The results obtained for the SIL/0 system are not shown here due to their qualitative similarity to the SIL/−0.125 system). With the obtained data such as the CPM value, which represents the collection efficiency of the system; N, which is related to the sampling volume $V = N/C$ (C is the concentration of the dye molecules); and τ_D, which is related to the transversal diameter of the confined field $\omega_{xy} = 2\sqrt{\tau_D D}$ (D is the diffusion constant) the system performance was analyzed. We define both the best focus position providing a highest field confinement and optimal pinhole size when CPM value reaches a maximum.

As we can see from Fig. 2, the SIL/−0.125 system has a highest field confinement when the distance between the SIL flat surface and the microscope objective is $Z_{best} = 1782\ \mu m$. Higher confinement of the field leads to a smaller sampling volume (see the minimum in Fig. 2, top) and better excitation/collection efficiency, which is expressed here in terms of counts per molecule value (see the maximum in Fig. 2, bottom). Here we define the best focus position when CPM value reaches a maximum in the Z dependency. These

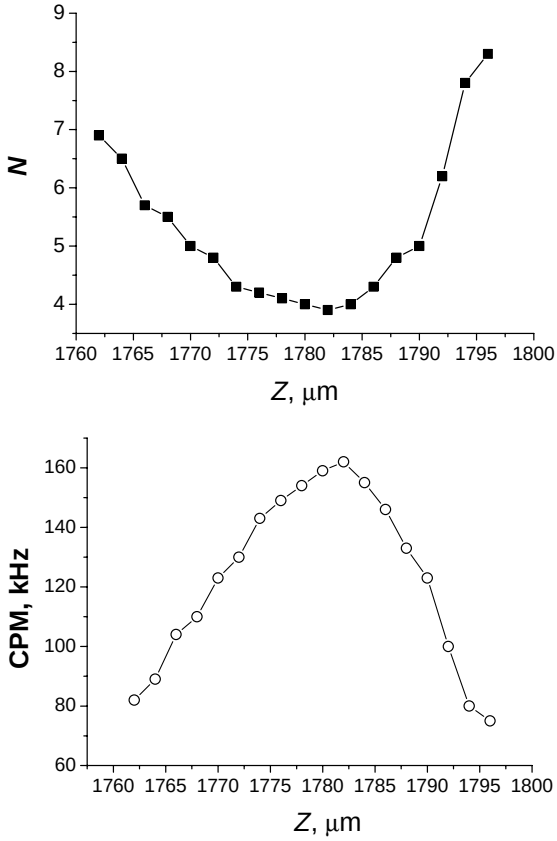

Fig. 2. Results obtained with SIL-FCS system. Left—dependence of the number of molecules (N) in the sampling volume on the distance between the SIL flat surface and the 0.6NA microscope objective (Z); right—detection efficiency of the SIL system in terms of counts per molecule (CPM) as a function of the distance between the SIL flat surface and the 0.6NA microscope objective (Z).

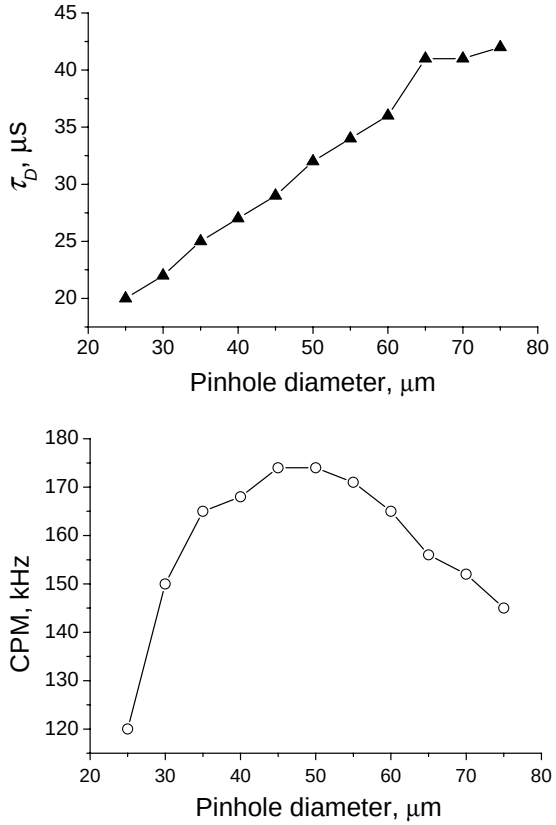

Fig. 3. Results obtained with SIL-FCS system. Left—dependence of the diffusion time (τ_D) on the detector pinhole diameter; right—detection efficiency of the SIL system in terms of counts per molecule (CPM) as a function of the detector pinhole diameter.

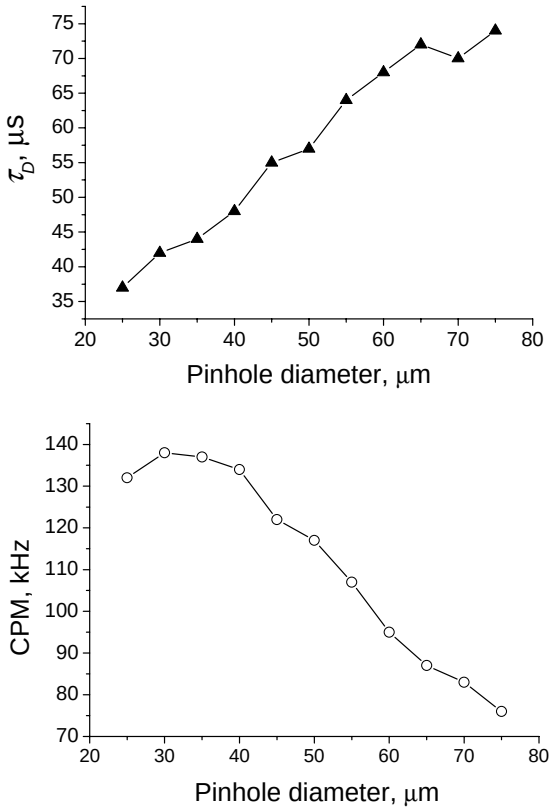

Fig. 4. Results obtained with 1.15NA objective system. Left—dependence of the diffusion time (τ_D) on the detector pinhole diameter; right—detection efficiency of the SIL system in terms of counts per molecule (CPM) as a function of the detector pinhole diameter.

data are obtained with a 45 μm diameter pinhole, which was found to be an optimum, see Fig. 3.

Dependence of the diffusion time τ_D on the detector pinhole size is shown in Fig. 3 (top) measured at Z_{best} = 1782 μm. This dependence has a linear behavior that is in a good agreement to the theory. On the bottom graph of Fig. 3 the collection efficiency of the SIL system is shown for the different detector pinhole sizes. As known the pinhole in confocal set-up plays role of a special filter: if it is too small—some of the photons coming from the focal spot will be lost; if it is to big—the background noise will influence the signal. This tendency is seen in Fig. 3 (bottom). The maximum in the CPM value here implies an optimal pinhole size adjustment for the SIL system. To compare our SIL measurements to the conventional FCS set-up we also optimized the pinhole size for the 1.15NA objective system. The results are shown in Fig. 4.

The optimal pinhole size for 1.15NA objective system is approximately 1.5 times smaller than for the SIL system since, from the one hand, the magnification of the SIL microscope system is two times higher due to the refractive index of the SIL (n_{SIL} = 2.030) but, from the other hand, the SIL system has about 1.5 times smaller focal spot on the sample (found from $\omega_{xy} = 2\sqrt{\tau_D D}$). This leads to that the focal spot size in the detector plane is approximately 1.5 times bigger for the SIL system. The maximum CPM value for the SIL system is slightly higher than for the 1.15NA objective system. This allows us to conclude that the SIL system collection efficiency is comparable or even better that for the conventional system.

We found that for the SIL/−0.125 systems the highest CPM value as well as the lowest N corresponds to a shift of the focal volume of 3.7 μm away from the plane SIL surface. This distance excludes any evanescent field excitation to the fluorescence response. Even for the SIL/0 system the focal volume was shifted 1.6 μm away from the plane SIL surface probably due to residual chromatic aberrations. The focus shifts were calculated based on ray-tracing and the experimentally determined Z values.

Typical correlation curves obtained with SIL/0, SIL/−0.125, and 1.15NA systems are shown in Fig. 5. We see that SIL/0 and SIL/−0.125 systems have equal performance, while the reference set-up with the 1.15NA objective reveals an approximately two times bigger sampling volume (N_{SIL} = 4.4, $N_{1.15NA}$ = 9.3). The transversal diameter ω_{xy} of the 1.15NA sampling volume is also bigger by a factor of 1.5. However the CPM values obtained with all the systems are not much different. Also, the fraction of the molecules in the triplet state was equal for all measurements implying

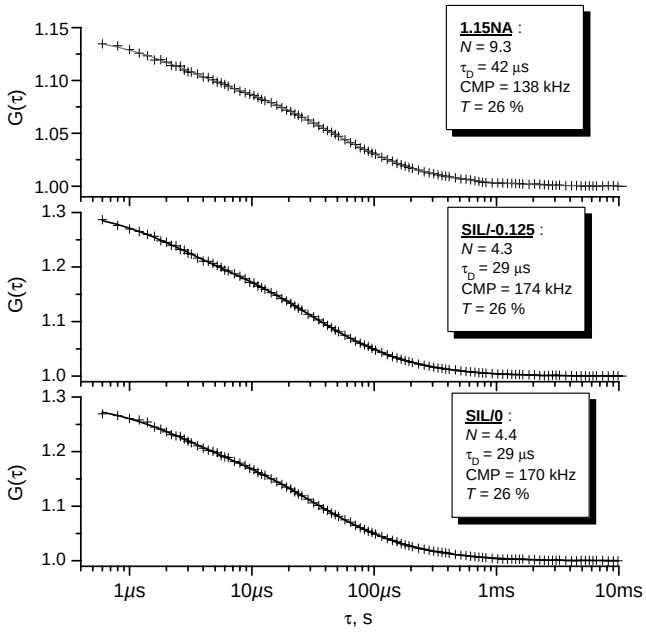

Fig. 5. Typical FCS correlation curves of Rhodamine Green at 10 nM concentrations obtained with: 1.15NA objective; SIL and 0.6NA objective with "−0.125 mm"-setting; SIL and 0.6NA objective with "0 mm"-setting. The "crosses" are the measured data; the solid line represents the fit with Eq. (2).

the same intensity level in the sampling volumes. Since the pinhole sizes of both systems were optimized corresponding to the highest CPM value, see Figs. 3 and 4, we consider that the sampling volume matches the confined volume size.

1.15NA objective is a diffraction-limited system. The measurements performed with the SIL allows us to conclude that the SIL based system achieves a performance comparable or even slightly better than it is obtained with a conventional diffraction-limited high numerical aperture objective. The diffraction-limited SIL performance can probably be explained by the influence of the polarization, phase and amplitude distribution in the incident beam on the SIL focusing system (Helseth, 2001).

4. Conclusion

In summary, we have investigated the usefulness of a hemispherical SIL for FCS measurements. For this purpose a conventional air-objective has been combined with a SIL. This combination demonstrated a two-times smaller confined volume compared to the 1.15NA water immersion objective. We demonstrated that adding a spherical aberration to the incident field shifts the sample volume away from the plane surface of the SIL (up to 4 μm in our case) conserving the diffraction-limited performance with a high collection efficiency.

Many biological samples have to be measured in a temperature-controlled manner, which can become difficult as long as the instrument is in touch with the probe and works as a heat sink. In this context we suggest that a SIL-air objective combination could be utilized in order to achieve a thermal decoupling of the sample from the instrument.

As further work we plan to investigate electromagnetic field distribution of the SIL configuration and its influence on the FCS signal.

References

Mansfield, S.M., Kino, G.S., 1990. Solid Immersion Microscope. Appl. Phys. Lett. 57 (24), 2615–2616.

Koyama, K., Yoshita, M., Baba, M., Suemoto, T., Akiyama, H., 1999. High collection efficiency in fluorescence microscopy with a Solid Immersion Lens. Appl. Phys. Lett. 75 (12), 1667–1669.

Poweleit, C.D., Gunther, A., Goodnick, S., Menéndez, J., 1998. Raman imaging of patterned silicon using a solid immersion lens. Appl. Phys. Lett. 73 (16), 2275–2277.

Terris, B.D., Mamin, H.J., Rugar, D., Studenmund, W.R., Kino, G.S., 1994. Near-field optical data storage using a solid immersion lens. Appl. Phys. Lett. 65 (4), 388–390.

Rigler, R., Elson, E.S., 2001. Fluorescence Correlation Spectroscopy: Theory and Applications, Chemical Physics. Springer-Verlag, Berlin.

Rigler, R., Mets, U., Widengren, J., Kask, P., 1993. Fluorescence correlation spectroscopy with high count rates and low background: analysis of translational diffusion. Eur. Biophys. J. 22, 169–175.

Krichevsky, O., Bonnet, G., 2002. Fluorescence correlation spectroscopy: the technique and its applications. Rep. Prog. Phys. 65, 251–297.

Wu, Q., Feke, G.D., Grober, R.D., 1999. Realization of a numerical apperture 2.0 using a gallium phosphide solid immersion lens. Appl. Phys. Lett. 75 (26), 4064–4066.

Karrai, K., Lorenz, X., Novotny, L., 2000. Enhanced reflectivity contrast in confocal solid immersion lens microscopy. Appl. Phys. Lett. 77 (21), 3459–3461.

Helseth, L.E., 2001. Roles of polarization, phase and amplitude in solid immersion lens system. Opt. Comm. 191, 161–172.

Milster, T.D., Joshua, S.Jo., Hirota, K., 1999. Roles of propagating and evanesvent waves in solid immersion lens systems. Appl. Opt. 38 (23), 5046–5057.

Paper 2

Total internal reflection fluorescence correlation spectroscopy (TIR-FCS) with low background and high count-rate per molecule

Kai Hassler[1], **Marcel Leutenegger**[1], **Per Rigler**[2], **Ramachandra Rao**[1], **Rudolf Rigler**[1], **Michael Gösch**[1] **and Theo Lasser**[1]

[1]*Ecole Polytechnique Fédérale de Lausanne (EPFL), Laboratoire d'Optique Biomédicale, 1015 Lausanne, Switzerland*

theo.lasser@epfl.ch

[2]*Universität Basel, Physikalische Chemie, 4056 Basel, Switzerland*

Abstract: We designed a fluorescence correlation spectroscopy (FCS) system for measurements on surfaces. The system consists of an objective-type total internal reflection fluorescence (TIRF) microscopy setup, adapted to measure FCS. Here, the fluorescence exciting evanescent wave is generated by epi-illumination through the periphery of a high NA oil-immersion objective. The main advantages with respect to conventional FCS systems are an improvement in terms of counts per molecule (cpm) and a high signal to background ratio. This is demonstrated by investigating diffusion as well as binding and release of single molecules on a glass surface. Furthermore, the size and shape of the molecule detection efficiency (MDE) function was calculated, using a wave-vectorial approach and taking into account the influence of the dielectric interface on the emission properties of fluorophores.

OCIS codes: (300.2530) Fluorescence, laser induced; (170.6280) Spectroscopy, fluorescence and luminescence; (240.6490) Spectroscopy, surface

References and links

1. D. Magde, W. W. Webb, and E. Elson, "Thermodynamic Fluctuations in a Reacting System - Measurement by Fluorescence Correlation Spectroscopy," Phys. Rev. Lett. **29**, 705–& (1972).
2. R. Rigler and E. L. Elson, *Fluorescence Correlation Spectroscopy: Theory and Applications* (Springer, Berlin, 2001).
3. O. Krichevsky and G. Bonnet, "Fluorescence correlation spectroscopy: the technique and its applications," Rep. Progr. Phys. **65**, 251–297 (2002).
4. R. Rigler, U. Mets, J. Widengren, and P. Kask, "Fluorescence Correlation Spectroscopy with High Count Rate and Low-Background - Analysis of Translational Diffusion," Eur. Biophys. J. Biophys. Lett. **22**, 169–175 (1993).
5. R. Brock and T. M. Jovin, "Fluorescence correlation microscopy (FCM) - Fluorescence correlation spectroscopy (FCS) taken into the cell," Cell. Mol. Biol. **44**, 847–856 (1998).
6. M. Auer, K. J. Moore, F. J. Meyer-Almes, R. Guenther, A. J. Pope, and K. A. Stoeckli, "Fluorescence correlation spectroscopy: lead discovery by miniaturized HTS," Drug Discov. Today **3**, 457–465 (1998).
7. A. M. Lieto, R. C. Cush, and N. L. Thompson, "Ligand-receptor kinetics measured by total internal reflection with fluorescence correlation spectroscopy," Biophys. J. **85**, 3294–3302 (2003).
8. U. Kettling, A. Koltermann, P. Schwille, and M. Eigen, "Real-time enzyme kinetics monitored by dual-color fluorescence cross-correlation spectroscopy," Proc. Natl. Acad. Sci. USA **95**, 1416–1420 (1998).

9. L. Edman, Z. Foldes-Papp, S. Wennmalm, and R. Rigler, "The fluctuating enzyme: a single molecule approach," Chem. Phys. **247**, 11–22 (1999).
10. N. L. Thompson, T. P. Burghardt, and D. Axelrod, "Measuring Surface Dynamics of Biomolecules by Total Internal- Reflection Fluorescence with Photobleaching Recovery or Correlation Spectroscopy," Biophys. J. **33**, 435–454 (1981).
11. K. Hassler, T. Anhut, R. Rigler, M. Gösch, and T. Lasser, "High count rates with total internal reflection fluorescence correlation spectroscopy," Biophys. J. **88**, L1–L3 (2005).
12. D. Axelrod, E. H. Hellen, and R. M. Fulbright, "Total Internal Reflection Fluorescence," in *Topics in Fluorescence Spectroscopy: Biochemical Applications*, J. R. Lakowicz, ed., vol. 3 (Plenum Press, 1992).
13. D. Axelrod, "Total internal reflection fluorescence microscopy in cell biology," Traffic **2**, 764–774 (2001).
14. D. Toomre and D. J. Manstein, "Lighting up the cell surface with evanescent wave microscopy," Tr. Cell Biol. **11**, 298–303 (2001).
15. R. L. Hansen, J. M. Harris, "Total Internal Reflection Fluorescence Correlation Spectroscopy for Counting Molecules at Solid/Liquid Interfaces," Anal. Chem. **70**, 2565–2575 (1998).
16. W. Lukosz, "Light-Emission by Magnetic and Electric Dipoles Close to a Plane Dielectric Interface .3. Radiation-Patterns of Dipoles with Arbitrary Orientation," J. Opt. Soc. Am. **69**, 1495–1503 (1979).
17. J. Enderlein, "Fluorescence detection of single molecules near a solution/glass interface - an electrodynamic analysis," Chem. Phys. Lett. **308**, 263–266 (1999).
18. N. L. Thompson, "Fluorescence Correlation Spectroscopy," in *Topics in Fluorescence Spectroscopy*, J. R. Lakowicz, ed., vol. 1 (Plenum Press, New York, 1991).
19. B. Richards and E. Wolf, "Electromagnetic Diffraction in Optical Systems .2. Structure of the Image Field in an Aplanatic System," Proc. Roy. Soc. A **253**, 358–379 (1959).
20. J. Mertz, "Radiative absorption, fluorescence, and scattering of a classical dipole near a lossless interface: a unified description," J. Opt. Soc. Am. B-Opt. Phys. **17**, 1906–1913 (2000).
21. S. Weiss, "Fluorescence Spectroscopy of Single Biomolecules," Science **283**, 1676–1683 (1999).
22. K. Hassler, M. Leutenegger, M. Gösch, T. Lasser, Laboratoire d'Optique Biomédicale, Ecole Polytechnique Fédérale de Lausanne (EPFL), 1015 Lausanne, Switzerland are preparing a manuscript to be called "Mathematical Models for Total Internal Reflection Fluorescence Correlation Spectroscopy".
23. C. T. Culbertson, S. C. Jacobson, and J. M. Ramsey, "Diffusion coefficient measurements in microfluidic devices," Talanta **56**, 365–373 (2002).

1. Introduction

An increasing number of research fields in biology and medicine requires spectroscopic techniques with single molecule sensitivity in order to understand biochemical or microbiological processes. One of the technological milestones for spectroscopy was therefore the development of the confocal principle, which subsequently resulted in a very high signal to noise ratio in many applications. The implementation of the confocal principle, known from microscopy, in fluorescence correlation spectroscopy (FCS) [1, 2, 3] in the early 90's, was a technical innovation that dramatically enhanced the sensitivity of FCS [4]. From this moment on, FCS was used in an ever increasing number of applications to investigate dynamic and kinetic properties of molecular systems including measurements of diffusion inside cells [5], investigations of receptor - ligand binding kinetics [6, 7] and enzyme binding and reaction kinetics [8, 9]. The latter applications generally require the molecular system under investigation to be attached to a surface. In this case, the use of total internal reflection FCS (TIR-FCS) [10] can be advantageous over confocal FCS. In contrast to confocal FCS where fluorophores are excited inside the waist of a laser beam, TIR-FCS uses an evanescent wave to excite molecules. This leads to a reduced axial extent of the observation volume and hence to a decreased background from Raman scattered light and from unwanted fluorescence of molecules in solution. However, both techniques, when used for measurements on surfaces, have disadvantages. For instance, confocal FCS suffers from a large axial extent of the excitation- and hence observation volume, while for classical TIR-FCS, the light collection efficiency is comparably low. To circumvent these inadequacies we propose a new technique that combines several aspects of TIR-FCS and confocal FCS [11]. Based on an objective-type TIRF setup [12, 13, 14], the proposed system uses epi-illumination through the periphery of a high NA oil-immersion objective to generate an evanescent wave on the surface of a microscope slide. The fluorescence signal is collected

by the same objective, which leads to an excellent light collection efficiency while retaining the advantage of a reduced detection volume. In the present paper, we demonstrate the high performance of 'objective-type TIR-FCS' by investigating diffusion and binding of free dye molecules on surfaces, respectively. Our results show that the proposed technique has superior performance compared to classical FCS methods with respect to the signal to background ratio and counts per molecule (cpm). The parameter cpm is a frequently used figure of merit in FCS, which denotes the detection rate of photons, emitted by a single fluorophore inside the observation volume. Furthermore, the molecule detection efficiency (MDE) function and the size of the observation volume was calculated using high-angle vectorial diffraction integrals. The calculations incorporate the influence of the dielectric interface on the emission properties of fluorophores. Parameters derived from experimental data, in particular the structure parameter and diffusion times, agree with the calculated MDEs.

2. Instrumentation

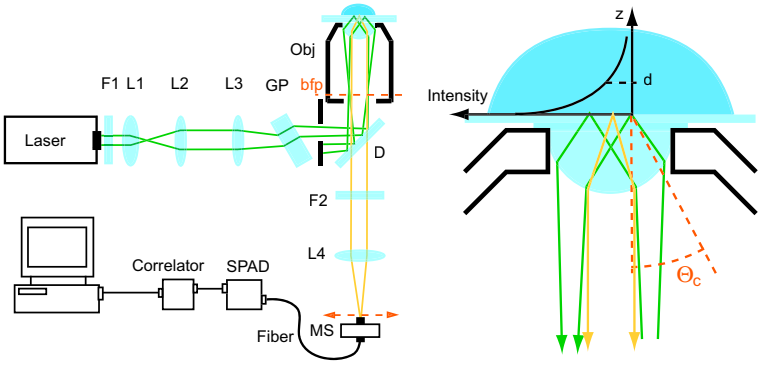

Fig. 1. Schematic representation of the 'objective-type TIR-FCS' setup (left). L1 - L4: lenses; F1, F2: fluorescence filters; GP: glass plate; D: dichroic mirror; Obj: microscope objective; bfp: back focal plane of the objective; MS: motorized scanning stage. An enlargement of the ray-path inside the microscope objective (right). d: evanescent wave depth; Θ_c: critical angle.

The setup (Fig. 1) is essentially an objective-type ('prismless') total internal reflection fluorescence (TIRF) setup adapted to measure FCS. Here, the beam of an argon ion laser (model 2214-25ML, Cyonics, Sunnyvale, CA) is enlarged by means of a telescope formed by lenses L1 and L2. Lens L3 focuses the beam onto the back focal plane (BFP) of an oil-immersion objective (α-Plan-Fluar, 1.45 NA, 100×, Carl Zeiss Jena GmbH, Jena, Germany) in order to get a collimated beam emerging from the objective. A pivotable glass-plate GP enables lateral shifting of the laser beam with respect to the optical axis. By shifting the beam, the angle of incidence at the glass-sample interface can be adjusted to exceed the critical angle Θ_c, thereby introducing total internal reflection. In this way, an evanescent wave with an intensity distribution that is Gaussian in the xy plane (parallel to the interface) and exponential in the z direction (along the optical axis) is generated at the glass-sample interface. The intersection of the beam with the interface is elliptical, with a lateral dimension (full width at half maximum of the intensity distribution in the plane of incidence) of roughly 15 μm. Fluorescence light is collected by the same objective and focused onto the end of a fiber, which is connected to a single photon avalanche diode (SPAD) (SPCM-AQR-13-FDC, PerkinElmer, Wellesley, MA). The core of the fiber acts as a pinhole assuring the lateral confinement of the observation volume. In our measurements we used a fiber with a core diameter of 50 μm, unless otherwise stated, which

was a convenient choice for the experimental investigations. The signal of the SPAD is processed by a hardware correlator or a single photon counting module (SPCM, SPC-630, Becker & Hickl GmbH, Berlin, Germany) to record the intensity versus time trace with high time resolution.

The illuminated region at the glass-water interface is several times larger than the observation volume, whose lateral extent is delimited by a pinhole in the microscope's image plane. The actual size of the illuminated region is adjustable by changing the magnification of the telescope used to enlarge the beam. Because of the large illuminated region, TIRF imaging using a camera and spectroscopic measurements can be performed at the same time. For spectroscopic measurements, locating a position of interest in the sample, e.g. a single receptor attached to the glass surface, may be achieved by scanning the fiber end in the image plane. There is no need to move the sample in this case, which makes the system very stable under experimental conditions. However, for some applications, where the residence time of fluorophores on the surface is large, illuminating a whole area may be disadvantageous due to the risk of photo-bleaching.

The advantages of the objective-type configuration with respect to prism-based configurations are, in particular, a higher light collection efficiency and easier handling of the system. In conventional (prism-based) TIR-FCS [10, 15], the evanescent wave is generated by means of a prism, placed on top of an objective that resides, in general, in an inverted microscope. A microscope slide is interfaced to the lower surface of the prism using immersion oil. The biological system (e.g. a membrane containing receptors) is attached to the lower surface of this glass slide, where fluorescence is excited by the evanescent wave. The sample, containing the biological system and some type of aqueous solution is sandwiched between the glass slide and another microscope-, or coverslide. An objective (typically a water immersion objective), placed below the coverslide is used to collect fluorescence light. The objective therefore focuses into an aqueous solution.

For objective-type TIR-FCS, the coverslide carrying the biological system is situated directly upon the objective and focusing into an aqueous solution is avoided. Only in such a case does the use of high NA oil immersion objectives become senseful because these objectives are designed to collect light in a high refractive index environment. They perform poorly, due to aberrations, if the focal plane is not right at the surface of the coverglass [3]. Using an oil immersion objective with NA 1.45 in the proposed configuration guarantees that almost all of the light from fluorescent particles at the focus position, emitted into the lower half-space falls into the cone of light accepted by the objective. The portion of light that is accepted even exceeds 50% because the light emission for dipoles near a dielectric interface is anisotropic, favoring emission into the medium with the higher refractive index [16, 17]. A further advantage of the present system is easier sample access. In particular, there is no hindrance by a prism as is the case in prism-based TIRF or TIR-FCS instruments [14].

3. Observation volume

In order to determine the shape and estimate the size of the detection volume, we calculated the normalized molecule detection efficiency (MDE) function [18], based on a wave-vectorial approach [19]. The MDE expresses the relative intensity seen by the detector as a function of the position of a point-emitter in the sample space; it is therefore the correct mathematical representation of the detection volume.

Figure 2 shows the normalized MDEs for a confocal FCS system (left) and for our TIR-FCS system (right). The MDE is calculated by multiplying the intensity distribution, $I(\mathbf{r})$, by the collection efficiency function (CEF), the CEF being proportional to the probability for a photon to be detected as a function of the position of the emitter:

$$\mathrm{MDE}(\mathbf{r}) = c\,\mathrm{CEF}(\mathbf{r})I(\mathbf{r}). \tag{1}$$

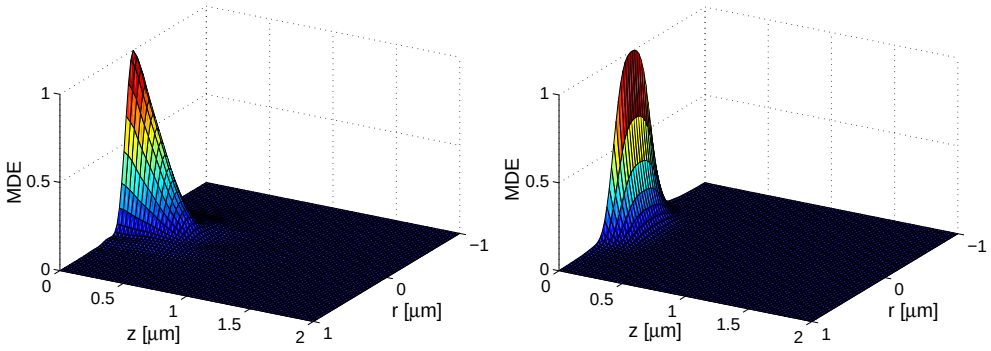

Fig. 2. The normalized MDEs for confocal FCS (left) and TIR-FCS (right). The confocal FCS case was calculated for a 1.15 NA, 40 $\times$ water-immersion objective. For the TIR-FCS case a 1.45 NA, 100 $\times$ oil-immersion objective was considered. A diameter of the pinhole (core of the fiber) of 50 μm was assumed in both cases. The excitation wavelength was 488 nm and the fluorescence emission wavelength was 542 nm.

The constant c is a normalization coefficient introduced to make $\mathrm{MDE}(0) = 1$. The fiber core diameter in both cases was $50\,\mu m$ and the excitation wavelength was 488 nm, corresponding to the blue line of the argon laser. The fluorophore under consideration was fluorescein. We assumed an emission wavelength of 542 nm, which is the average of the emission spectrum of fluorescein multiplied by the transmission function of the emission filter. In the confocal FCS case, we calculated the MDE for a 1.15 NA, 40$\times$ water immersion objective, which is standard. For confocal FCS, the intensity distribution was approximated by the point-spread function (PSF) of the system. The intensity distribution for TIR-FCS was assumed to be constant in the xy plane on the length scale of the typical diameter of the observation volume. It was further assumed to decay exponentially in the z direction with a penetration depth, d, of the intensity distribution given by:

$$d = \frac{\lambda}{4\pi}\left(n_2^2 \sin^2(\theta) - n_1^2\right)^{-1/2}. \tag{2}$$

This was calculated for a maximal lateral displacement of the excitation beam, implying a minimal angle of incidence $\theta = 71^\circ$. Here, n_1 and n_2 are the refractive indices of water and of the glass slide, respectively. The angle of incidence at the glass-water interface, θ, was measured by out-coupling the beam with the aid of a prism.

In the proximity of a dielectric interface the emission of a dipole with random orientation becomes highly anisotropic. This results in an apparent increase of the fluorophores brightness with decreasing distance to the interface [16, 17]. To take this effect into account we introduce the function $\mathrm{P}(z)$, the fraction of power emitted by a single dipole at a distance z from the interface into the cone of light accepted by the objective. This is calculated for a dipole with random orientation situated at the optical axis according to [20]. The CEF may then be approximated by

$$\mathrm{CEF}(\mathbf{r}) = \mathrm{P}(z) \int_S \mathrm{circ}(\mathbf{q}'/a)\mathrm{PSF}(\mathbf{q}-\mathbf{q}', z)\mathrm{d}\mathbf{q}'. \tag{3}$$

This is a convolution of the systems point spread function, $\mathrm{PSF}(\mathbf{r})$, calculated according to [19], with the transmission function of the pinhole represented by a disk function, $\mathrm{circ}(\mathbf{q}/a)$, and multiplied by $\mathrm{P}(z)$. The convolution is carried out in the focal plane in object space ($z = 0$). The symbol $\mathbf{q}$ denotes a vector in the focal plane and a is the pinhole size divided by the

magnification of the microscope. Results in Fig. 2 are consistent with experimental results, which we discuss later in section 5.

Given the MDE, we numerically calculated the W_1 volume and the effective volume, $V_{eff} \equiv W_1^2/W_2$, using [18]

$$W_n \equiv \int_V \mathrm{MDE}^n(\mathbf{r})\mathrm{d}\mathbf{r}, \tag{4}$$

where V is the half-space containing the sample. The quantity W_1 is the size of the geometrical volume that would produce the given count-rate if the detection efficiency were equal to the maximum of the MDE and constant inside the volume. The numerical calculations give $W_1 =$ 17 al (17 attoliter), $V_{eff} = 57$ al for TIR-FCS and $W_1 = 26$ al, $V_{eff} = 134$ al for confocal FCS.

The numerically calculated MDE for TIR-FCS is close to the analytical approximation given by

$$\mathrm{MDE_a}(x,y,z) = \exp\left(-2\frac{(x^2+y^2)}{\omega_{xy}^2}\right)\exp\left(-\frac{z}{h}\right). \tag{5}$$

The calculations of the autocorrelation function in section 5 are based on this approximation. Here, h is the axial displacement at which the normalized MDE decreases to $1/e$. This is smaller than the evanescent field depth, since the MDE, being the product of two in z monotonically decreasing functions (I and CEF), decreases faster with z than the intensity I.

4. Single molecule binding

Several groups were able to show the single fluorophore detection capabilities of objective-type TIRF (see [21] and references therein). We would expect that the proposed TIR-FCS setup features similar sensitivity since it differs from an objective-type TIRF setup essentially in the way the detected signal is processed and in the fact that for FCS only a single-point detector is used. Using our TIR-FCS setup, we performed measurements on single rhodamine 6G molecules undergoing adsorption and desorption on glass coverslides. Thereby we were able to examine the performance of our system; in particular, from high resolution intensity time traces we could estimate a lower bound for the maximal cpm that can be achieved in objective-type TIR-FCS experiments on binding kinetics. Dye molecules, present at a low concentration, diffused through the sample and eventually adsorbed at some location at the surface. For dyes entering the observation volume, and especially for binding events inside the observation volume, intensity peaks or bursts were observed. In general, the height of a burst depends on the lateral location of the bound dye within the observation volume or, for a diffusing dye, on its trajectory. It further depends on the dyes residence time inside the observation volume in the case that this is shorter than the binning time. Therefore, the cpm inferred from single molecule bursts are in general lower than the maximal cpm. For example, the maximal cpm would be obtained in experiments investigating binding kinetics of a single receptor, perfect alignment presumed; in other words, if the receptor is situated at the position where the MDE is maximal.

For these measurements, we have chosen experimental conditions described in the following. We used standard microscope coverslides previously cleaned by sonication in 2 % Helmanex. The applied laser power incident on the microscope slide was approximately 10 - 15 mW. We used a dye solution containing 1 nM rhodamine 6G in buffer (potassium phosphate, pH 7.0), a concentration, low enough to assure that only single molecule events are observed. Due to adsorption, this concentration of free dye drops to smaller values immediately after applying the solution to the coverslide. Using a conventional confocal FCS system (Confocor I, Zeiss Jena GmbH), we checked the sample to exclude further that bursts are due to aggregated molecules. No aggregation could be inferred from the FCS data.

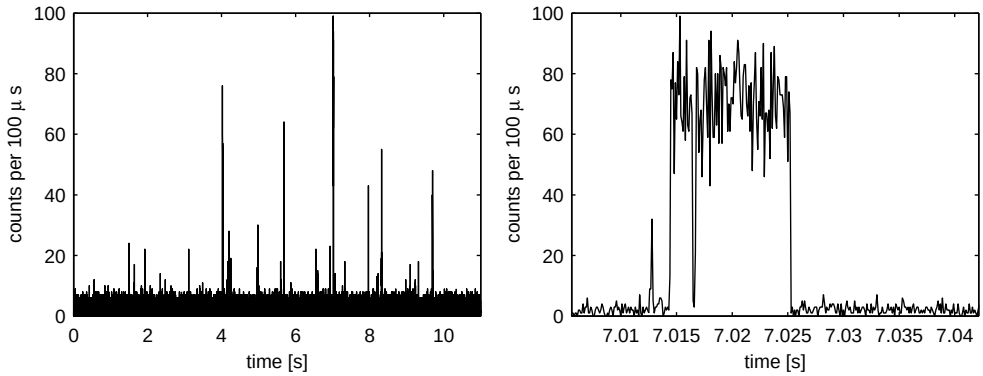

Fig. 3. Typical time trace for single rhodamine 6G molecules binding to a microscope slide (left). The right picture shows an enlargement of the two highest bursts. The binning time is 100 μs.

Figure 3 shows a typical time trace (left) and an enlargement of the highest photon bursts (right). The threshold for identifying a burst was set to 10 counts per 100 μs (given a background of 2 counts per 100 μs), in order to keep the probability for false positives (bursts due to variations of the background) low. Given this threshold, one can expect about one false positive in a time window of ten seconds. Intensity peaks, lasting on average for about 400 μs, occurred with a frequency of about 7 per second. The average number of overlaps of two or more bursts in a time interval of 10 s was calculated to be approximately one, for about 70 bursts in total. The probability to observe two molecules residing at the same time in the observation volume was therefore small. For broader bursts the binning time (100 μs) was small compared to the lasting of the bursts (sometimes several milliseconds). Bursts due to two (or more) molecules could in this case be easily distinguished from single molecule events by the necessary existence of steps or spikes. This is because a timely overlap of two binding events will never be exact; two molecules will not adsorb to, and desorb from the surface at exactly the same time, presumed that there is no aggregation (see above). In the example shown, inspection of the enlargement confirms the assumption that the observed event was caused either by a single molecule, or two, but successively binding molecules. In particular no spikes or steps are observed during the photon bursts lasting for about 10 ms. In general, burst heights frequently exceeded 70 counts, which implies cpm of more than 700 kHz. The background was approximately 20 kHz, which implies a signal to background ratio of 35 for the highest burst shown in Fig. 3. These values are further supported by FCS measurements of diffusing dyes as is shown in the following section.

5. FCS on diffusing molecules

We performed TIR-FCS measurements on rhodamine 6G molecules freely diffusing near a coverglass surface. To prevent unspecific binding, the microscope slides were treated with oxygen plasma before use. This renders the surface of the slides highly hydrophilic and lowers the probability to observe binding events. As a result, the correlation time becomes orders of magnitude smaller compared to measurements on slides not specially prepared. Furthermore, after cleaning with oxygen plasma no bursts are observed in the time traces, given a binning time of 100 ms and a fluorophore concentration, C, of 1 nM.

Figure 4 shows an autocorrelation curve and the corresponding time trace obtained for a solution of 100 nM rhodamine 6G in water. To fit the data, we used the model presented in [11]

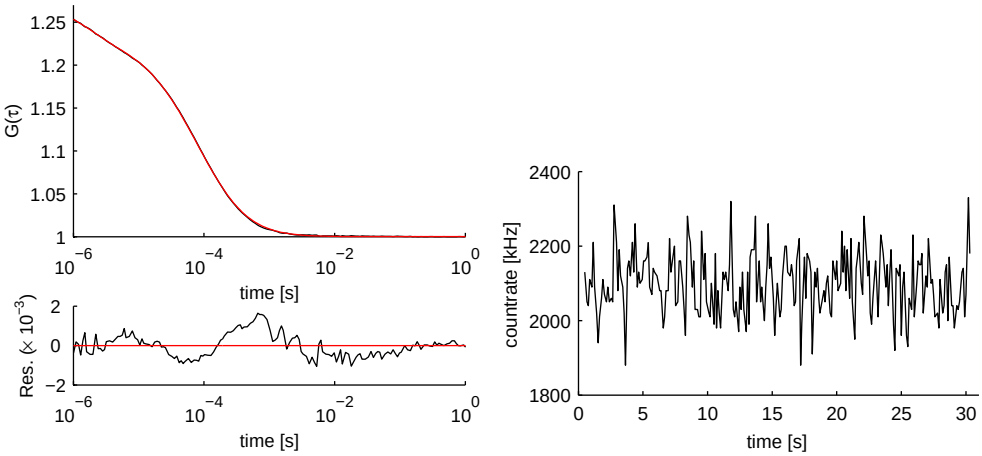

Fig. 4. Autocorrelation for diffusing rhodamine 6G molecules (upper left) and time trace (right). The overall measurement time was 30 s. Fitting the data with the model represented by equation 6 yields the following parameters: N = 1.2, $\tau_z = 21.1\,\mu$s, $\omega = 0.38$, $p = 15.4\,\%$, $\tau_t = 1.6\,\mu$s and cpm = 1.77 MHz. The red curve represents the fi t to the autocorrelation data.

and further discussed in [22]:

$$G(\tau) = 1 + \frac{\gamma}{N}\left[1 + \frac{p}{1-p}\exp\left(-\frac{\tau}{\tau_t}\right)\right]\left(1 + \frac{\tau}{\omega^2\tau_z}\right)^{-1} \times \left[\left(1 - \frac{\tau}{2\tau_z}\right) w\left(i\sqrt{\frac{\tau}{4\tau_z}}\right) + \sqrt{\frac{\tau}{\pi\tau_z}}\right]. \tag{6}$$

The diffusion times are $\tau_z = h^2/(4D)$ and $\tau_{xy} = \omega_{xy}^2/(4D) = \omega^2\tau_z$ for the axial diffusion and diffusion parallel to the surface, D is the diffusion coefficient, and $\omega = \omega_{xy}/h$. The parameters h and ω_{xy} describe the geometry of the observation volume (equation 5). The parameter p denotes the percentage of molecules in the triplet state and τ_t denotes the triplet state decay time. The function w is defined by $w \equiv \exp(-x^2)\mathrm{erfc}(-ix)$, and γ is a correction factor defined as $\gamma \equiv W_2/W_1$ [18]. This factor describes the deviation of the effective volume, $V_{eff} \propto 1/(CG(0))$, from W_1. From equations 4 and 5 it follows that γ equals $1/4$. However, in the subsequent calculations we used the value $\gamma = 1/3.4$, which was obtained from the numerical calculations.

To estimate the cpm from diffusion measurements, we used cpm $= r/N$ where r stands for the total average count-rate. N is the number of molecules in the volume W_1, which implies the cpm is the maximal value for a molecule that stays at the position where the MDE is maximal. This deviates from the definition in [11], where cpm describes an averaged value. The value for cpm in the example shown in Fig. 4 reaches almost 1.8 MHz. This is higher than the value obtained from the more direct investigation of the time traces (Fig. 3). The discrepancy may be due to a different alignment, especially of the focus position with respect to the sample and/or a different incident angle of the laser beam. Indeed, the background in these diffusion measurements was higher too; we estimated it to be approximately 45 kHz for FCS measurements in distilled water. This implies a signal to background ratio of about 39, which is close to the value obtained from direct measurements, which is 35.

From inspection of the residuals (Fig. 5, lower left), we conclude that the model still deviates from reality. This may be due to the fact, that there is some interaction of the dye with the surface even after treating the slides with oxygen plasma. In the present model, interaction of

dyes with the surface is not taken into account. Nevertheless, fitting of the data with the model represented by equation 6 gives reasonable parameter estimates.

In order to experimentally verify the model given by equation 6, TIR-FCS measurements for three different core diameters (37.5 μm, 50 μm and 100 μm) were performed on diffusing fluorescein. A solution of 50 nM fluorescein in buffer (TRIS, pH 8) was used for these experiments. The results for three typical measurements over 100 s measurement time are shown in Table 1.

Table 1. Parameter estimates for measurements with different pinhole diameters. *pd*: diameter of the pinhole. *D*: diffusion coefficient. ω_t: theoretically obtained structure parameter. For other symbols refer to the discussion of equation 6. The parameter τ_t was fixed to 1 μs.

$pd\,[\mu\mathrm{m}]$	N	$\tau_z\,[\mu\mathrm{s}]$	$\tau_{xy}\,[\mu\mathrm{s}]$	ω_t	ω	$p\,[\%]$	$\tau_t\,[\mu\mathrm{s}]$	$D\,[10^{-6}\mathrm{cm}^2\mathrm{s}^{-1}]$
37.5	5.3	3.7	75.5	0.20	0.22	38	1	2.8
50	5.4	3.4	97.7	0.17	0.19	27	1	3.0
100	17.3	4.3	255.2	0.10	0.12	33	1	2.4

The diffusion coefficients in Table 1 were calculated from the estimated value of τ_z, using the relation $D = h^2/4\tau_z$. The value of h was estimated from the numerical calculations of the MDE to be 64 nm. Values for the structure parameter, ω, that were derived from the data, are in excellent agreement with values ω_t, that were obtained from the numerically calculated MDEs. Also values for D coincide to a satisfactory degree with values previously published [23]. For a pinhole diameter of 100 μm, the MDE function is not well approximated by equation 5, which explains the deviations of the values τ_z and D in this case. However, these values are all in the same range, which is to be expected, because changing the pinhole diameter should only marginally change the axial extent of the MDE.

6. Conclusion

By adapting an objective-type TIRF setup for FCS measurements, a very sensitive system is obtained. High counts per molecule (cpm) are achieved due to the good light collection efficiency inherent to this system. A small observation volume decreases background and measurement artifacts. The signal to background ratio is excellent, as can be inferred from intensity time traces of single molecules adsorbing to a glass slide, or more indirectly from TIR-FCS measurements. Numerical calculations of the observation volume are in good agreement with experimental TIR-FCS data, obtained for freely diffusing fluorophores. In particular, the diffusion coefficient and structure parameters derived from experimental data are in good agreement with reported and theoretical values. The system allows for simultaneous parallel TIRF imaging by simply connecting a camera to a second port of the microscope. All these features, in addition easy handling and excellent stability, make the proposed set-up perfectly suitable for surface FCS measurements on a single molecule level.

Acknowledgment

We thank Mona Wells for careful reading of the manuscript and helpful discussions. This research was supported by the Swiss National Science Foundation (SNSF).

Paper 3

Stochastic Approach to Data Analysis in Fluorescence Correlation Spectroscopy

Ramachandra Rao,*,† Rajesh Langoju,‡ Michael Gösch,† Per Rigler,§ Alexandre Serov,† and Theo Lasser†

Laboratoire d'optique biomédicale, Laboratoire d'imagerie biomédicale, Ecole Polytechnique Fédérale de Lausanne (EPFL), 1015 Lausanne, Switzerland, and Physikalische Chemie, Universität Basel, 4056 Basel, Switzerland

Received: October 10, 2005; In Final Form: July 19, 2006

Fluorescence correlation spectroscopy (FCS) has emerged as a powerful technique for measuring low concentrations of fluorescent molecules and their diffusion constants. In FCS, the experimental data is conventionally fit using standard local search techniques, for example, the Marquardt−Levenberg (ML) algorithm. A prerequisite for these categories of algorithms is the sound knowledge of the behavior of fit parameters and in most cases good initial guesses for accurate fitting, otherwise leading to fitting artifacts. For known fit models and with user experience about the behavior of fit parameters, these local search algorithms work extremely well. However, for heterogeneous systems or where automated data analysis is a prerequisite, there is a need to apply a procedure, which treats FCS data fitting as a black box and generates reliable fit parameters with accuracy for the chosen model in hand. We present a computational approach to analyze FCS data by means of a stochastic algorithm for global search called PGSL, an acronym for Probabilistic Global Search Lausanne. This algorithm does not require any initial guesses and does the fitting in terms of searching for solutions by global sampling. It is flexible as well as computationally faster at the same time for multiparameter evaluations. We present the performance study of PGSL for two-component with triplet fits. The statistical study and the goodness of fit criterion for PGSL are also presented. The robustness of PGSL on noisy experimental data for parameter estimation is also verified. We further extend the scope of PGSL by a hybrid analysis wherein the output of PGSL is fed as initial guesses to ML. Reliability studies show that PGSL and the hybrid combination of both perform better than ML for various thresholds of the mean-squared error (MSE).

I. Introduction

Fluorescence correlation spectroscopy (FCS) has become an important tool for investigating the dynamic properties of single molecules in solution.[1−3] It was introduced in the 1970s as a method for measuring molecular diffusion, reaction kinetics, and flow of fluorescent particles.[4−7]

FCS is based on the statistical analysis of fluorescence intensity fluctuations in solution. It has found widespread applications in the study of various processes such as diffusion in solutions and membranes,[8] rotational diffusion,[9] and singlet−triplet state kinetics.[10] Recent research has proved the power of FCS as a diagnostic tool in biochemical studies.[11]

The data in FCS is conventionally modeled with a finite number of diffusing components and fit with a nonlinear minimization algorithm like the Marquardt−Levenberg method.[12] However, it can generate wrong results for bad initial guesses or for large number of components. It identifies a region of good solutions and follows a downward path (gradient) by accepting only better solutions. In multidimensional solution spaces, it is likely to identify only local minima. Since FCS data are by themselves inherently sensitive to changes in experimental setups,[13] the fitting algorithms have to be robust and accurate in their behavior to avoid unnecessary interpretations in data analysis.[14] Even if the data can be adequately fit by a small number of diffusing components with minimum residual error, this may lead to an unphysical description of the real system under study.

To overcome these drawbacks, we present a data-fitting algorithm for FCS based on a global search method called Probabilistic Global Search Lausanne (PGSL). The algorithm uses random sampling with a probability density function to locate the global minimum of a user-defined objective function. Starting with a uniform probability density function over the entire search space (set of all possible solution points), probabilities are updated dynamically such that a more intensive search is performed in regions where good solutions are found. The PGSL algorithm has a distinct advantage over other local search algorithms such as Marquardt−Levenberg, conjugate gradient, Newton−Raphson technique, and so forth, in so far as these require a good initial guess to reach the global minimum. Tests carried out on complex nonlinear objective functions such as the Lennard-Jones cluster optimization problem, indicate that PGSL performs better in terms of obtaining the success rate and the mean values of the variables estimated as compared with other probabilistic methods such as genetic algorithm and simulated annealing.[15] Because of its proven robustness in identifying the global optima, PGSL has been successfully applied to various areas such as structural mechanics[16] and phase-shifting interferometry.[17] In our implementation in the context of FCS, PGSL finds optimal solutions for FCS data. Subsequently, we address the mean-squared error (MSE) of the fit using the PGSL algorithm.

* To whom correspondence should be addressed. E-mail: ramachandra.rao@epfl.ch.
† Laboratoire d'optique biomédicale.
‡ Laboratoire d'imagerie biomédicale.
§ Universität Basel.

10.1021/jp055763t CCC: $30.25
Published on Web 08/25/2006 PAGE EST: 8.2

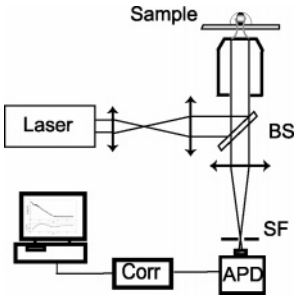

Figure 1. Schematic illustration of a typical high-NA objective-based epi-illumination FCS setup. (BS, dichroic beam splitter; SF, spatial filter (pinhole); APD, avalanche photodiode). Emitted fluorescence is detected by an APD and then processed by a multiple tau correlator (Corr).

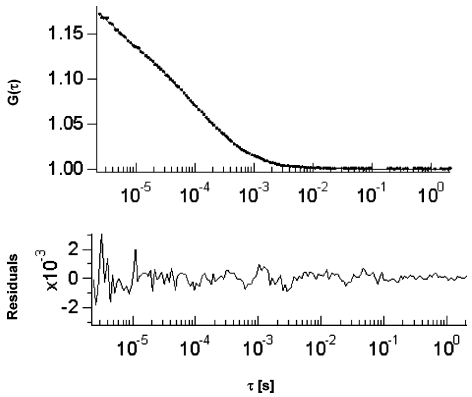

Figure 2. FCS curve of an M13 primer labeled with RhG at 10 nM concentration indicating the presence of two components. The dark lines show the fitted curve to our experimental data (dotted lines). The residuals shown indicate the fit quality. The two-component fit yielded the following parameters: $N = 7.2$, pa $= 0.34$, $\tau_{Da} = 35.20$ μs, $\tau_{Db} = 201.4$ μs, $\omega = 5$, $p = 0.31$, and $\tau_T = 2.02$ μs.

In what follows, we first present in section II a general framework by presenting the Experimental Methods and the FCS parameters of a two-component model with triplet transitions along with the tests carried out on them. Section III presents the PGSL algorithm, explains the approach in determining the global minimum for the physical model, the salient features of the classical ML algorithm, and a graphical overview of the internal architectures of PGSL and ML. Section IV presents two case studies wherein the PGSL is applied first to a standard two-component system and second to a parameter estimation with an essential noise contribution. Section V presents a benchmark test of PGSL with ML and presents a reliability test performed on PGSL, ML, and on a hybrid concept merging the PGSL with the ML algorithm.

II. Experimental Methods, Parameters in FCS Data, and Description of Tests

i. Experimental Methods. A FCS configuration is based on a standard confocal setup (Figure 1), the excitation laser light is directed by a dichroic mirror into a high-NA objective, which focuses the light into the sample. The fluorescence emission is collected through the same objective (epi-illumination), filtered by a dichroic beam splitter (BS), and focused onto a pinhole, so that the excited fluorescence light inside the sample is imaged onto the pinhole aperture acting as a spatial filter (SF), which efficiently confines the sampling volume to a diffraction limited size. After the pinhole, the fluorescence signal is collected directly by an avalanche photodiode (APD) and processed by a multiple tau correlator. Our experimental setup was based on the ConfoCor from Carl Zeiss which is basically a confocal microscope designed for FCS. The epi-illumination setup was done using a 40×/1.15 Olympus, Uapo/340 (cover slide corrected), water immersion objective. As a model two-component system, we take a mixture where there is a presence of two fractions, that is, free dye and a labeled primer sample, M13 primer, labeled with rhodamine green at 10 nM concentration for the two-component fits.

These dye molecules crossing the detection volume were excited with an Ar^+ laser at 488 nm. Intensity variations of the fluorescent response were detected across a pinhole of diameter 50 μm with a single photon counting module and processed with a hardware correlator. Optical power on the sample was around 50 μW for all measurements during a measurement time of 30 s. A measurement obtained along with its corresponding fit using PGSL is seen in Figure 2 for a representation of the two-component case.

ii. Parameters in FCS Data. The autocorrelation $G(\tau)$ of the solute molecules in a small open volume of a dilute solution is defined as

$$G(\tau) = \frac{\langle I(t+\tau)I(t)\rangle}{\langle I(t)\rangle^2} \tag{1}$$

where $\langle\ \rangle$ denotes the time average and $I(t)$ is the instantaneous intensity of the fluorescence present in the detection volume element. A thorough analysis leading to an analytical expression for a two-component case with multiple numbers of differently weighted freely and independently moving molecules is given by[18]

$$G(\tau) = 1 + \frac{1}{N}\left(\frac{1+p}{1-p}\right)\exp\left(\frac{-\tau}{\tau_t}\right) \times \left[\left(\frac{\mathrm{pa}}{1+\frac{\tau}{\tau_{Da}}}\right)\frac{1}{\sqrt{\left(1+\frac{\tau}{\omega^2\tau_{Da}}\right)}} + \left(\frac{1-\mathrm{pa}}{1+\frac{\tau}{\tau_{Db}}}\right)\frac{1}{\sqrt{\left(1+\frac{\tau}{\omega^2\tau_{Db}}\right)}}\right] \tag{2}$$

For a consequent evaluation, we therefore have the following set of parameters, which need to be estimated for the two-component case: N, number of molecules in the excitation volume element; pa, percentage of species 1 in the confocal volume element; τ_{Da}, diffusion time of faster diffusing species in microseconds; τ_{Db}, diffusion time of slower diffusing species in microseconds; ω, structure parameter for the three-dimensional (3-D) Gaussian volume element which is given by the experimental setup and is generally fixed; p, fraction of molecules in the triplet states; τ_t, triplet correlation time in microseconds.

Here, we assume that the fraction of molecules in the triplet state, p and the triplet correlation time, τ_t are the same for both species as there would be no additional information in terms of the photophysics while fitting by having additional parameters for multiple species. Also, in this study, we set the quantum yield to one. This expression assumes a 3-D Gaussian spatial distribution of the probe volume. N is the average number of molecules present in the detection volume element $V = \pi^{3/2}\omega_{xy}{}^2\omega_z$, where ω_{xy} is the transversal extent and ω_z is axial extent at which the laser intensity has dropped by $1/e^2$. ω is consequently defined as $\omega = \omega_z/\omega_{xy}$, while $\tau_D = \omega_{xy}{}^2/4D$ denotes the diffusion time across the sampling region, where D is the diffusion coefficient. Thus, the average concentration of the molecules in the volume element is $C = N/V$.

iii. Description of Tests. A Pentium IV 2.4 GHz machine was used for all tests. The programs were written in C and

TABLE 1: Large Bound and Small Bounds Results for Various NFC Parameters in PGSL

		NSDC = 40			NSDC = 40	
original values	[large bounds]	NFC = 20	NFC = 40	[small bounds]	NFC = 20	NFC = 40
$N = 4.5$	[0.01−100]	4.508	4.503	[0.1−50]	4.50	4.49
	$((\Delta N)/(N)$ %)	(0.2%)	(0.08%)	$((\Delta N)/(N)$ %)	(0.1%)	(0.06%)
pa =0.35	[0.1−1]	0.364	0.357	[0.1−1]	0.363	0.344
	((Δpa/pa) %)	(4.3%)	(2.1%)	((Δpa/pa) %)	(3.8%)	(1.6%)
$\tau_{Da} = 60 \times 10^{-6}$	$[1 \times 10^{-8}$ to $1 \times 10^{-4}]$	64.13×10^{-6}	62.06×10^{-6}	$[1 \times 10^{-7}$ to $1 \times 10^{-4}]$	63.87×10^{-6}	58.49×10^{-6}
	$((\Delta\tau_{Da}/\tau_{Da})$ %)	(6.8%)	(3.4%)	$((\Delta\tau_{Da}/\tau_{Da})$ %)	(6.4%)	(2.4%)
$\tau_{Db} = 5 \times 10^{-4}$	$[1 \times 10^{-7}$ to $1 \times 10^{-3}]$	5.13×10^{-4}	5.05×10^{-4}	$[1 \times 10^{-5}$ to $1 \times 10^{-3}]$	5.11×10^{-4}	4.95×10^{-4}
	$((\Delta\tau_{Db}/\tau_{Db})$ %)	(2.6%)	(1.2%)	$((\Delta\tau_{Db}/\tau_{Db})$ %)	(2.2%)	(0.9%)
$p = 0.15$	[0.01−1]	0.1513	0.1513	[0.1−1]	0.1511	0.149
	$((\Delta p/p)$ %)	(0.9%)	(0.4%)	$((\Delta p/p)$ %)	(0.7%)	(0.3%)
$\tau_t = 1.2 \times 10^{-6}$	$[1 \times 10^{-9}$ to $1 \times 10^{-5}]$	1.22×10^{-6}	1.21×10^{-6}	$[1 \times 10^{-8}$ to $1 \times 10^{-5}]$	1.22×10^{-6}	1.19×10^{-6}
	$((\Delta\tau_t/\tau_t)$ %)	(2.0%)	(0.9%)	$((\Delta\tau_t/\tau_t)$ %)	(2.1%)	(0.5%)
	MSE →	1.26×10^{-6}	2.87×10^{-7}		1.06×10^{-6}	1.65×10^{-7}

interfaced with MATLAB (The Math Works, Inc.). We choose to use a simulated data set for the sake of effective comparison between the two algorithms. The values for the parameters described as the "original values" in Table 1 are $N = 4.5$, $pa = 0.35$, $\tau_{Da} = 60 \times 10^{-6}$ s, $\tau_{Db} = 5 \times 10^{-4}$ s, $\omega = 5$, $p = 0.15$, $\tau_T = 1.2 \times 10^{-6}$ s. Using eq 2, we generate a set of 288 points logarithmically spaced in the decades of time. For a data set of these 288 points as in Case Studies I and II, a typical fitting run with an NSDC of 40 and NFC of 40 took less that 3 s for output, which demonstrates the flexibility as well as the lesser computational cost as well. The number of iterations in PGSL for each of the evaluations is computed as NS (2) × NPUC (1) × NFC (40) × NSDC (40) × number of parameters (6) = 19200. Here, NS = 2 corresponds to an internal default value to the present version of the PGSL implementation used here. For a typical run of NFC = 20 and NSDC = 40, the number of iterations to reach convergence is around 9000 and for NFC = 40 and NSDC = 40 it goes up to 17 000. The only parameters to be determined for PGSL are the values of the Focusing cycles and Subdomain cycles. This fixes the number of iterations required and hence the computation time for a particular run. The sensitivity of the results obtained increases marginally as the number of iterations is increased. The table in the following subsection gives an overview of the quality of the fits obtained for a synthetic data set for the two-component case.

III. Algorithms

i. PGSL Algorithm. We describe the algorithms in terms of the parameters of the two-component case here, that is, for the accurate determination of N, pa, τ_{Da}, τ_{Db}, p, and τ_t. This is done by computing the global minimum of the least-squares error objective function, Π, defined by

$$\Pi = \sum_{i=1}^{K} [G_{fit}(\tau_i) - G_{data}(\tau_i)]^2 \qquad (3)$$

for K number of sample points and time interval given by τ.

We then utilize the PGSL algorithm, which is based on the direct global search technique.[19] This algorithm operates by organizing optimizations search through four nested cycles, namely, Sampling, Probability updating, Focusing, and Subdomain. Each cycle has a different role to perform while searching for the optimum solution. The user first defines the bounds for each variable that is used with the objective function Π. The method then searches for the optimum value of the objective function defined in Π, which is performed by matching the measured $G_{data}(\tau)$ with its predicted counterpart based on the estimated values of the variables N, pa, τ_{Da}, τ_{Db}, p, and τ_t. The algorithm initially generates random values for each variable in the Sampling cycle. Assuming equal probability of finding good solution in the entire search space, the residual error Π is evaluated by substituting all generated solutions in eq 3. This allows for selecting all points where the residual error is minimum. Probability-updating and Focusing cycles subsequently refine the search in the neighborhood of good solutions. Convergence to the optimum solution is achieved by means of the Subdomain cycle. The following are the main terms used for describing the PGSL algorithm.

Solution Point. A point consists of a value set for each of the variables N, pa, τ_{Da}, τ_{Db}, p, and τ_t.

Search Space. Search space is the set of all potential solution points. It is an M-dimensional space with an axis corresponding to each variable. M denotes the total number of variables. In the case presented here, $M = 6$. The user defines the minimum and maximum values, commonly known as bounds of variables along each axis. A subset of the search space is called a subdomain.

Probability Density Function, PDF. The PDF of a variable is defined in the form of a histogram. The axis represented by the variable is discretized into a fixed number of intervals. Uniform probability distribution is assumed within each interval. The PDF is used to search within a small neighborhood. Since PGSL works by global sampling, there is no point-to-point movement as compared with other random methods.

The function of each cycle is described below:

Sampling Cycle. In the sampling cycle, the number of samples evaluated in the sampling cycle (NS) are generated randomly by selecting a value for each variable according to its PDF. This sampling technique resembles the Monte Carlo technique. Each point is evaluated, and the point having the minimum cost, BS (Best Sample), is selected.

Probability-updating Cycle. The sampling cycle is repeated NPUC (number of iterations in the probability-updating cycles) times, and after each iteration, the PDF of each variable is modified using a probability-updating algorithm. This ensures that the sampling frequencies in regions containing good points are increased. In the probability-updating algorithm, the interval containing the value of the variable in BS is located. The evolution of the PDF for a variable after several sampling cycles is illustrated in Figure 3.

Focusing Cycle. The probability-updating cycle is repeated NFC (number of focusing cycles) times, and after each iteration, the current best point, CBEST, is selected. The PDF is updated by first locating the interval containing the value of each variable in CBEST. This probability is uniformly divided into its subintervals. The widths of these subintervals are calculated such that the PDF decays exponentially away from it. After subdivisions, intervals no longer have the same width and probabilities are heavily concentrated near the current best. The evolution

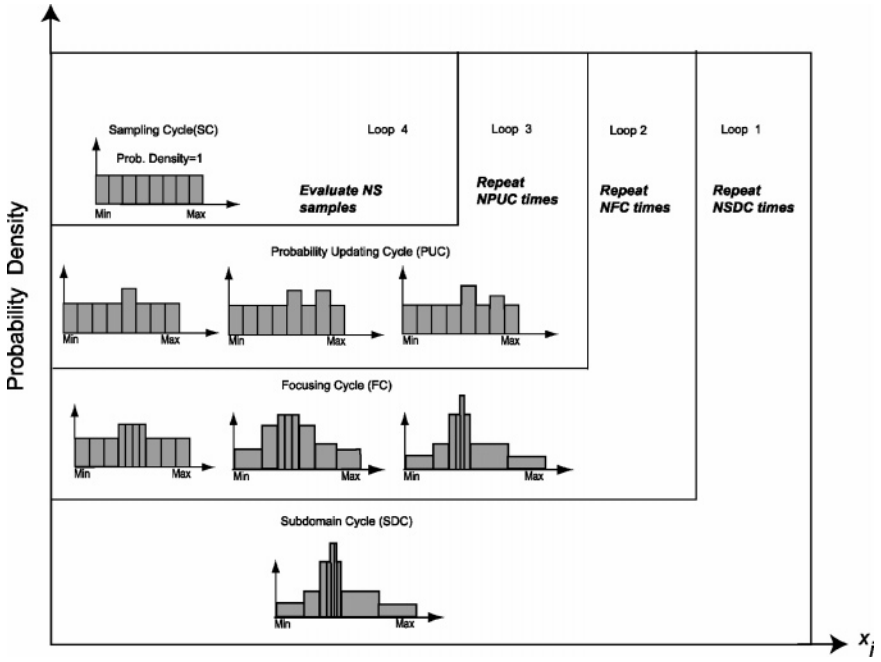

Figure 3. Illustration of the development of the probability density function of one optimization variable Xi during four nested loops of PGSL. This schematic summarizes the overall internal architecture of the PGSL.

of PDF after several probability-updating cycles is illustrated in Figure 3. Assume that the value of the variable in the best solution found in the first probability-updating cycle is Xb1. The interval containing this value is subdivided into four parts and is assigned 50% probability. The remaining probability is distributed to the other intervals according to an exponentially decaying function. Due to this probability distribution, 50% of variables in subsequent samples lie within their respective best intervals. This results in exploration of alternative values of some variables keeping the values of other variables in the best regions. Assume that the value of the variable in the best solution found in the second updating cycle is Xb2. The interval containing this value is further subdivided (for clarity, intervals are not shown to scale in the figure). Probability densities increase enormously due to fine division of intervals after many probability-updating cycles.

Subdomain Cycle. In the subdomain cycle, the focusing cycle is repeated NSDC (number of subdomain cycles) times, and at the end of each iteration, the current space search is modified. In the beginning, the entire space is searched, but in subsequent iterations, a subdomain of a smaller width is selected for search. The size of the subdomain decreases gradually, and the solution converges to a point. The scale factor is dynamically chosen such that there is no premature convergence. This is, however, not the case in ML (see section ii).

Each cycle therefore serves a different purpose in the search for a global optimum. The sampling cycle permits a more uniform and exhaustive search over the entire search space than the other cycles. The probability-updating and focusing cycles refine the search in the neighborhood of good solutions. Convergence is achieved by the subdomain cycle.

The parameter study revealed that only the values of the focusing cycles and subdomain cycles need to be adjusted to fix the total number of evaluations of the objective function in hand. This underlines the ease and simplicity of fixing PGSL parameters.

a. Approaches for Determining Global Minimum. The selection of an appropriate methodology is the key for successful data analysis. Before narrowing down to a particular method, it is imperative to study the topology of the parameter space for Π. Figure 4 shows a plot for Π in eq 3 from the experimental measure of Figure 2 obtained with an M13 labeled with RhG at 10 nM concentration on a cover glass. This plot is generated with two sensitive variables, namely, N and τ_{Da}, where the values of N are varied from 0 to 10 and τ_{Da} from 1×10^{-9} to 1×10^{3}. This log plot shows the presence of many local minimas and only one global minimum. There would be many minima for the entire multiparameter space of Π when one considers all the five variables simultaneously. The figure presented here considers only two of the sensitive variables for the sake of display. With traditional analysis, the FCS experimenter often encounters this situation while fitting experimental data when multiple solution sets are obtained for repetitive fitting on the same data set. The choice is then to obtain multiple data sets from many measurements and to do the cumulative analysis of the data therein or have multiple fitting sessions on the same data set with varying good initial guesses.

The proposed PGSL algorithm is ideal for the error function Π, since no initial guesses are required, and although the bounds need to be defined, the bounds do not require a difficult constraint selection.

For instance, for the variables in eq 3 is defined as follows

$$0 < N \leq 100,\ 0.1 \leq pa \leq 1,\ 1 \times 10^{-8} \leq \tau_{Da} \leq 1 \times 10^{-4},\ 1 \times 10^{-8} \leq \tau_{Db} \leq 1 \times 10^{-4},\ 0.01 \leq p \leq 1$$

and

$$1 \times 10^{-8} \leq \tau_{t} \leq 1 \times 10^{-5} \quad (4)$$

where the maximum and minimum values above represent the theoretical ranges of values possible for a particular dye molecule under consideration.

Boundary Sensitivity. Boundary sensitivity is the dependence of the parameter estimates for the range of values given to the PGSL algorithm. They are highly flexible and need to be modified appropriately with the system in hand. We can also set the lower bounds of pa and p to zero and get similar results for the two-component fit with the triplet model here. In case these parameters are not desired for evaluation, then one could

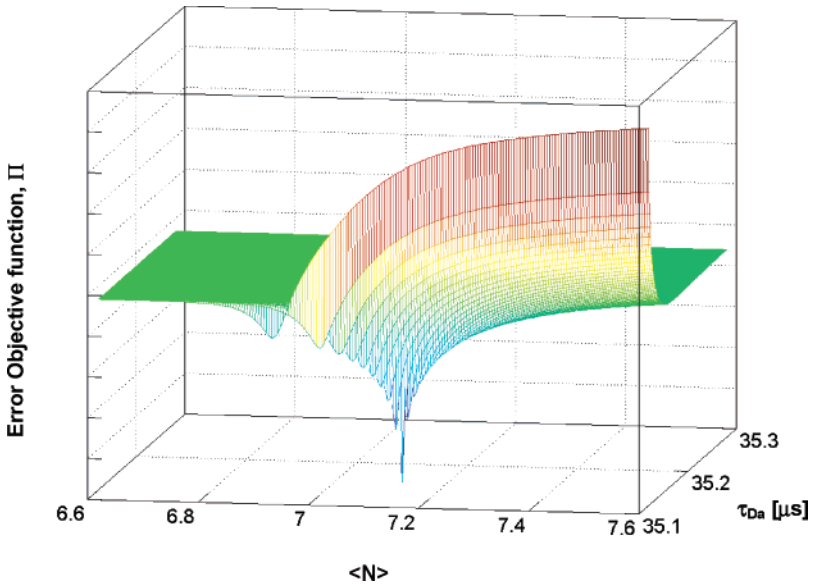

Figure 4. Magnitude of error for objective function Π defined in eq 3. The log plot shows the presence of several minima close to one global minimum for the choice of two parameters only for our two-component model.

choose the no triplet or the one-component model accordingly. The structure parameter ω is fixed in the analysis.

b. Mean Squared Error (MSE) of Fit in PGSL. It is desired for a fitting algorithm that it take into account the error of individual points.[20] We utilize the simple definition of MSE to evaluate the quality of fit in PGSL here.

$$\mathrm{MSE} = \frac{1}{K}\sum_{i=1}^{K}[G_{\mathrm{fit}}(\tau_i) - G_{\mathrm{data}}(\tau_i)]^2 \tag{5}$$

This value measures the difference between the fitted function $G_{\mathrm{fit}}(\tau)$ and the experimental data $G_{\mathrm{data}}(\tau)$ at every time interval τ, weighted by length of data points K. In Table 1, we see the performance of PGSL under various Focusing cycles (NFC) for the six parameters of the two-component case. The fitted values and also the relative percentage errors with respect to the initial original values are presented here. The values presented are a statistical value obtained after running the algorithm for 100 times. The choice of appropriate bounds also influences the MSE as seen in Table 1.

ii. Marquardt−Levenberg Algorithm. The ML algorithm[12,21] is briefly described in this section and is explained with regard to the two-component equation in eq 2 written in terms of the parameter **u**

$$G(\mathbf{u},\tau) = 1 + \frac{1}{u_1}\left(\frac{1+u_5}{1-u_5}\right)\exp\left(\frac{-\tau}{u_6}\right)\times \left[\left(\frac{u_2}{1+\frac{\tau}{u_3}}\right)\frac{1}{\sqrt{\left(1+\frac{\tau}{\omega^2 u_3}\right)}} + \left(\frac{1-u_2}{1+\frac{\tau}{u_4}}\right)\frac{1}{\sqrt{\left(1+\frac{\tau}{\omega^2 u_4}\right)}}\right] \tag{6}$$

where, u_1, u_2, u_3, u_4, u_5, and u_6 the elements of **u**, represent N, pa, τ_{Da}, τ_{Db}, p, and τ_{t}, respectively. To obtain any of the elements in **u**, we must calculate the residual error[21] $E(\mathbf{u})$

$$E(\mathbf{u}) = \sum_{i=1}^{K}(G(\mathbf{u},\tau_i) - d_i)^2 \tag{7}$$

for K number of sample points and the corresponding time interval given by τ_i and where d_i is the measured value at τ_i.

If $(\mathbf{u})^l$ is the initial guess for the parameter set **u**, the ML iteration step is given by

$$[\mathbf{J}((\mathbf{u})^l)^T\mathbf{J}((\mathbf{u})^l) + \lambda\mathbf{I}]((\mathbf{u})^{l+1} - (\mathbf{u})^l) = -\mathbf{J}((\mathbf{u})^l)^T\mathbf{E}((\mathbf{u})^l) \tag{8}$$

where $\mathbf{J}(\mathbf{u})$ is the Jacobian matrix, which is defined as

$$\mathbf{J}(\mathbf{u}) = \begin{bmatrix} \frac{\partial E_1(\mathbf{u})}{\partial N} & \frac{\partial E_1(\mathbf{u})}{\partial pa} & \frac{\partial E_1(\mathbf{u})}{\partial \tau_{\mathrm{Da}}} & \frac{\partial E_1(\mathbf{u})}{\partial \tau_{\mathrm{Db}}} & \frac{\partial E_1(\mathbf{u})}{\partial p} & \frac{\partial E_1(\mathbf{u})}{\partial \tau_t} \\ \frac{\partial E_2(\mathbf{u})}{\partial N} & \frac{\partial E_2(\mathbf{u})}{\partial pa} & \frac{\partial E_2(\mathbf{u})}{\partial \tau_{\mathrm{Da}}} & \frac{\partial E_2(\mathbf{u})}{\partial \tau_{\mathrm{Db}}} & \frac{\partial E_2(\mathbf{u})}{\partial p} & \frac{\partial E_2(\mathbf{u})}{\partial \tau_t} \\ \cdots & \cdots & \cdots & \cdots & \cdots & \cdots \\ \cdots & \cdots & \cdots & \cdots & \cdots & \cdots \\ \frac{\partial E_K(\mathbf{u})}{\partial N} & \frac{\partial E_K(\mathbf{u})}{\partial pa} & \frac{\partial E_K(\mathbf{u})}{\partial \tau_{\mathrm{Da}}} & \frac{\partial E_K(\mathbf{u})}{\partial \tau_{\mathrm{Db}}} & \frac{\partial E_K(\mathbf{u})}{\partial p} & \frac{\partial E_K(\mathbf{u})}{\partial \tau_t} \end{bmatrix} \tag{9}$$

The parameter λ is dynamically adjusted during the course of minimization where l is the current iteration and $l+1$ is the next iteration. T is the transpose operator and **I** is the identity matrix. The iteration process continues until some pre-specified termination criterion has been met, such as a given change in the value of the parameter **u** or a limit on the number of iterations.

Used in this way, the ML algorithm allows for computing of the optimal parameter **u**. We use the ML implementation available in the "Optimization Toolbox" in MATLAB with no changes in the default values for the various internal parameters described therein.

iii. Illustration of the Internal Architectures of PGSL and ML. PGSL has several interesting features not similar to other algorithms. First, it works by global sampling, thereby avoiding point-to-point improvement in a region around a current point. Second, it uses histograms for the PDF—a discontinuous function with multiple peaks. This allows fine control over probabilities in small regions by subdividing intervals. Third, the shape and form of the PDF can be changed by subdividing intervals as well as by directly increasing the probabilities of intervals. This is different from the normal practice of changing the standard deviation in other methods.

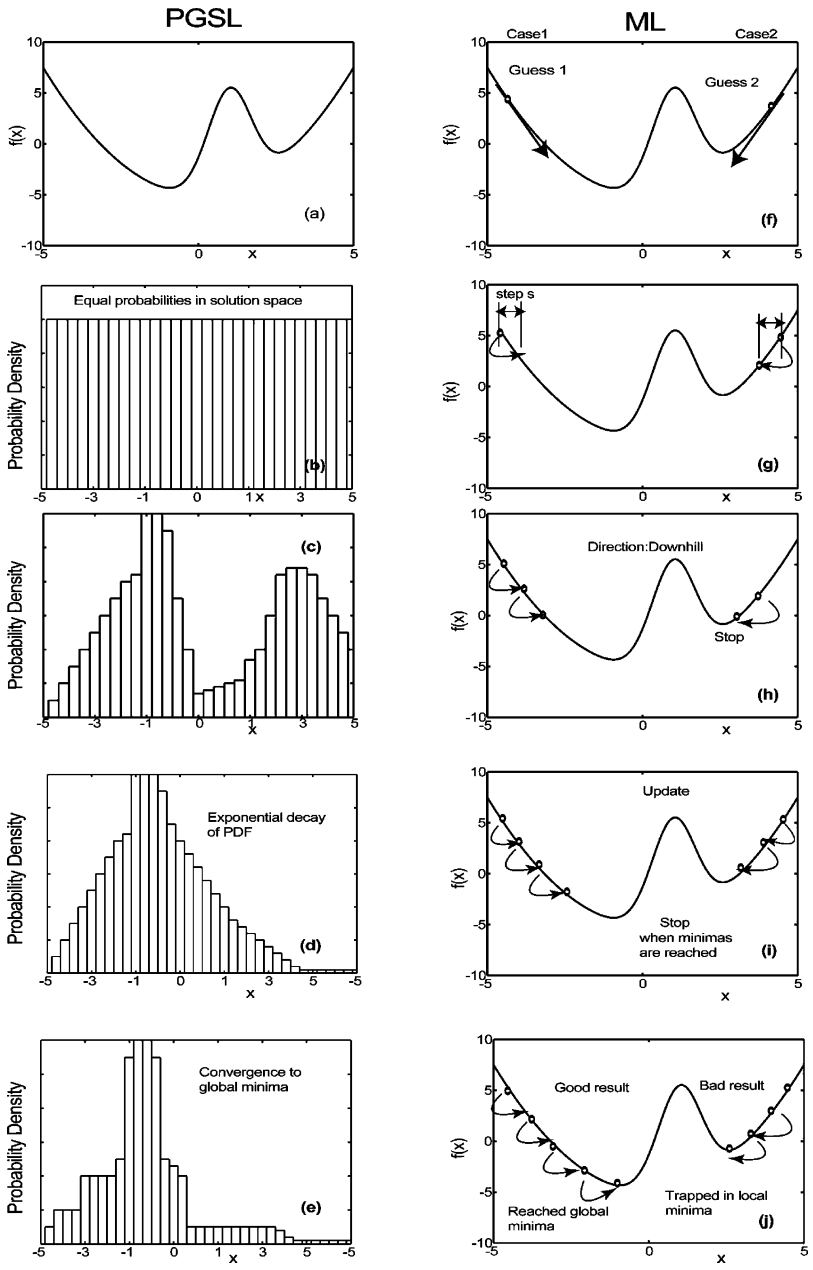

Figure 5. Illustration of basic differences between PGSL and ML. Points are randomly generated using a PDF in PGSL. Probabilities are increased in regions where good solutions are found: (a) a function $f(x)$ in a single variable, (b) a uniform PDF, (c) a PDF with higher probabilities in regions containing good solutions, (d) evolution of the PDF into regions with better solutions and the subsequent exponential decay of the PDF, and (e) search space progressively narrowed by converging to points in a subdomain of smaller size centered on the best point. The ML operates on the premise of intense searching in (f) initial guesses for two cases here considered by the seeking the minimum of the function, (g) the step size (s) is chosen in the direction of steepest descent, (h) chosen in the direction of steepest descent iteration continues towards the minimum, (i) point updated in the direction of the slope until minimum is reached, and (j) "stop" when the function hits the minimum value possible.

PGSL therefore works directly on the solution search space and does not seek any gradients for approaching the global minima. This key feature enables PGSL to generate an optimal solution set for any noise level by avoiding getting trapped into local minima irrespective of the complexity of the error objective function (see parts a−e of Figure 5).

Whereas a local search technique like the ML method finds good solutions using an exhaustive search over a constrained space provided, they are given good initial guesses. It is therefore a nontrivial task to compare two different categories of algorithms wherein their individual internal architectures differ as markedly as those seen here (see parts f−j of Figure 5).

IV. Case Studies

i. Case Study 1: PGSL Applied to a Two-Component System of Interacting Fluorophores. On the left-hand side of Table 1, the bounds are varied to the maximum extent as permissible by the parameters of interest for the case of large bounds. This clearly shows the strength of PGSL in generating acceptable solutions with no initial guesses for arbitrarily large bounds.

On the right-hand side of Table 1, we see the performance of PGSL under various focusing cycles (NFC) with small bounds as compared with the previous case. The differences are mainly for the bounds in the various diffusion times for the

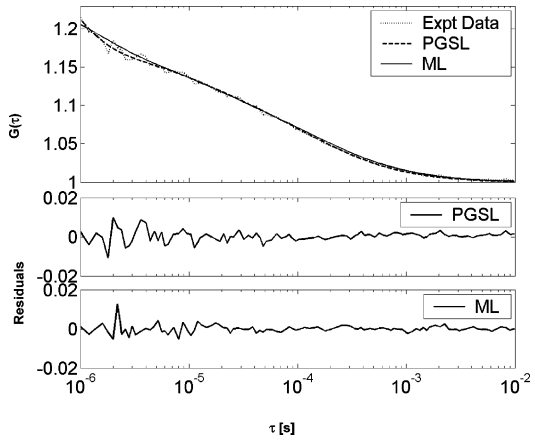

Figure 6. Fitting of experimental FCS data with PGSL and the Marquardt−Levenberg algorithm: (a) the experimental data with the fits in ML and PGSL with eq 2, (b) the residuals using PGSL, and (c) the residuals using the ML algorithm.

model under consideration here. We see an increase in the sensitivity of the obtained parameters.

The MSE is different for the various cases and gives the quality of fit for every particular choice of NFC and NSDC.

We have good solutions for both high and low required accuracies. The overall setting of the NSDC being 40 and an NFC of 20 or 40 provides optimal fits here. These results were also confirmed by testing them on several different models as well.

ii. Case Study 2: PGSL Applied to Parameter Estimation with Noisy Data. FCS is susceptible to various noise sources such as intrinsic photon shot noise dependent on the average count rate, excitation power instabilities, Raman scattering, and background fluorescence.[22−24] Also, depending on the type of individual setups or application (two-photon or intracellular systems) at hand, the contribution of various noise sources leading to improper fitting is another source of systematic error leading to erroneous interpretation of the obtained data.

In our context of addressing fitting artifacts especially in noisy data, we present the main influence of averaging noise here. The following measurement (Figure 6) was done on a 3 s measurement time interval on the M13−RhG sample as before at 10 nM concentration. The data mainly contains the overall effect of shot noise (governed by Poisson statistics) and averaging noise (for the long lag times during the finite measurement interval T).

TABLE 2: Comparison of PGSL and ML for a Noisy Experimental Data Set

		N	pa	τ_{Da} (μs)	τ_{Db} (μs)	p	τ_t (μs)	MSE
30 s (ref)	PGSL	7.2	0.34	35.20	201.4	0.31	2.02	4.32×10^{-6}
3 s	PGSL	5.56	0.40	20.6	151.9	0.5	1.6	7.5×10^{-4}
3 s	ML	5.52	0.54	192.3	11.2	0.28	1.33	4.4×10^{-4}

We clearly see in Table 2 that the values obtained for ML are not satisfactory for τ_{Da}, τ_{Db}, and τ_t for this particular fit here, although the residuals look satisfactory. It is evident that the ML has converged to a wrong minimum in the six-parameter space here. This is an illustration, where the experimenter has to refit the data with varying initial guesses and bounds until a good fit is obtained. For this simple case, it is possible to obtain better results for ML by fixing the faster diffusing parameter (τ_{Da}) for the standard dye label attached by undertaking calibration measurements on the setup used. Therefore, with good initial guesses and prior knowledge of system behavior, ML does perform very well. However, in cases for measurements in, for example, living cells where additional noise terms are also an issue to be considered,[25] the very choice and reliability of good initial guesses would be a nontrivial task.

V. Benchmark Tests between PGSL and ML

In this section, we benchmark and evaluate the performance of PGSL and ML for the objective function defined in eq 3. This is done by obtaining the best MSE for three different threshold values in both the situations.

i. Description of Tests and Results in PGSL vs ML. PGSL Algorithm. It is run for two different cases for large and small bounds (as in Table 1) for the given simulated data. The initial seed values for starting the solution search are randomly varied for each iteration for a fixed NSDC of 40 and an NFC of 40. This ensures that a new random number starts the global search process in the solution space for every iteration.

ML Algorithm. The initial guesses for the two sensitive parameters, N and τ_{Da}, are automatically generated by the correlogram itself. The initial guess for N follows from the simple relation $G(\tau \rightarrow 0) = 1/N$, while for τ_{Da} the time value corresponding to $G(\tau_{Da}) = {}^1/_2 G(0)$ is chosen. For 100 runs, the

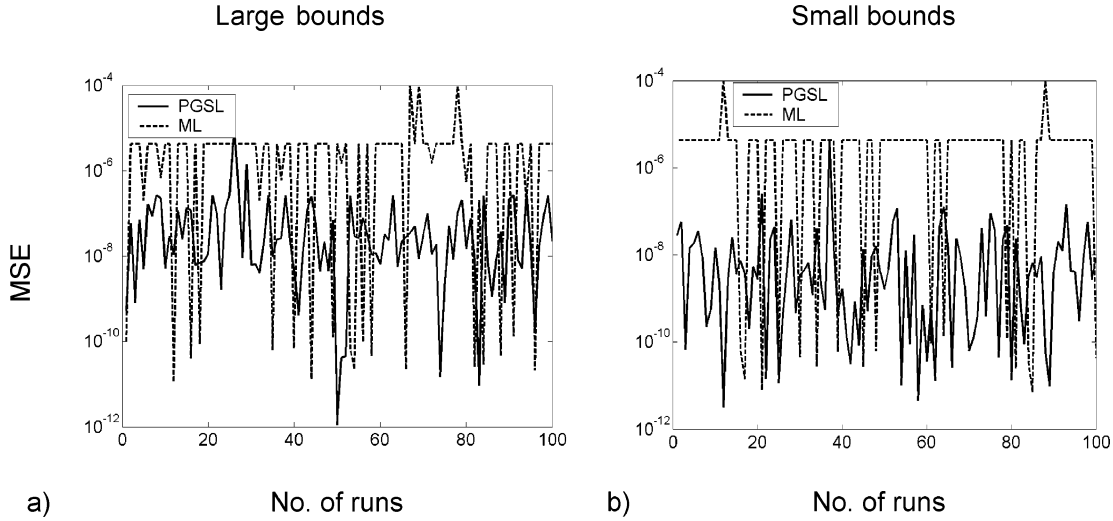

Figure 7. Mean-squared error plots for the data evaluated comparing the performances of PGSL (dark lines) and ML (dotted lines) for (a) large bounds and (b) small bounds.

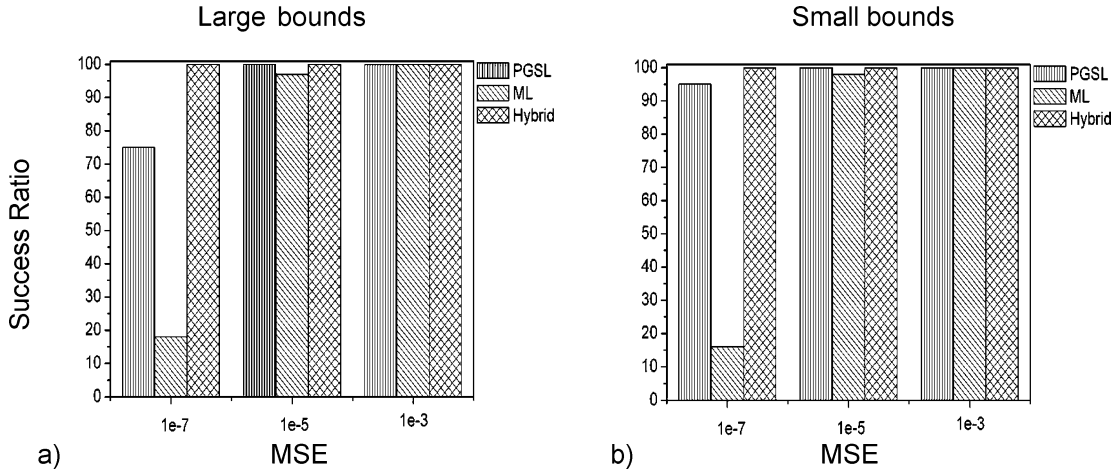

Figure 8. Reliability study of obtaining the best mean-squared error for the data is seen in the bar plots comparing the performances of PGSL, ML, and their hybrid: (a) large bounds and (b) small bounds. PGSL outperforms ML and results in a better MSE value, indicating better fit quality.

initial values are randomly varied around the above chosen mean value so that we have a different start value at each iteration for τ_{Da}. For τ_{Db}, the value chosen is twice that of the τ_{Da}. The triplet fraction p is chosen at 10% while for τ_t a typical value of 1 μs is given as the initial guess value.

Hybrid Algorithm. We further explore the possibility of combining the mutual abilities of PGSL and ML and call it a hybrid. Here, the output of PGSL is fed as an initial guess to ML, and the resultant hybrid performance is evaluated here as well.

After performing 100 runs for varying guesses for ML and by varying the initial random value for PGSL, we obtain the varying MSE for large and small bounds can be seen again in Figure 7.

We see that PGSL outperforms ML consistently in terms of the MSE throughout. This is further summarized in terms of the success ratio in Figure 8.

The success ratio is defined as the percentage of iteration steps which gives the MSE below the predefined threshold.

In the bar graphs, we have fixed three threshold values for the MSE. For each iteration, in all the three cases, the fit generates a particular value of the MSE. The sensitivity of our iterations was evaluated by checking on the various MSE thresholds. For a MSE threshold value such as 1×10^{-7}, which corresponds to a better quality of the fit obtained, we see that the success ratio is lower as compared with the other two cases. Correspondingly, we obtain a higher success ratio when we choose to lower our fit quality (as for an MSE threshold of 1×10^{-3}).

For both large and small bounds, we see that PGSL outperforms ML throughout and their corresponding hybrid approach moves toward the limit of performance as that of PGSL. These tests conclusively prove that PGSL is a robust search technique that performs well in spaces with multiple local minima.

Because of the generality of the procedures discussed here, we believe that PGSL is useful for various FCS fitting models. Simple guidelines leading to parameter adaptation as seen above depending on the models and also on the physical systems under study would lead to even better convergence in PGSL. This would then result in faster parameter retrieval for large data sets as in assays.[26] Also, for highly heterogeneous systems with multiple diffusing species, PGSL would provide a bias-free fitting of the data for the model chosen on hand since it would always generate acceptable solutions for the chosen model without the need for a priori user knowledge of the physical system.

VI. Conclusions

To conclude, we have described a novel stochastic data analysis concept applicable to the determination of fitting parameters in FCS experiments. For the two-component case, the FCS parameters are determined with high precision by the application of this algorithm. The fitting values are given the lower and upper bounds with no initial guesses thereby giving the experimentalist the confidence in data validation when experiments are to be planned requiring the application of various models. It is therefore useful in experimental situations wherein accurate determination of parameters with no fitting artifacts from various physical models is also a prime criterion. We also determine the quality of the fit from the MSE analysis. Statistical studies further demonstrate the capability of the method to estimate the fit parameters with greater confidence along with existing standard gradient-based methods. The robustness of PGSL on noisy experimental data for parameter estimation is also shown. Therefore, PGSL appears to be a viable tool for unbiased parameter retrieval of FCS data.

Acknowledgment. We would like to thank Benny Raphael and Per Thyberg for valuable discussions and suggestions. We also acknowledge the positive feedback of one of the reviewers toward the effective presentation of this research. This research is partly funded by the Swiss National Science Foundation. Program Availability: The PGSL programs are available free of charge either directly from the authors (e-mail or conventional mail) or can be downloaded from the laboratory website: http://lob.epfl.ch/page58512.html.

References and Notes

(1) Magde, D.; Webb, W. W.; Elson, E. *Phys. Rev. Lett.* **1972**, *29*, 705.
(2) Magde, D.; Elson, E. L.; Webb, W. W. *Biopolymers* **1974**, *13*, 29.
(3) Magde, D. *Q. Rev. Biophys.* **1976**, *9*, 35.
(4) Aragon, S. R.; Pecora, R. *Biopolymers* **1975**, *14*, 119.
(5) Ehrenberg, M.; Rigler, R. *Q. Rev. Biophys.* **1976**, *9*, 69.
(6) Ehrenberg, M.; Rigler, R. *Chem. Phys.* **1974**, *4*, 390.
(7) Magde, D.; Elson, E. L. *Biopolymers* **1978**, *17*, 361.
(8) Pick, H.; Preuss, A. K.; Mayer, M.; Wohland, T.; Hovius, R.; Vogel, H. *Biochemistry* **2003**, *42*, 877.
(9) Ehrenberg, M.; Rigler, R. *Chem. Phys.* **1974**, *4*, 390.

(10) Widengren, J.; Mets, U.; Rigler, R. *J. Phys. Chem.* **1995**, *99*, 13368.
(11) Cluzel, P.; Surette, M.; Leibler, S. *Science* **2000**, *287*, 1652.
(12) Marquardt, D. W. *J. Soc. Ind. Appl. Math.* **1963**, *11*, 431.
(13) Enderlein, J.; Gregor, I.; Patra, D.; Fitter, J. *Curr. Pharm. Biotechnol.* **2004**, *5*, 155.
(14) Hess, S. T.; Webb, W. W. *Biophys. J.* **2002**, *83*, 2300.
(15) Raphael, B.; Smith, I. F. C. *Appl. Math. Comput.* **2003**, *146*, 729.
(16) Robert-Nicoud, Y. R. I.; Raphael, B.; Smith, I. F. C. *J. Comput. Civ. Eng.* **2005**, *19*, 239.
(17) Patil, A.; Raphael, B.; Rastogi, P. *Opt. Lett.* **2004**, *29*, 1381.
(18) Krichevsky, O.; Bonnet, G. *Rep. Prog. Phys.* **2002**, *65*, 251.
(19) Masri, S. F.; Bekey, G. A.; Safford, F. B. *Appl. Math. Comput.* **1980**, *7*, 353.
(20) Wohland, T.; Rigler, R.; Vogel, H. *Biophys. J.* **2001**, *80*, 2987.
(21) Aster, R.; Borchers, B.; Thurber, C. *Parameter Estimation and Inverse Problems*; Academic Press: Amsterdam, The Netherlands, 2004; p 184.
(22) Koppel, D. E. *Phys. Rev. A* **1974**, *10*, 1938.
(23) Qian, H. *Biophys. Chem.* **1990**, *38*, 49.
(24) Kask, P.; Gunther, R.; Axhausen, P. *Eur. Biophys. J. Biophys. Lett.* **1997**, *25*, 163.
(25) Schwille, P.; Haupts, U.; Maiti, S.; Webb, W. W. *Biophys. J.* **1999**, *77*, 2251.
(26) Eggeling, C.; Berger, S.; Brand, L.; Fries, J. R.; Schaffer, J.; Volkmer, A.; Seidel, C. A. M. *J. Biotechnol.* **2001**, *86*, 163.

Curriculum Vitæ

G. RAMACHANDRA RAO

Born on July 13, 1978 in Chennai, India; Indian nationality; single.

EDUCATION AND PROFESSIONAL EXPERIENCE

- Research Assistant and Graduate Student [6.2002– 12.2006]: Laboratoire d'Optique Biomedicalé, Ecole Polytechnique Fédérale de Lausanne,(EPFL), Lausanne, Switzerland
  Doctoral Thesis: Fluorescence Correlation Spectroscopy - Simulations and Biochemical Applications based on Solid Immersion Lens concepts.

- Project Associate [1.2002 – 6.2002]: Applied Photonics Laboratory, Electrical Communication Engineering Dept,
  Indian Institute of Science (IISc), Bangalore, India.

- Master of Technology in Applied Optics [2002]: Dept. of Physics, Indian Institute of Technology, Delhi (IITD), India.

- Master of Physics [2000]: Dept. of Physics, Sri Sathya Sai Institute of Higher Learning (SSSIHL), India.

- Bachelor of Physics (Honours) [1995]: Dept. of Physics, Sri Sathya Sai Institute of Higher Learning (SSSIHL), India.

- Class XII [1995]: All India Senior School Certificate Examination, Central Board for Secondary Education (CBSE), New Delhi.

- Class X [1993]: All India Secondary School Certificate Examination, Central Board for Secondary Education (CBSE), New Delhi.

TEACHING EXPERIENCE

1. Research assistant [2002-2005]: Laboratoire d'Optique Biomedicalé, EPFL
   Teaching assistant to courses offered at the Masters level *viz*, Microscopie et Métrologie Optiqué, Optical Design and Applied Optics.

2. Student-Assistant [2000-2001]: IIT-Delhi, Assistant in the Physics Department.

LANGUAGE SKILLS

- English - Fluent
- French - Basic
- Kannada - Mother Tongue
- Hindi - Fluent
- Telugu - Good

COMPUTER SKILLS

PROGRAMMING

MatLab, Mathematica, C, C++, LaTeX

ENGINEERING PACKAGES

Zemax, Opti-BPM, Opti-Fiber and TracePro.

AWARDS

Received Ministry of Human Resources Development scholarship, Govt of India.

PUBLICATIONS

Journals

1. **Rao, R**., Langoju, R., Gösch, M., Serov, A. and Lasser, T., Stochastic approach to Data Analysis in Fluorescence Correlation Spectroscopy, *Journal of Physical Chemistry A, 110(37) pp 10674 - 10682 ,2006.*
2. **Rao, R**., Mitic, J., Serov, A. and Lasser, T., Field confinement with aberration correction in a Solid Immersion Lens based Fluorescence Correlation Spectroscopy set-up, to be published in *Optics Communications*.
3. **Rao, R**., Bolinger, P.Y., Lopez, A., Rigler, P., Vogel, H. and Lasser, T., Temperature controlled *in situ* Fluorescent Correlation Spectroscopy investigation on vesicles with a thermally decoupled sample holder using a Solid Immersion Lens, manuscript to be submitted to *Journal of Biomedical Optics*.
4. Leutenegger, M., **Rao, R**., Leitgeb, R and Lasser, T., Fast focal field calculations., *Optics Express.*14, 11277-11291 (2006).
5. Hassler, K., Leutenegger, M.,Rigler. P., **Rao, R**., Rigler, R.,Gösch, M., and Lasser, T., "Total internal reflection fluorescence correlation spectroscopy (TIR-FCS) with low background and high count-rate per molecule,"*Optics Express.* Volume 13, 7415-7423, 2005.
6. Serov, A.,**Rao, R**. ,Gösch, M. ,Anhut, T. ,Martin, D. ,Brunner, R. ,Rigler, R. and Lasser, T., High light field confinement for fluorescent correlation spectroscopy using a solid immersion lens, *Biosensors and Bioelectronics.*, Volume 20, Issue 3, 431-435, 2004.

Conference Proceedings and Patents

1. Patent : Solid Immersion Lens Spectroscopy and Microscope.

2. Serov, A., **Rao, R**. , Gösch, M. , Anhut, T. , Martin, D. , Brunner, R. , Rigler, R. and Lasser, T., Sub-wavelength resolution fluorescent correlation spectroscopy using a solid immersion lens, SPIE Vol. 5486, 307-314, (2004).

Others

1. M. Tech Thesis, Submitted at Dept of Physics, IIT, Delhi on December 2001.

2. IISc Project Report, Development of project proposal in the area of "Fiber Lasers" for a research grant from the funding agencies. Submitted on June 2002.